DISTRIBUTED TRANSDUCER DESIGN FOR THE ACTIVE CONTROL OF MULTIDIMENSIONAL ELASTIC STRUCTURES

by

JEANNE MARIE SULLIVAN

B.S. Physics, Carnegie Mellon University
(1988)

S.M. Mech. Eng., Massachusetts Institute of Technology
(1990)

SUBMITTED TO THE DEPARTMENT OF MECHANICAL ENGINEERING
IN PARTIAL FULFILLMENT OF THE REQUIREMENTS
FOR THE DEGREE OF

DOCTOR OF PHILOSOPHY

at the

MASSACHUSETTS INSTITUTE OF TECHNOLOGY
May 9, 1994

Signature of Author.....
Department of Mechanical Engineering, May 9, 1994

Certified by.....
Dr. James E. Hubbard, Jr., Thesis Committee Chairman
Lecturer, Department of Mechanical Engineering
Vice President, Optron Systems, Inc.

Approved by.....
Dr. Shawn E. Burke, Technical Supervisor
C.S. Draper Laboratory, Inc.

Accepted by.....
Professor Ain A. Sonin
Chairman, Department Graduate Committee

DISTRIBUTED TRANSDUCER DESIGN FOR THE ACTIVE CONTROL OF MULTIDIMENSIONAL ELASTIC STRUCTURES

by

Jeanne Marie Sullivan

submitted to the Department of Mechanical Engineering
on May 9, 1994 in partial fulfillment of the requirements
for the Degree of
Doctor of Philosophy

ABSTRACT

A new modeling method for two-dimensional distributed transducers with arbitrary spatial distribution is presented. The spatial weighting of a two-dimensional distributed transducer is defined using multidimensional distributions with composite functions as arguments. A distributional calculus is developed to determine the spatial differential operator describing the spatial dynamics of induced-strain transducers. The methodology, valid for both uniaxial and biaxial transducers, is applied to several model problems and the results are compared with previous research and limiting cases.

Two-dimensional transducer shading and its implications for the active control of thin plates are then discussed. Two-dimensional transducer shaping is presented as a design tool for the control problem. A method is described for approximating continuously shaded transducer distributions with a combination of transducer shaping and gain-weighting. A least-squares optimization method is used to fit the approximation to a continuous transducer distribution over a specified number of modal coefficients. The analysis is applied to two examples. The first utilizes two-dimensional transducer shaping alone to establish controllability and observability over the acoustically significant modes in a simply-supported plate. Even-even modes, which would not couple into the acoustic radiation field, are filtered out by this distribution. The second distribution is a superposition of gain-weighted, shaped transducer sections, which provides a close approximation to a continuous two-dimensional shaded transducer distribution. This distribution provides "all-mode" controllability and observability over a large bandwidth and is therefore useful for global vibration suppression.

A closed-loop vibration control experiment is described in which the "all-mode" transducer distribution is used to actively damp vibrations in an aluminum plate. The boundary conditions of the plate are approximately simply-supported with a rotational edge constraint. The transducers are

constructed from distributed piezopolymer film. Velocity feedback of the colocated actuator/sensor transducer distributions yields a reduction in settling time of more than fifty percent compared to the open-loop system when subjected to an wide-band transient input disturbance.

Thesis Committee:

Dr. James Hubbard, Jr., Chairman
Prof. Jean-Jacques Slotine
Prof. Wallace Vander Velde
Dr. Shawn Burke (Draper)

Acknowledgements

I would like to thank all of the members of my thesis committee for their advice, encouragement and support. Jymn Hubbard, as the head of my committee, provided valuable experience in the field and was a very enthusiastic supporter of the work. I am also grateful for the confidence he showed in me when he hired me on as a graduate student. Shawn Burke was my supervisor at Draper and was always "on call" when I needed any kind of assistance. I appreciate all of the time he spent with me working on my experiment in the laboratory. He taught me a great deal about how to hunt down and understand the bugs (25.31 Hz) in a controls experiment. Professors Jean-Jacques Slotine and Wallace Vander Velde gave helpful critiques of the work and many useful suggestions for improving the theoretical foundation. Professor Vander Velde's detailed attention to my writing really improved the final product.

I owe a huge thank you to my friend and fellow lab partner, John Meyer. He was always there to brainstorm, help me build things, debug computer programs, answer my questions, and take frequent junk food breaks. He made the years working on this thesis infinitely better than they would have been without him. I was very lucky to have had the opportunity to work with him.

Joe Paradiso helped with the electronics for my experiment and was a lot of fun to work with. Dan Hegg helped me to understand distribution theory and how to develop a good proof. I also enjoyed working with and learning from Tom Bailey.

There are a number of people at M.I.T. that I would like to thank as well. Leslie Regan deserves many thanks for helping to get me through M.I.T. She is a great morale booster and the department is lucky to have her as the graduate administrator. Prof. Gilbert Strang gave advice on using two-dimensional distributions. Prof. Kamal Youcef-Toumi helped to prepare me for the qualifying examinations. Professors Mary Boyce, William Durfee, and Ain Sonin always had an open-door policy and gave great advice.

There are several people from the Structures and Controls Division at the Air Force Phillips Laboratory who helped me to get a long educational delay

before active duty. They include Kevin Slimak, Alok Das, and Major Maurice Martin. Major Martin was especially helpful in dealing with the Air Force bureacracy and providing much encouragement in the final months. Also, I would like to thank Bill Hallauer for his help with the stability analysis work in this thesis.

I was very fortunate to have a bunch of friends who helped get me through the ups and downs of the last few years. I would first like to thank my best friend Mike Hughes for all of his support and great sense of humor. I have known him since elementary school and it was an amazing stroke of luck for both of us to end up in the M.I.T. PhD program together. I would like to thank Monique Gaffney, Dana Hartley, Chris Lu, Melody Meyer, Li Shu, Akhil Madhani, Jen Wu, Cathy Lin, Cathy Chen, Anna and Sam Druker, Lisa Mitchell, Shari Kinzinger, Bilal Mughal, Bob Regan, Dino DeAngelis, Walter Baker, and Pete Millington for being great buddies. Also, I would like to thank the steadfast members of MEGAwomen for their friendship and camaraderie including Karon MacLean, Ellen Arruda (now a professor), Heather Beck, Naomi Chesler, Lou Jarendra, and Catherine Ford.

Finally, I would not have made it to this point without the love of my family. My brother, John, and future sister-in-law, Jessy, have been incredibly supportive and lots of fun to hang out with. My parents, Ken and Terry, have always had faith in me and really let me know it! The whole experience showed me how lucky I was to have such a great family. Thanks!

This thesis was prepared at The Charles Stark Draper Laboratory, Inc. under Internal Research and Development Projects 352 and 466. Publication of this thesis does not constitute approval by the Draper Laboratory of the findings or conclusions contained herein. It is published for the exchange and stimulation of ideas. I hereby assign my copyright of this thesis to The Charles Stark Draper Laboratory, Inc., Cambridge, Massachusetts.

Jeanne Sullivan

Permission is hereby granted by The Charles Stark Draper Laboratory, Inc., to the Massachusetts Institute of Technology to reproduce any or all of this thesis.

List of Figures

List of Tables

Chapter 1:

Introduction

1.1 Historical Background

The need for active structural control arises in many applications. Recent research has examined its utility for sound transmission/radiation suppression.[1,2] Structures can transmit sound or they can radiate sound when excited by a mechanical or acoustic disturbance. The resulting sound field is undesirable in many applications, including duct noise, aircraft cabin noise, industrial machinery noise, car interior noise, and marine hull noise.[3] Previous research has studied the use of multiple sound sources for noise cancellation in the far-field, but direct vibration inputs to plates and shells have been shown to be more effective and practical.[4] Microphones placed in the far-field have been used for sensor input, but distributed sensors applied directly to the structure have also been shown to be more feasible.[2]

One of the more challenging classes of structural control problems can occur with precision space structures. Many space structures have stringent performance requirements for shape control and vibration suppression. These structures have a large number of lightly-damped vibrational modes within their performance bandwidth.[5] This means that a commanded maneuver, such as a slew, could excite vibrational modes with long decay times, degrading performance and possibly destabilizing the system. Space structures are also subjected to mechanical and environmental disturbances from thermal gradients, thrusters, momentum wheels, and machinery vibration. Active structural control, in the form of global vibration suppression, may be required to maintain a specific shape and to damp vibrations in the presence of both deterministic and stochastic disturbances.

Another application which may require global vibration suppression involves panel flutter for supersonic vehicles, including airplanes and launch vehicles. Bisplinghoff and Ashley[6] discussed the problem of fatigue as

the principal mode of structural failure in panel flutter problems. Both flat panels and buckled or slightly curved panels have been studied in this area.[6]

Generally, active structural control techniques seek to cancel known plant dynamics and replace them with a set of desired dynamics. Unfortunately, a large amount of model uncertainty is present in structural systems.[7,8,5] There may be parametric uncertainty in the mass and stiffness properties of the structure, and this will manifest itself as uncertainty in the natural frequencies of the structure.[7,8] In addition, structures theoretically have an infinite number of modes and in practice have large number of modes present within their performance bandwidth. This can lead to non-parametric uncertainty in the model order if a controller requires truncation of modes.[5] The disturbance environment is also often poorly known. The disturbances may be transient or continuous, either stochastic or deterministic.

A structural component common in all of these applications is the panel. In this thesis, flat panels in the form of thin plates will be considered. However, in the future, the work can be expanded to curved panels and shells. Much of the previous research in structural control has focused on beams,[9-15] but plates are more complex and therefore have not received as much attention in the literature.

1.2 Previous Research

Much of the original research in the active control of plates made use of discrete sensors and actuators.[1,16] The distribution of these transducers across the surface of the plate was determined in an ad hoc manner. Centralized, multivariable control techniques were used for closed-loop control.

Meirovitch and Thangjitham,[1] in a theoretical study, considered the use of discrete sensors and actuators collocated on opposite sides of a simply-supported plate to provide open-loop and closed-loop control for minimization of the radiated sound field. Because they used LQR (Linear Quadratic Regulator) for the closed-loop control and full-state feedback of the modal states, one sensor-actuator pair was needed for each mode of the plate

to be controlled. This made it quite difficult to implement closed-loop control for a large number of modes. In addition, because the LQR controller was based upon perfect knowledge of the modal states, the closed-loop compensator was very sensitive to model uncertainty. Figure 1.1 shows the actuator distribution that was considered, with an identical sensor distribution located on the opposite side of the plate. There are 13 discrete actuators, with the locations chosen such that they are spaced evenly across the plate. Controllability and observability for a given mode will be lost, however, when nodal lines run through the transducers.

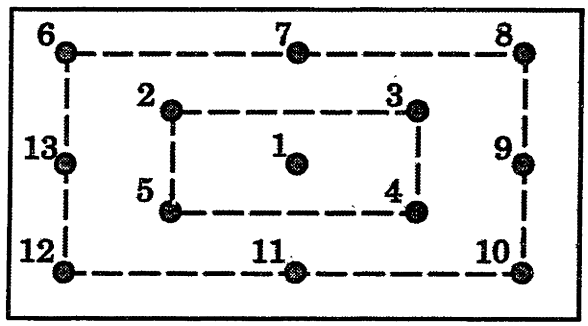

Fig. 1.1 Actuator/sensor locations for LQR/modal feedback of simply-supported plate (after Meirovitch and Thangjitham[1]).

Greeley *et al.*[16] described a plate control experiment using a limited number of discrete sensors and actuators. Using the Maximum Entropy/Optimal Projection control method, they designed a reduced-order compensator which required fewer sensors and actuators than the number of modes to be controlled. Fig. 1.2 shows the sensor and actuator distribution for this experiment. Note that some sensors were not collocated with actuators. They were able to suppress vibrations in a vertically suspended square plate with a disturbance bandwidth which included one hundred modes. Slots were cut in the corners of the plate to increase the modal density. Their compensator, however, was dependent upon a detailed modal identification test and therefore was sensitive to both parametric and non-parametric uncertainties.

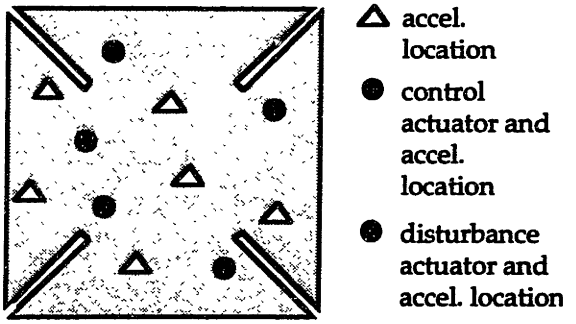

Fig. 1.2 Actuator/sensor locations for ME/OP control of a vertically suspended square plate (after Greeley *et al.*[16]).

Several researchers have considered using distributed transducers for the active control of plates.[17-21] Lee and Moon[17] studied the use of piezoelectric transducers for plate sensing and control. As shown in Fig. 1.3, they varied the skew angle of the material axes of piezopolymer film (PVDF) with respect to the geometrical axes of the plate laminate, a layered composite, and showed how this affected the loading/sensing parameters of the film. The boundary of the transducer, however, was assumed to be rectangular with axes coincident with those of the plate.

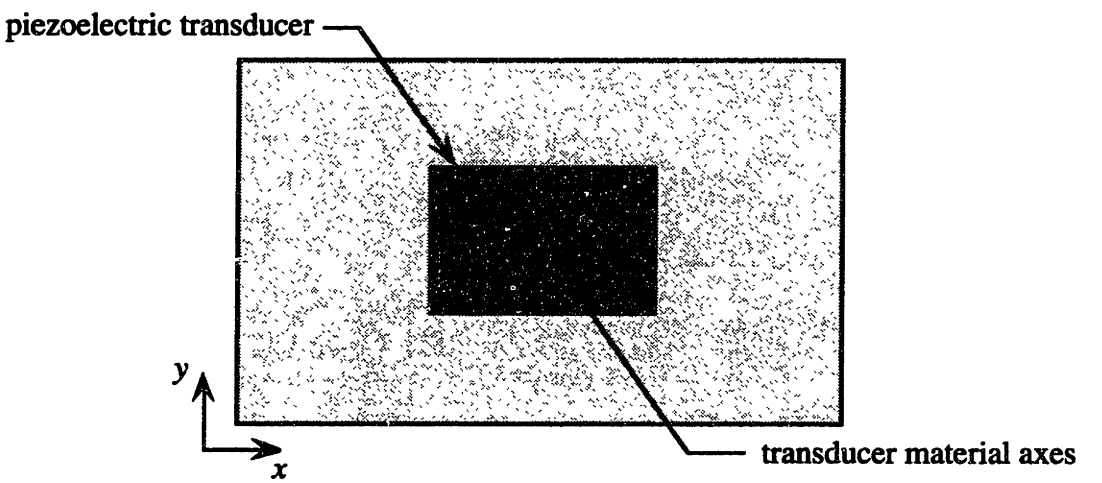

Fig. 1.3 Piezoelectric transducer distribution with finite skew angle between material axes and boundary/plate axes.

Clark and Fuller,[2,18] Clark *et al.*[19] and Clark and Burke[20] investigated one-dimensionally shaped PVDF sensors for sensing acoustically significant

modes in plates. Although these shaped transducers were applied to plates, their width is small in comparison to the smallest transverse wavelength present in the plate's dynamic response. However, errors in the placement of these sensors can lead to coupling with undesired modes in experimental implementations.[20]

These sensors were combined with rectangular piezoceramic patches in the closed-loop control experiment for a simply-supported plate[18] as shown in Fig. 1.4. In this case, the sensors were rectangular strips of film. They have the capability of sensing the odd-odd modes of the plate and, to a lesser extent, the odd-even and even-odd modes. These sensors cannot sense the even-even modes. These sensors, therefore, can sense only those modes which have a significant contribution to the sound field. Non-collocated control was provided with a feedforward LMS (least-mean-squares) algorithm. The algorithm assumes a harmonic disturbance with location and frequency that is known *a priori*. This method of compensation is quite sensitive to both model and disturbance uncertainty.[21]

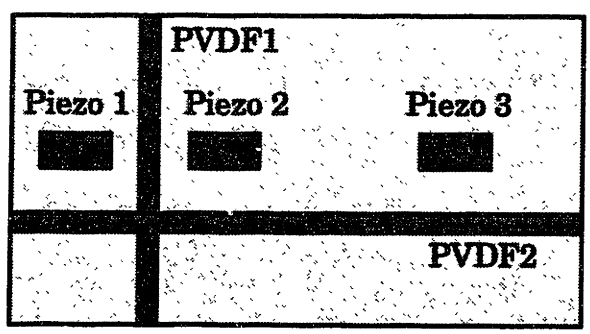

Fig. 1.4 Distributed actuator/sensor locations for feedforward LMS control of a simply-supported plate (after Clark and Fuller[18]).

Burke and Hubbard[22] conducted a theoretical study on the effects of applying a distributed transducer with a continuously varying gain over the entire surface of a plate. An example of this is shown in Fig. 1.5. The transducer is assumed to cover the entire plate. This would allow all-mode sensing and control from one sensor/actuator pair for a simply-supported plate when combined with velocity feedback. Although such a transducer is difficult to realize in practice, the concept of spatial gain weighting, referred to

as *shading*,[22,23,24] is very important for the design of transducers for plate control and will be reviewed and built upon in this thesis.

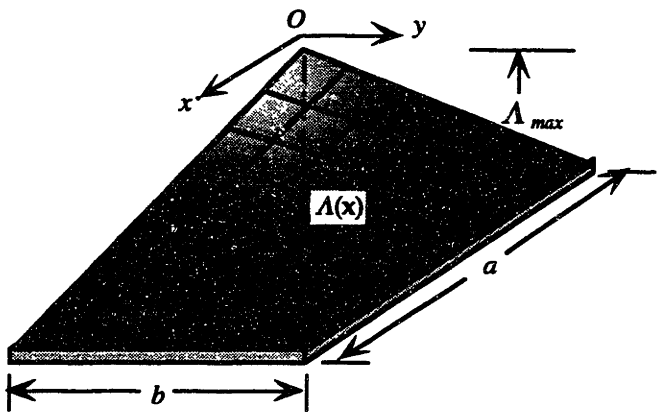

Fig. 1.5 Transducer distribution with continuously varying gain.

Many active structural control methods have recently focused on using multivariable state or output feedback along with discrete actuators and sensors. Hyland *et al.*[5] surveyed various control algorithms for space structures. They include LQG (Linear Quadratic Gaussian), LQG/LTR (Linear Quadratic Gaussian with Loop Transfer Recovery), H_∞, mixed H_2/H_∞, SSV (Structured Singular Values), and ME (Maximum Entropy). These centralized design methods produce compensators with dimensions equal to or greater than the number of plant modes within the control system bandwidth. This often leads to controllers which are practically unrealizable.

The control methods mentioned above also assume the plant can be described by a linear, time-invariant model. These control methods, however, produce conservative compensators when high model uncertainty is present.[5] In structural applications, this model is frequently developed using modal analysis. Usually, experimental modal tests of the structure are conducted and compared to high-order finite element models used to predict the mode shapes and frequencies. These methods often do not reliably describe the modal structure of a system in use.[25] Research into real-time system identification has attempted to ameliorate this problem,[26] but this too can lead to a substantial computer processing burden. The spatial design part of the problem is treated separately from the temporal control design in these

methodologies. Also, since these techniques often rely on discrete transducers, the only spatial design variables considered are the number and location of transducers.

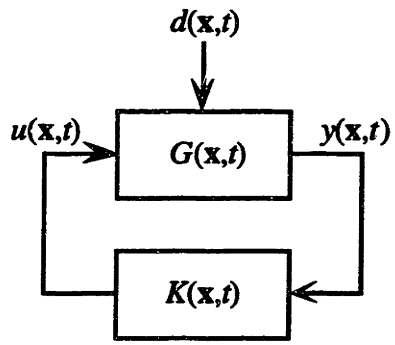

Fig. 1.6 Idealization of distributed parameter control system.

The active structural control problem involves control of distributed parameter systems, i.e. systems which involve both space and time variables. Fig. 1.6 shows an idealized block diagram of such a control system where the blocks involve spatial and temporal operators. Because of the distributed nature of the system, the compensator, $K(\mathbf{x},t)$, depends upon both space and time. Much of the previous research mentioned in this section focused on the temporal portion of the compensator, while the research which involved distributed transducers considered the spatial part of the design problem.

1.3 Objective

The objective of this thesis is to develop a general methodology which can be used to actively dampen vibrations in multidimensional elastic structures with imprecise or poorly known models and disturbance environments. The proposed means for achieving this objective is to incorporate distributed transducers. Distributed transducers offer additional spatial degrees of freedom that may be used as design variables in the control problem. One can exploit the spatial design and synthesis of distributed transducers to help accomplish the closed-loop control objectives. The technique will allow the

use of a dissipative feedback control law, such as velocity feedback, which is robust to changes in plant parameters and the disturbance environment.

1.4 Approach

A comprehensive approach for modeling two-dimensional transducers of arbitrary spatial distribution is developed. The technique is based upon the theory of multivariable distributions. This allows distributed transducer *shape* to be incorporated into the control design process for multi-dimensional structures as an additional design parameter. Also, by providing a compact, analytical representation of two-dimensional transducers, the method can be used to design new devices requiring such transducers for a variety of applications. The method itself is general and is thus applicable to many types of transducers, including piezoelectric, electrostrictive, and magnetostrictive devices.

Spatial synthesis is critical to the goal of effective structural control design.[23] For example, a discrete actuator located along a nodal line of a plate will not have any input into the corresponding mode. The primary advantage of distributed transducers is that they allow flexibility in the spatial design and synthesis for the control problem. Distributed transducers may be *shaded* by varying their gain over their spatial extent. Through the application of shaded transducers, the transducer-augmented forward-loop transfer function can be altered so as to achieve desired temporal and spatial performance goals. This work describes methods for achieving two-dimensional transducer shading using two-dimensionally shaped transducers and then discusses how these can be utilized for the control of plates.

The theoretical development is experimentally demonstrated on a thin-plate with boundary conditions that are intermediate between simply-supported and clamped. This demonstration provides insight for many classes of panel vibration problems.[27] Closed-loop active vibration control is achieved in the presence of both transient and continuous disturbances.

1.5 Organization of Thesis

A modeling approach for two-dimensional distributed transducers is developed in Chapter 2. The mathematical theory needed to describe the spatial dynamics of the transducer is developed and applied to several example problems. The results are compared with previous research and limiting cases. Guidelines for applying the technique are deduced from the various examples.

Chapter 3 uses the analytical modelling technique described in Chapter 2 to study the implications of two-dimensional transducer shape and shading for the active control of plates. Transducer shaping is shown to be an effective design tool for the control problem. The utility of continuous, two-dimensional transducer shading for establishing controllability and observability over a broad control bandwidth is also discussed. Transducer shaping can be combined with gain-weighting to provide a close approximation of a continuously shaded transducer distribution.

Chapter 4 discusses the stability of velocity feedback when combined with the spatial design work presented in Chapter 3. Plant and transducer characteristics are discussed. With collocated velocity feedback chosen as the control strategy, the marginal and asymptotic stability of the system are guaranteed.

The experimental demonstration on a thin plate is described in Chapter 5. The experimental hardware and setup is discussed. Modal tests are presented along with open-loop tests which show how the sensor and actuator distributions couple into the plate modes. Closed-loop tests are presented which demonstrate both transient and stochastic disturbance rejection.

Conclusions and recommendations for further work are presented in Chapter 6.

1.6 References

1. L. Meirovitch and S. Thangjitham, "Control of Sound Radiation From an Orthotropic Plate," in *Active Noise and Vibration Control, Proceedings of the Winter Annual Meeting of ASME*, Dallas, TE, edited by G. Warnaka *et al.* (1990).

2. R.L. Clark and C.R. Fuller, "Control of Sound Radiation with Adaptive Structures," *Journal of Intelligent Material Systems and Structures*, 2(3), pp. 431-452 (1991).

3. F. Fahy, **Sound and Structural Vibration: Radiation, Transmission and Response**, Academic Press Inc., San Diego, CA, 1989.

4. C.R. Fuller, C.H. Hansen, and S.D. Snyder, "Active Control of Sound Radiation From a Vibrating Rectangular Panel by Sound Sources and Vibration Inputs," Journal of Sound and Vibration, **145**(2), pp. 195-215 (1991).

5. D.C. Hyland, J.L. Junkins, R.W. Longman, "Active Control Technology for Large Space Structures," *Journal of Guidance, Control and Dynamics*, **16**(5), 1993.

6. R.L. Bisplinghoff and H. Ashley, **Principles of Aeroelasticity**, John Wiley & Sons Inc., New York, NY, 1962.

7. J.C. Chen, "Evaluation of Spacecraft Modal Test Methods," J. Spacecraft **24**(1), pp. 52-62, 1986.

8. E.F. Crawley, M.C. Van Schoor, and E.B. Bokhour, "The Middeck 0-gravity Dynamics Experiment Summary Report," M.I.T. Space Engineering Research Center, SERC #16-92-R, 1992.

9. T. Bailey and J.E. Hubbard, Jr., "Distributed Piezoelectric Polymer Active Vibration Control of a Cantilever Beam," *AIAA Journal of Guidance and Control*, **8**(5), pp. 605-610, 1985.

10. S.E. Burke and J.E. Hubbard, Jr., "Distributed Actuator Control Design for Flexible Beams," *Automatica*, **24**(5), pp. 619-627, 1988.

11. S. Miller and J.E. Hubbard, Jr., "Observability of a Bernoulli-Euler beam using PVF_2 as a Distributed Sensor," *Proceedings of the Sixth VPI&SU/AIAA Symposium on Dynamics and Control of Large Structures*, Blacksburg, VA, 1987.

12. J. Plump, J.E. Hubbard, Jr., and T. Bailey, "Nonlinear Control of a Distributed System: Simulation and Experimental Results," Transactions of the ASME, *Journal of Dynamic Systems, Measurement , and Control*, **109**, pp. 133-139, 1987.

13. G. Procopio and J.E. Hubbard, Jr., "Active Damping of a Bernoulli-Euler Beam via End Point Impedance Control Using Distributed Parameter Techniques," in D. Inman (Ed.), *Vibration Control and Active Vibration Suppression*, DE-Vol. 4, 11th Biennial Conference on Mechanical Vibration and Noise, Boston, MA, pp. 35-46, 1987.

14. C.K. Lee, W.W. Chiang and T.C. O'Sullivan, "Piezoelectric Modal Sensor/Actuator Pairs for Critical Active Damping Vibration Control," *Journal of the Acoustical Society of America*, 90(1), pp. 374-383, 1990.

15. D.W. Miller, S.A. Collins and S.P. Peltzman, "Development of Spatially Convolving Sensors for Structural Control Applications," *AIAA Paper*, 90-1127 -CP, pp. 2283-2297, 1990.

16. S.W. Greeley, D.J. Phillips, and D.C. Hyland, "Experimental Demonstration of the Maximum Entropy/Optimal Projection Design Theory for Active Vibration Control,"

17. C.-K. Lee and F.C. Moon, "Laminated Piezopolymer Plates for Torsion and Bending Sensors and Actuators," *Journal of the Acoustical Society of America*, **85**(6), pp. 2432-2439, 1989.

18. R.L. Clark and C.R. Fuller, "Modal Sensing of Efficient Acoustic Radiators with Polyvinylidene Fluoride Distributed Sensors in Active Structural Acoustic Approaches," *Journal of the Acoustical Society of America*, **91**(6), pp. 3321-3329, 1992.

19. R.L. Clark, R.A. Burdisso and C.R. Fuller, "Design Approaches for Shaping Polyvinylidene Fluoride Sensors in Active Structural Acoustic Control," *Journal of Intelligent Material Systems and Structures*, **4**, pp. 354-365, 1993.

20. R.L. Clark and Burke, S.E., "Practical Considerations for Designing Shaped Modal Sensors From Polyvinylidene Fluoride," submitted to *ASME Journal of Vibration and Acoustics*, 1993.

21. K. Ogata, **Modern Control Engineering**, Prentice Hall, Englewood Cliffs, N.J., 1970.

22. S.E. Burke and J.E. Hubbard, Jr., "Distributed Transducer Vibration Control of Thin Plates," *Journal of the Acoustical Society of America*, **90**(2), pp. 937-944, 1991.

23. S.E. Burke and J.E. Hubbard, Jr., "Spatial Filtering Concepts in Distributed Parameter Control," *Journal of Dynamic Systems, Measurement, and Control*, 112, pp. 565-573, December 1990.

24. S. E. Burke, "Distributed Transducer Shading: Application to Structural Control, Hydrodynamics, and Sonar Sensing," in *Smart Structures and Materials 1993: Smart Structures and Intelligent Systems*, N.W. Hagood and G.J. Knowles, Editors, Proc. SPIE 1917, pp. 1098-1112, 1993.

25. G.J. Balas and J.C. Doyle, "Identification of Flexible Structures for Robust Control," *IEEE Control Systems Magazine*, **10**(4), pp. 51-58, 1990.

26. J.E. Voss, "Real Time Identification of Large Space Structures," Ph.D. Dissertation, Massachusetts Institute of Technology, Cambridge, MA, 1987.

27. P.W. Smith, Jr., and R.H. Lyon, "Sound and Structural Vibration," National Aeronautics and Space Administration, NASA CR-160.

Chapter 2:

Modeling Approach for Two-dimensional Distributed Transducers of Arbitrary Spatial Distribution

2.1 Introduction

The benefits of using shaped, distributed transducers for the active control and sensing of beams have been explored by a number of researchers.[1-7] By varying the shape of the transducer, it is possible to weight the gain of the transducer along the length of the beam. This is an approximation, however, which breaks down when a transverse mode of vibration is present in the beam's response.

In this case, the transducer must be modeled as a two-dimensional device. Two-dimensional transducers have been considered for the active control and sensing of plates,[8,9] but only rectangular shapes or sums of rectangular shapes were considered. Lee and Moon[8] modeled rectangular pieces of piezoelectric transducers adhered to a plate with a skew angle between the piezo material axes and the boundary axes of the transducer. The boundary axes of the transducer, however, were assumed to be coincident with those of the plate. Their work showed how a finite skew angle can affect the loading/sensing parameters of the transducer.

Burke and Hubbard[9] examined the use of two-dimensional transducers for vibration control of plates with arbitrary boundary conditions. They assumed that the spatial gain of the transducer could be continuously varied, or *shaded*, over its surface area. In this work, the transducer shape was also assumed to be rectangular with boundary axes coincident with the plate axes.

In Lee and Moon[8] and Burke and Hubbard[9], products of generalized functions in orthogonal coordinates were used to model the spatial distribution

of the transducer. This procedure, however, can only accomodate transducers of rectangular shape.

This chapter describes the development and application of a method for modeling two-dimensional distributed transducers with arbitrary spatial distribution. This approach allows distributed transducer *shape* to be incorporated into the control design process for multi-dimensional structures as an additional design parameter. Also, by providing a compact representation of two-dimensional transducers, the method can be used to design new devices requiring such transducers for a wide variety of applications. The method itself is general and is thus applicable to many types of transducers, including piezoelectric, electrostrictive, and magnetostrictive devices.

The technique is based upon the theory of multivariable distributions.[10] After presenting an example of a one-dimensional shaded transducer [1-3,11] and the use of one-dimensional distributions in modeling such a device,[12] the spatial deposition of a two-dimensional transducer is defined using multidimensional distributions with composite functions as arguments. A distributional calculus is developed to determine the differential operator describing the two-dimensional transducer's spatial dynamics. The resulting modeling method is applied to several example problems and the results are compared with previous research and limiting cases. Guidelines for applying the technique are deduced from the various examples.

2.2 Theoretical Development

Many types of distributed transducers, including piezoelectric, magnetostrictive, electrostrictive, and fiber optic, are classified as *separable* transducers because their temporal dynamics do not vary over their spatial aperture.[11] Separable transducers can be represented by a product of spatial and temporal functions:

$$u(\mathbf{x},t) = \Lambda(\mathbf{x})\, u(t), \tag{2.1}$$

where $\Lambda(\mathbf{x})$ describes the transducer's spatial distribution (or spatial kernel) and $u(t)$ describes the transducer's temporal dynamics. Previous research by Burke

and Hubbard[1,11,12] has dealt with choosing a compact mathematical representation for the spatial kernel. Generalized functions, described by the theory of distributions, were used to describe both discrete and distributed transducers. The Macauley notation[13] was used to represent the generalized functions. For example, $\langle x-a\rangle^0$ represents a step function $h(x\text{-}a)$, which begins at $x = a$. The derivative with respect to x of this function is given by $\langle x-a\rangle^{-1}$. This is the delta function $\delta(x-a)$, at $x = a$. The derivative of this delta function yields $\langle x-a\rangle^{-2}$, a doublet function $\delta'(x-a)$, at $x = a$. An example from this research is presented for review.[11]

The spatial distribution of a one-dimensional distributed transducer can be weighted over the aperture [0,a] such that

$$\Lambda(x) = b\langle x\rangle^0 - \frac{b}{a}\langle x\rangle^1 + \frac{b}{a}\langle x-a\rangle^1, \tag{2.2}$$

by linearly varying the transducer's spatial input/output characteristics to decrease from some maximum, b, to zero. Note that, due to the distributed nature of the transducer, more than one generalized function is needed for the description given by (2.2).

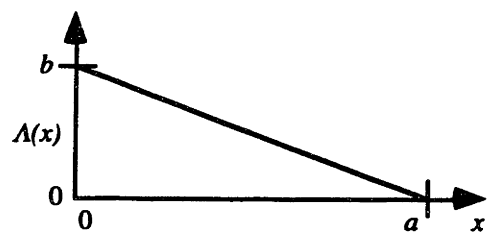

Fig. 2.1 One-dimensional shaded transducer distribution.

If the transducer described above is an induced strain device, then its spatial input/output characteristics are determined by the Laplacian of the distribution defined in (2.2),

$$\Lambda_{xx}(x) = b\langle x\rangle^{-2} - \frac{b}{a}\langle x\rangle^{-1} + \frac{b}{a}\langle x-a\rangle^{-1}. \tag{2.3}$$

The result, consisting of a doublet function and a delta function at $x = 0$ and one delta function at $x = a$, is shown in Fig. 2.2. Note that the doublet function occurs at the discontinuity in amplitude and the delta functions occur at the discontinuities in slope. If the transducer is used as an actuator, these functions would correspond to a moment and two forces, and therefore force and moment equilibrium would be satisfied. Conversely, if the transducer is used as a sensor, these functions would correspond to angular and transverse displacement respectively.

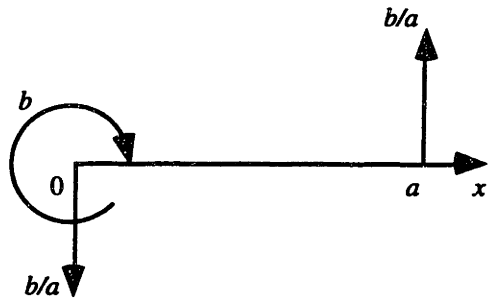

Fig. 2.2 Laplacian of one-dimensional transducer distribution.

The type of distribution shown in Fig. 2.1 has been used in the design of actuators and sensors for beams[1-3] and a variant has also been used in a center of pressure sensor[14] and a sonar sensor.[15,16] The one-dimensional shading was implemented by varying the shape of the transducer along the length of the aperture, as shown in Fig. 2.3. The shading is thus achieved by allowing the width of the transducer to linearly decrease from a maximum, Λ_{max}, at one end to a minimum, zero, at the other. Several other researchers[4-7] have used this transducer shaping technique to achieve a desired shading along the length of beams.

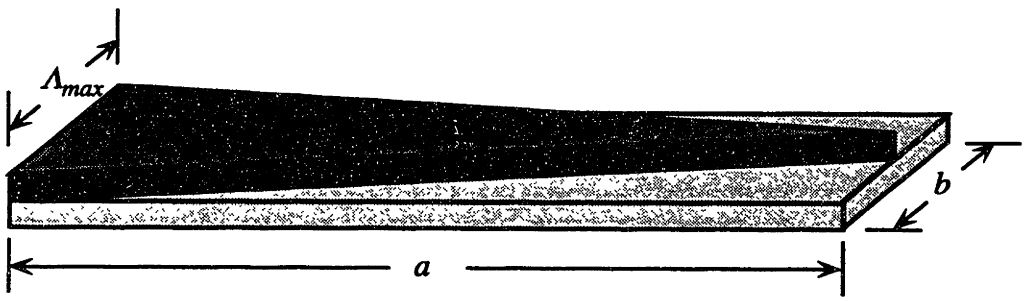

Fig. 2.3 Shaped transducer approximation of 1D shading.

This method for achieving one-dimensional shading is actually an approximation for the continuous variation of the conversion properties of the transducer over the aperture as shown in Fig. 2.4. This approximation, however, becomes invalid if the beam behaves like a plate. For example, if there are any modes of vibration along the transverse direction of the beam, then the problem is no longer one-dimensional and the shaped transducer approximation to one-dimensional shading will not be valid. In this case, the distributed transducer is two-dimensional and can no longer be modeled using one-dimensional generalized functions.

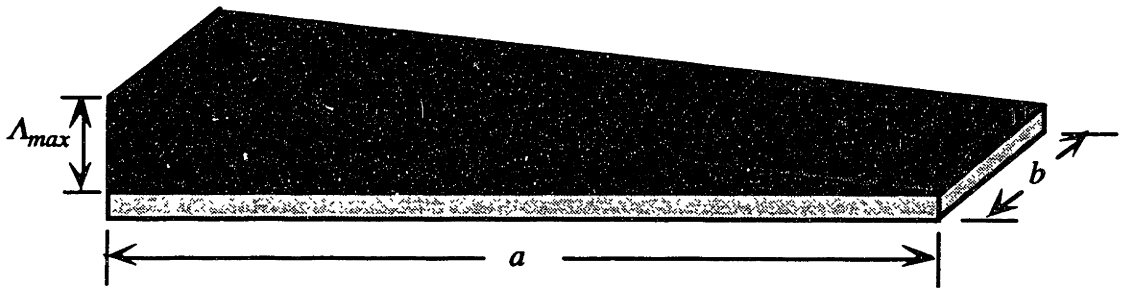

Fig. 2.4 One-dimensionally shaded transducer distribution.

It is possible to model a two-dimensional transducer using two-dimensional generalized functions. Much work has been accomplished using generalized functions for the modeling of distributed transducers in one dimension.[1-3,12] Research conducted by Lee and Moon,[8] Burke and Hubbard,[9] and Dimitriadis *et. al.*[17] has also utilized generalized functions for modeling two-dimensional transducers. This work, however, was restricted to generalized functions defined in orthogonal coordinates, and thus only rectangular shaped transducers could be examined. In the following subsection, theory is presented which enables one to use multidimensional distributions to model arbitrary transducer spatial weightings.

2.2.1 Multidimensional distributions with composite arguments

Generalized functions (distributions) defined over multi-dimensional spaces in orthogonal coordinates are discussed in Zemanian[10] and Strang.[18] For example, the delta function, $\delta(x,y)$, can be defined in two dimensions, using the inner product notation defined in Zemanian,[10] as

$$\langle \delta(x,y), \phi(x,y) \rangle = \langle \delta(x)\delta(y), \phi(x,y) \rangle = \phi(0,0). \tag{2.4}$$

This two-dimensional delta function, which is the product of a delta function in x and a delta function in y, is zero everywhere except at the origin. When operating on an ordinary function, $\phi(x,y)$, this distribution returns the value of $\phi(x,y)$, at the origin. It is also possible to have distributions which act on ordinary functions in n-dimensional real space. It is not possible, however, to multiply two distributions which are solely dependent upon the same variable.[20] For instance, neither of the two products,

$$\begin{aligned} &\delta(x)\delta(x-a), \\ &h(x-a)\delta(x), \end{aligned} \tag{2.5}$$

have a real meaning.

Now, consider the region of two-dimensional space shown in Fig. 2.5,

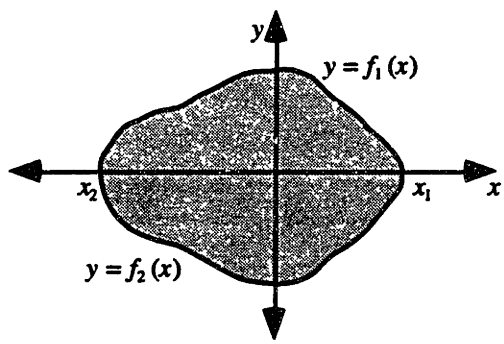

Fig. 2.5 Arbitrary closed curve in cartesian coordinates.

This region can be described by the following functions,

$$\begin{aligned} &y = f_1(x) \quad \textit{for } y > 0 \textit{ over } x \in [x_2, x_1], \\ &y = f_2(x) \quad \textit{for } y < 0 \textit{ over } x \in [x_2, x_1], \end{aligned} \tag{2.6}$$

where x_1 and x_2 are the x extrema of the boundary. In this example, the bounding functions are known for y. The situation can be reversed, i.e. knowing

$$x = g_1(y) \quad \text{for } x > 0 \text{ over } y \in [y_2, y_1],$$
$$x = g_2(y) \quad \text{for } x < 0 \text{ over } y \in [y_2, y_1], \tag{2.7}$$

where y_1 and y_2. are the y extrema of the boundary. The bounding functions in (2.6) and (2.7) have been assumed to be single-valued. If they are doubled-valued, then the region can be decomposed into *subregions* which admit either (2.6) or (2.7).

Using the functions defined in (2.6), the shape can be described by

$$\Lambda(x,y) = \left(\langle x - x_2\rangle^0 - \langle x - x_1\rangle^0\right)\left(\langle y - f_2(x)\rangle^0 - \langle y - f_1(x)\rangle^0\right). \tag{2.8}$$

Within the boundary, the distribution has unit amplitude, $\Lambda = 1$, and outside of the boundary the distribution has zero amplitude, $\Lambda = 0$. Unlike either of the products in (2.5), this expression has physical meaning because the distribution is represented by products of distributions in non-parallel coordinates. The expression can be used to describe a two-dimensional distributed transducer of arbitrary shape. If the shape is complex, then it can be separated into subregions which can be described by (2.8) and the overall representation can be derived through superposition.

If, in addition to an irregular shape, the gain of the transducer is varied over space, then the generalized functions in (2.8) may be multiplied by ordinary functions to reflect this weighting. For example, for the rectangular shape shown in Fig. 2.6,

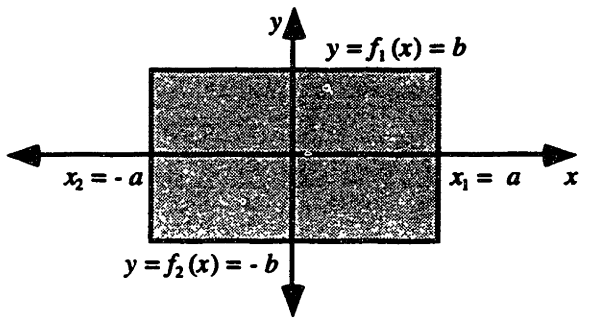

Fig. 2.6 Rectangular distribution.

equation (2.8) simplifies to

$$\Lambda(x,y) = \left(\langle x+a\rangle^0 - \langle x-a\rangle^0\right)\left(\langle y+b\rangle^0 - \langle y-b\rangle^0\right). \tag{2.9}$$

This expression is a product of distributions in orthogonal coordinates and has been used by Lee and Moon[8] and Burke and Hubbard[9] to describe a rectangular electrode distribution on piezoelectric film, and by Dimitriadis *et. al.*[17] to describe piezoceramic transducers of rectangular shape. Burke and Hubbard,[9] in designing a shaded piezoelectric film transducer, also added linear weighting in each direction,

$$\Lambda(x,y) = \frac{1}{4}\left[\left(1-\frac{x}{a}\right)\left(\langle x+a\rangle^0 - \langle x-a\rangle^0\right)\right]\left[\left(1-\frac{y}{b}\right)\left(\langle y+b\rangle^0 - \langle y-b\rangle^0\right)\right], \tag{2.10}$$

by multiplying each term by an *ordinary* function. This distribution could have been rewritten using only generalized functions as,

$$\begin{aligned}\Lambda(x,y) = &\left(\langle x+a\rangle^0 - \frac{1}{2a}\langle x+a\rangle^1 + \frac{1}{2a}\langle x-a\rangle^1\right)\times \\ &\left(\langle y+b\rangle^0 - \frac{1}{2b}\langle x+b\rangle^1 + \frac{1}{2b}\langle y-b\rangle^1\right).\end{aligned} \tag{2.11}$$

The mathematical representation defined in (2.8) can accomodate two-dimensional transducers of both arbitrary shape and gain weighting because it permits products of distributions with composite function arguments. The method is useful for directly modeling non-induced strain transducers such as piezoelectric film used in the thickness mode.[19]

In order to determine the effects of using induced strain transducers described by (2.8) in physical systems, it is necessary to derive a differentiation theorem for distributions with composite function arguments and then extend the results to multidimensions through the use of partial derivatives.

2.2.2 Differentiation of a distribution with a composite function argument: the chain rule

Given a distribution, $f(t)$, consider the meaning of that same distribution with a composite function as its argument, $f(g(t))$, where g is an ordinary function with the following properties:[10]

> The function g has an inverse h defined by $x = g(t)$ and $t = h(x)$. Both t and x are one-dimensional variables. The function g and its inverse h are infinitely smooth. The first derivative of g, and hence h, is always positive or always negative (but never zero) over the corresponding interval: $a < t < b$ and $c < x < d$. Therefore, within the given interval, the functions are not double-valued; they are either monotonically increasing or decreasing.

If $f(x)$ is a distribution defined over the interval $c < x < d$, then $f(g(t))$ is defined over the interval $a < t < b$ as[10]

$$\langle f(g(t)), \phi(t) \rangle \equiv \langle f(x), |h'(x)| \phi(h(x)) \rangle, \tag{2.12}$$

where the function $\phi(t)$ is a continuously differentiable test function with bounded support. The concept of a suitable test function is discussed further in Appendix A. This definition is derived as follows. The inner product notation is first expanded to integral notation to show the finite limits of integration,

$$\langle f(g(t)), \phi(t) \rangle = \int_a^b f(g(t))\, \phi(t)\, dt. \tag{2.13}$$

Using a change of variable under integration, where $x = g(t)$, yields

$$\begin{aligned} t &= h(x), \\ dt &= h'(x)\, dx. \end{aligned} \tag{2.14}$$

When $h'(x) > 0$, the integration limits change from $[a,b]$ to $[c,d]$. When $h'(x) < 0$, the limits change from $[a,b]$ to $[d,c]$. Substituting in for both cases yields the same result,

$$\langle f(g(t)), \phi(t) \rangle \equiv \langle f(x), |h'(x)|\, \phi(h(x)) \rangle. \tag{2.15}$$

The above result gives physical meaning to a distribution with a composite argument. To differentiate such a distribution with respect to the scalar variable, t, it is necessary to find a similar result for,

$$\left\langle \frac{d}{dt} f(g(t)), \phi(t) \right\rangle, \tag{2.16}$$

where $\phi(t)$ has support contained within $a < t < b$ and $g(t)$ is an ordinary function defined as before. Using integration by parts,

$$\left\langle \frac{d}{dt} f(g(t)), \phi(t) \right\rangle = \left\langle f(g(t)), -\frac{d}{dt}\phi(t) \right\rangle. \tag{2.17}$$

The change of variable under integration described in (2.14) will be used so the right-hand side of (2.17) is now expressed in integral form to show the limits of integration,

$$\left\langle f(g(t)), -\frac{d}{dt}\phi(t) \right\rangle = -\int_a^b f(g(t))\frac{d}{dt}[\phi(t)]dt. \tag{2.18}$$

When $h'(x) > 0$, the limits change from $[a,b]$ to $[c,d]$ and the direction of integration is unchanged. However, when $h'(x) < 0$, the limits change from $[a,b]$ to $[d,c]$ and the direction of integration is changed. Substituting in for both cases yields

$$-\int_a^b f(g(t))\frac{d}{dt}[\phi(t)]dt = -\int_c^d f(x)\,\frac{d}{dx}[\phi(h(x))]dx \qquad \text{for } h'(x) > 0, \tag{2.19}$$

$$-\int_a^b f(g(t))\frac{d}{dt}[\phi(t)]dt = \int_c^d f(x)\,\frac{d}{dx}[\phi(h(x))]dx \qquad \text{for } h'(x) < 0. \tag{2.20}$$

Integrating by parts again and combining equations (2.19) and (2.20),

$$\mp\int_c^d f(x)\,\frac{d}{dx}[\phi(h(x))]dx = \pm\int_c^d \frac{d}{dx}[f(x)]\phi(h(x))dx \qquad \text{for } h'(x) \gtrless 0. \tag{2.21}$$

Performing another change of variable back to the t domain where

$$x = g(t),$$
$$dx = g'(t)dt, \tag{2.22}$$

and subsituting in for both cases, $h'(x) > 0$ and $h'(x) < 0$, yields

$$\pm\int_c^d \frac{d}{dx}[f(x)]\phi(h(x))dx = \int_a^b \left(\frac{1}{g'(t)}\right)\frac{d}{dt}[f(g(t))]\phi(t)g'(t)dt. \tag{2.23}$$

Using the relationship,

$$g'(t)dt = d(g(t)). \tag{2.24}$$

equation (2.23) can be written as

$$\begin{aligned}\int_a^b \left(\frac{1}{g'(t)}\right)\frac{d}{dt}[f(g(t))]\phi(t)g'(t)dt &= \int_a^b \frac{d[f(g(t))]}{d(g(t))}\phi(t)g'(t)dt \\ &= \int_a^b g'(t)f'(g(t))\phi(t)dt.\end{aligned} \tag{2.25}$$

Therefore,

$$\boxed{\left\langle \frac{d}{dt} f(g(t)), \phi(t) \right\rangle = \langle g'(t)\, f'(g(t)), \phi(t) \rangle.} \tag{2.26}$$

The two distributions in (2.26) satisfy the definition of equality for distributions so that

$$\frac{d}{dt} f(g(t)) = g'(t)f'(g(t)). \tag{2.27}$$

The result is a chain rule for distributions with general substitution which works the same way as the chain rule for ordinary functions. For example, when $g(t) = at + b$, equation (2.27) reduces to

$$\frac{d}{dt} f(at + b) = af'(at + b) \qquad \text{for } a \neq 0. \tag{2.28}$$

This is a chain rule for distributions with linear substitution, and is given without a proof in Lighthill.[20] The derivative with respect to t of $\langle at+b\rangle^0$ is then

$$\frac{d}{dt}\langle at+b\rangle^0 = a\langle at+b\rangle^{-1} \qquad \text{for } a \neq 0. \tag{2.29}$$

The preceeding proof for the distributional chain rule (2.27) was derived independently. A similar result was obtained by Hoskins,[21] although the proof did not include the use of test functions. The proof was derived for the delta function as

$$\delta(x) = \frac{dh(x)}{dx} = \frac{dh(g(t))}{dt}\frac{dt}{dx} = [g'(t)]^{-1}\frac{dh(g(t))}{dt}, \tag{2.30}$$

such that

$$\frac{d}{dt}h(g(t)) = g'(t)\,\delta(g(t)). \tag{2.31}$$

The same method was used to determine the derivative of a delta function with a composite argument.

The input/output characteristics of induced strain transducers are described by a spatial differential operator. When such a transducer is two-dimensional and can be described by (2.8), the distributional chain rule (2.27) can be used to help calculate the result of the spatial differential operator. To accomodate two-dimensional induced strain transducers, however, the chain rule result must first be extended to partial differentiation in multi-dimensions. This procedure is outlined in the following subsection.

2.2.3 Extension of distributional chain rule to multi-dimensions

The spatial distribution defined in (2.8) is the product of two terms, one solely dependent upon x and the other dependent on both x and y,

$$\Lambda(x,y) = \Lambda_1(x)\,\Lambda_2(x,y). \tag{2.32}$$

When taking the partial derivative of this distribution with respect to x, it is possible to use the product rule for differentiation as long as y is assumed to be a constant,

$$\frac{\partial \Lambda(x,y)}{\partial x} = \Lambda_1'(x)\,\Lambda_2(x,y) + \Lambda_1(x)\frac{\partial \Lambda_2(x,y)}{\partial x}. \tag{2.33}$$

The partial derivative with respect to y is

$$\frac{\partial \Lambda(x,y)}{\partial y} = \Lambda_1(x)\frac{\partial \Lambda_2(x,y)}{\partial y}. \tag{2.34}$$

When taking higher-order spatial derivatives, one can apply the product rule successively:

$$\frac{\partial^2 \Lambda(x,y)}{\partial x\,\partial y} = \Lambda_1'(x)\frac{\partial \Lambda_2(x,y)}{\partial y} + \Lambda_1(x)\frac{\partial^2 \Lambda_2(x,y)}{\partial x\,\partial y}, \tag{2.35}$$

$$\frac{\partial^2 \Lambda(x,y)}{\partial x^2} = \Lambda_1''(x)\,\Lambda_2(x,y) + 2\,\Lambda_1'(x)\frac{\partial \Lambda_2(x,y)}{\partial x} + \Lambda_1(x)\frac{\partial^2 \Lambda_2(x,y)}{\partial x^2}, \tag{2.36}$$

$$\frac{\partial^2 \Lambda(x,y)}{\partial y^2} = \Lambda_1(x)\frac{\partial^2 \Lambda_2(x,y)}{\partial y^2}. \tag{2.37}$$

Using the distributional chain rule defined in (2.27), where y is again assumed to be a constant, the partial derivative of $\Lambda(x,y)$ defined in (2.8) with respect to x can be written as,

$$\begin{aligned}\frac{\partial \Lambda(x,y)}{\partial x} &= \left(\langle x-x_2\rangle^{-1} - \langle x-x_1\rangle^{-1}\right)\left(\langle y-f_2(x)\rangle^0 - \langle y-f_1(x)\rangle^0\right)\\ &+ \left(\langle x-x_2\rangle^0 - \langle x-x_1\rangle^0\right)\left(-f_2'(x)\langle y-f_2(x)\rangle^{-1} + f_1'(x)\langle y-f_1(x)\rangle^{-1}\right).\end{aligned} \tag{2.38}$$

The partial derivative of $\Lambda(x,y)$ with respect to y is simply,

$$\frac{\partial \Lambda(x,y)}{\partial y} = \left(\langle x-x_2\rangle^0 - \langle x-x_1\rangle^0\right)\left(\langle y-f_2(x)\rangle^{-1} - \langle y-f_1(x)\rangle^{-1}\right). \tag{2.39}$$

Of course, the spatial distributions of distributed transducers may be more complicated than defined in equation (2.8). If the transducer is shaded, the spatial distribution may include ordinary functions or higher order generalized functions. However, one can simply use the distributional chain rule and the product rule for differentiation as needed when taking partial derivatives.

2.3 Application to Two-Dimensional Problems

The theory presented in the preceeding section can be used to calculate the spatial differential operator of an induced strain transducer. In this section, spatial distributions of piezoelectric material will be examined to allow comparisons of the modeling technique to previous research in the field. The differential operator describing the spatial dynamics of piezopolymer film (PVDF), with the possibility of skew angle, θ, between the transducer and structure axes, is given by Lee and Moon[8]

$$L[\Lambda(x,y)] = e_{31}^0 \frac{\partial^2 \Lambda(x,y)}{\partial^2 x} + e_{32}^0 \frac{\partial^2 \Lambda(x,y)}{\partial^2 y} + e_{36}^0 \frac{\partial^2 \Lambda(x,y)}{\partial x \, \partial y}, \tag{2.40}$$

$$\begin{bmatrix} e_{31}^0 \\ e_{32}^0 \\ e_{36}^0 \end{bmatrix} = \begin{bmatrix} \cos^2\theta & \sin^2\theta & -2\cos\theta\sin\theta \\ \sin^2\theta & \cos^2\theta & 2\cos\theta\sin\theta \\ \cos\theta\sin\theta & -\cos\theta\sin\theta & \cos^2\theta - \sin^2\theta \end{bmatrix} \times \begin{bmatrix} Y_p/(1-\nu_p^2) & \nu_p Y_p/(1-\nu_p^2) & 0 \\ \nu_p Y_p/(1-\nu_p^2) & Y_p/(1-\nu_p^2) & 0 \\ 0 & 0 & Y_p/2(1+\nu_p) \end{bmatrix} \begin{bmatrix} d_{3'1'}^0 \\ d_{3'2'}^0 \\ 0 \end{bmatrix}, \tag{2.41}$$

where $e_{31}^0, e_{32}^0, e_{36}^0$ represent the piezoelectric stress/charge constants with respect to the structure axes; $d_{3'1'}^0, d_{3'2'}^0$ are the piezoelectric strain/charge constants with respect to the PVDF material axes; and Y_p, ν_p are the Young's modulus and Poisson's ratio respectively of PVDF. The examples of two-dimensional shaped transducers presented in the following subsections are based upon PVDF film.

2.3.1 Application to triangular shaped transducer distribution

Consider the triangular shaped piezoelectric distribution shown in Fig. 2.7 where the magnitude of the slope of the taper, m, is equal to b/a.

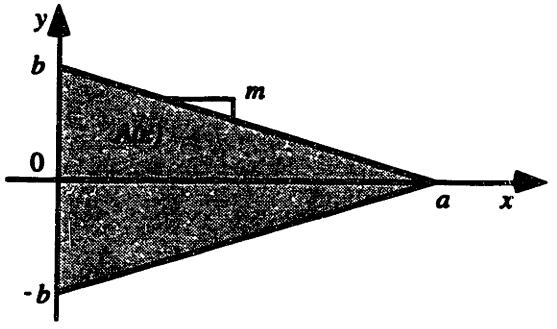

Fig. 2.7 Triangular shaped distribution.

This shape can be represented using equation (2.8), where $f_1(x) = -mx + b$ *and* $f_2(x) = +mx - b$;

$$\Lambda(\mathbf{x}) = \Lambda(x,y) = \big(\langle x\rangle^0 - \langle x-a\rangle^0\big)\big(\langle y-(mx-b)\rangle^0 - \langle y-(-mx+b)\rangle^0\big). \quad (2.42)$$

Equation (2.42) describes a distribution that is "on" with unit intensity only when x is within the range $0 < x < a$ and y is within the range $(mx - b) < y < (-mx + b)$. The location of the origin is arbitrary but has been chosen as shown for convenience. This distribution can be rewritten as

$$\Lambda(x,y) = \big(\langle x\rangle^0 - \langle x-a\rangle^0\big)\big(\langle y-mx+b\rangle^0 - \langle y+mx-b\rangle^0\big). \quad (2.43)$$

Assume that this distribution is either a triangular shaped piezoelectric transducer or electrode distribution on a piezoelectric transducer where the material axes of the transducer are coincident with the x and y axes shown in Fig. 2.7 (skew angle is zero). The result of the piezoelectric operator (2.40) acting on this distribution may be found through the use of equations (2.33) - (2.39) and the distributional chain rule for linear substitution (2.27),

$$
\begin{aligned}
L[\Lambda(x,y)] = {} & e_{31}^{0}\left(\langle x\rangle^{-2} - \langle x-a\rangle^{-2}\right)\left(\langle y-mx+b\rangle^{0} - \langle y+mx-b\rangle^{0}\right) \\
& - 2me_{31}^{0}\left(\langle x\rangle^{-1} - \langle x-a\rangle^{-1}\right)\left(\langle y-mx+b\rangle^{-1} + \langle y+mx-b\rangle^{-1}\right) \\
& + \left(m^{2}e_{31}^{0} + e_{32}^{0}\right)\left(\langle x\rangle^{0} - \langle x-a\rangle^{0}\right)\left(\langle y-mx+b\rangle^{-2} - \langle y+mx-b\rangle^{-2}\right).
\end{aligned}
\tag{2.44}
$$

The magnitudes of the last two terms in equation (2.44) depend on the slope of the lines and not on the x or y intercepts. Thus, the location of the origin of the coordinate system does not affect the result. The physical interpretation of this result is shown in Fig 2.8.

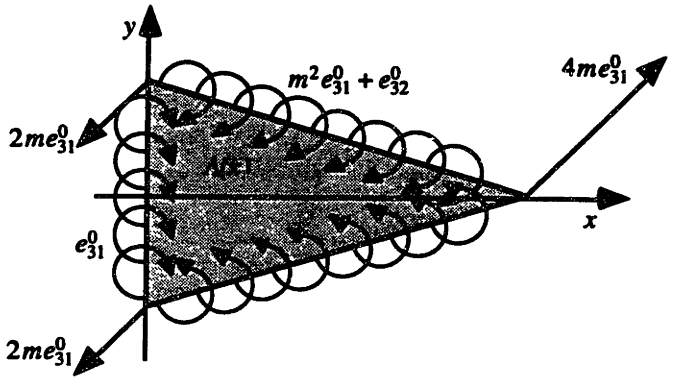

Fig. 2.8 Result of piezoelectric operator acting on triangular distribution.

The first term in equation (2.44) contributes distributed doublet functions of magnitude e_{31}^{0} on the lines $x = 0$ and $x = a$, but only within the lines $y = mx - b$ and $y = -mx + b$. Because the sloped lines intersect at the point $(a, 0)$, no doublet functions exist on the right hand boundary of the triangle. The third term contributes distributed doublet functions of magnitude $m^2e_{31}^{0} + e_{32}^{0}$ along the lines $y = mx - b$ and $y = -mx + b$, but only within the lines $x = 0$ and $x = a$. The second term in equation (2.44) gives downward delta functions of magnitude $2me_{31}^{0}$ at the points $(0, b)$ and $(0, -b)$ and an upward delta function of $4me_{31}^{0}$ at the point $(a, 0)$. Doublet functions line the boundary, where there is a discontinuity in amplitude of the distribution, and delta functions occur at discontinuities in boundary slope.

Burke and Hubbard[1] and Miller and Hubbard[2] cut PVDF in this shape to approximate the linear shading in one dimension, as described by equation (2.2).

The resulting one-dimensional Laplacian was given in (2.3) and shown in Fig. 2.2. The approximation made is seen to be correct by comparing the results with those given in equation (2.44) and shown in Fig. 2.8. The two-dimensional description approaches the one-dimensional Laplacian as the two-dimensional structure the transducer is attached to or embedded within approaches a one-dimensional system. The structure will become very "stiff" in the y-direction as this limit is approached. Thus, the two delta functions on the left vertices in Fig. 2.8 sum to one which is equal in magnitude but opposite in direction from the delta function at the right vertex. Due to stiffness in the y-direction, the bending effect of the doublet functions along the sloped lines becomes negligible in comparison to that of the distributed moment along the left boundary. The distributed doublet functions along the left boundary can be summed to give one resultant doublet function acting in opposition to the delta function at the right vertex.

The differential operator result for this distribution also reduces to a known result when looking at the limit as the slope of the taper, m, approaches zero. When this occurs, the distribution itself approaches a rectangular distribution,

$$\Lambda(x,y) = \left(\langle x\rangle^{0} - \langle x-a\rangle^{0}\right)\left(\langle y+b\rangle^{0} - \langle y-b\rangle^{0}\right), \tag{2.45}$$

and the differential operator result approaches

$$\begin{aligned} L[\Lambda(x,y)] = {} & e_{31}^{0}\left(\langle x\rangle^{-2} - \langle x-a\rangle^{-2}\right)\left(\langle y+b\rangle^{0} - \langle y-b\rangle^{0}\right) \\ & + e_{32}^{0}\left(\langle x\rangle^{0} - \langle x-a\rangle^{0}\right)\left(\langle y+b\rangle^{-2} - \langle y-b\rangle^{-2}\right). \end{aligned} \tag{2.46}$$

The result agrees with that reported by Lee and Moon,[8] Burke and Hubbard,[9] and Dimitriadis *et. al.*[17] The magnitude of the distributed doublet functions along the lines $y = mx - b$ and $y = -mx + b$ approaches e_{32}^{0} and the magnitudes of the delta functions at the vertices approach zero as m approaches zero. Therefore, as the slope of the taper, m, approaches zero, the differential operator result approaches that of a uniform rectangular distribution with distributed moments along the boundaries and no delta functions at any of the corners.

One can see from this exercise that, because the transducer shape is symmetric about the x-axis, it is best to define the distribution as in equation

(2.43). For any given x within $[0,a]$, there are two possible values of y. Therefore, the shape cannot be defined in terms of unique functions of y as in equation (2.7). One could, however, break up the shape into two parts along the x-axis, examine the differential operator result of each, and sum the results. The top shape could be defined as,

$$\Lambda(x,y) = \left(\langle x\rangle^0 - \langle x + y/m - a\rangle^0\right)\left(\langle y\rangle^0 - \langle y - b\rangle^0\right), \tag{2.47}$$

and the bottom shape could be defined in a similar manner. However, the limit of this distribution as m approaches zero does not approach a rectangular distribution because $(1/m)$ approaches infinity. Therefore, one can deduce that equation (2.47) is not a suitable representation of the upper part of the shape shown in Fig. 2.7. A general guideline for defining distributions of irregular shape is that the limit, as a parameter describing the shape approaches some nominal value, exist and conform to the distribution describing the nominal shape.

Up to this point, the type of piezoelectric material, uniaxial or biaxial, used to create the tapered distribution has not been specified. The difference between these two materials lies in the values of the strain/charge constants, $d^0_{3'1'}, d^0_{3'2'}$. The stress/charge constants, calculated from equation (2.41) for zero skew angle, are related to the strain/charge constants by the following relation,

$$\begin{bmatrix} e^0_{31} \\ e^0_{32} \\ e^0_{36} \end{bmatrix} = \begin{bmatrix} q d^0_{3'1'} + \nu_p q d^0_{3'2'} \\ \nu_p q d^0_{3'1'} + q d^0_{3'2'} \\ 0 \end{bmatrix}, \tag{2.48}$$

where

$$q = Y_p/(1-\nu_p^2). \tag{2.49}$$

For uniaxial, piezoelectric "KYNAR" film [22], $d^0_{3'1'} = 24\times10^{-12}\, m/V\ (or\ C/N)$ and $d^0_{3'2'} = 3\times10^{-12}\, m/V\ (or\ C/N)$ so that the stress/charge constants are[20]

$$\begin{bmatrix} e_{31}^0 \\ e_{32}^0 \\ e_{36}^0 \end{bmatrix} = \begin{bmatrix} 2.40\times10^{-11} \\ 1.07\times10^{-11} \\ 0 \end{bmatrix} q. \tag{2.50}$$

For biaxial, piezoelectric "SOLEF" film[23], $d_{3'1'}^0 = d_{3'2'}^0 = (6\text{–}10)\times10^{-12}\, m/V$ (*or* C/N) so the maximum stress/charge constants are[21]

$$\begin{bmatrix} e_{31}^0 \\ e_{32}^0 \\ e_{36}^0 \end{bmatrix} = \begin{bmatrix} 1.33\times10^{-11} \\ 1.33\times10^{-11} \\ 0 \end{bmatrix} q. \tag{2.51}$$

Using these values, the ratio of the magnitudes of the doublet functions, $e_{31}^0 m^2 + e_{32}^0$, along the sloped lines of the taper is

$$\frac{uniaxial\ mag}{biaxial\ mag} = \frac{24m^2+11}{13.3\,(m^2+1)} \approx \frac{12\,(2m^2+1)}{13.3\,(m^2+1)}. \tag{2.52}$$

This ratio varies between 0.83 and 1.3 for m between 0 and 1 respectively. With uniaxial film it is therefore possible to obtain the same magnitude of distributed doublet functions along the sloped edges of the taper as with biaxial film. Thus, it is possible to achieve a two-dimensional loading/sensing effect with uniaxial film by cutting the film or shaping the electrodes in a direction which is nonorthogonal to the rolling axis of the film. Uniaxial film is simpler to manufacture than biaxial film and is therefore more readily available and cost-effective as a transducer. This agrees with research by Lee [8] where varying the skew axis of the film with respect to a rectangular boundary produced two dimensional loading/sensing effects.

2.3.2 Application to rectangular transducer distribution with finite skew angle of material axes

The modeling method can be applied to the distribution shown in Fig. 2.9 to provide a comparison with results obtained by Lee and Moon.[8] Their research

showed, based upon piezoelectric laminate theory, that the e_{36}^0 stress/charge constant in the piezoelectric differential operator (2.40) could be generated by skewing the material axes of the transducer with respect to the laminate by an angle θ. This stress/charge constant weights the cross term in (2.40) and causes the equivalent of delta functions to be produced at the corners of a rectangular distribution. In addition, varying the skew angle causes all of the stress/charge constants to vary in a sinusoidal manner with increasing skew angle. The distribution shown in Fig. 2.9 has material axes which are coincident with the x and y axes shown in the figure, but the geometric axes of the rectangle, x_r and y_r, are skewed with respect to the x and y axes.

This is analogous to the distribution shown in Fig. 2.10 where the material axes are skewed with respect to the x and y axes but the geometric axes of the rectangle are coincident those axes. The distribution in Fig. 2.10 has stress/charge constants given by equation (2.41) where the skew angle is a finite θ, and the distribution in Fig. 2.9 has stress charge constants given by (2.41) where the skew angle is equal to zero as shown in equations (2.48) and (2.49). Since the boundary itself in Fig. 2.9 is skewed, multi-dimensional distributions, with $\cos\theta$ and $\sin\theta$ included in the arguments, are needed to describe the shape. Differentiation of these composite distributions will produce the cross-terms, resulting in delta functions at the corners, and will correctly weight the doublet functions acting along the boundary. Analyzing the piezoelectric operator results for both distributions will provide an effective correlation of this work with that of Lee and Moon[8].

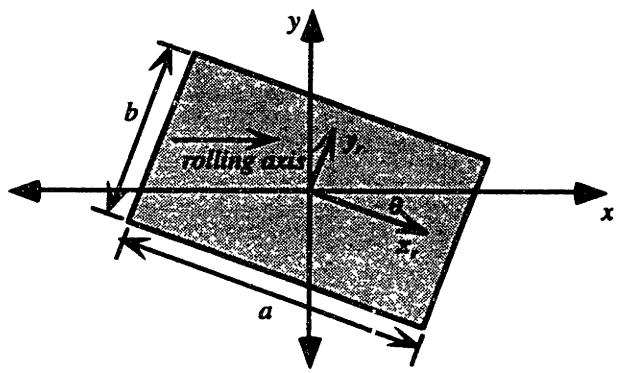

Fig. 2.9 Rectangular distribution with skewed boundary.

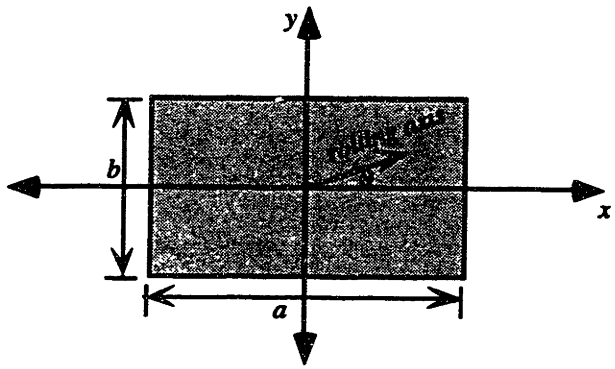

Fig. 2.10 Rectangular distribution with skewed material axes.

Define the distribution shown in Fig. 2.9 using the geometric axes with the following coordinate transformation to the material axes,

$$\begin{aligned} x_r &= x\cos\theta - y\sin\theta, \\ y_r &= y\cos\theta + x\sin\theta. \end{aligned} \tag{2.53}$$

The distribution is defined in terms of these coordinates as

$$\Lambda(x_r,y_r) = \left(\langle x_r + a/2\rangle^0 - \langle x_r - a/2\rangle^0\right)\left(\langle y_r + b/2\rangle^0 - \langle y_r - b/2\rangle^0\right). \tag{2.54}$$

Since the choice of coordinates does not affect the amplitude of the distribution,

$$\Lambda(x_r,y_r) = \Lambda(x,y). \tag{2.55}$$

Defining the distribution in terms of x and y with the coordinate transformation (2.53) yields

$$\begin{aligned} \Lambda(x,y) = &\left(\langle x\cos\theta - y\sin\theta + a/2\rangle^0 - \langle x\cos\theta - y\sin\theta - a/2\rangle^0\right) \\ &\times\left(\langle y\cos\theta + x\sin\theta + b/2\rangle^0 - \langle y\cos\theta + x\sin\theta - b/2\rangle^0\right). \end{aligned} \tag{2.56}$$

This definition is valid since the limit of $\Lambda(x,y)$ as θ approaches zero reduces to

$$\Lambda(x,y) = \left(\langle x + a/2\rangle^0 - \langle x - a/2\rangle^0\right)\left(\langle y + b/2\rangle^0 - \langle y - b/2\rangle^0\right), \tag{2.57}$$

and the limit as θ approaches $\pi/2$ reduces to

$$\Lambda(x,y) = \left(\langle y + a/2\rangle^0 - \langle y - a/2\rangle^0\right)\left(\langle x + b/2\rangle^0 - \langle x - b/2\rangle^0\right). \tag{2.58}$$

The distribution involves two terms which are *both* dependent on x and y,

$$\Lambda(x,y) = \Lambda_1(x,y)\Lambda_2(x,y). \tag{2.59}$$

Because of the added y dependence in Λ_1, the second derivative with respect to x is now

$$\frac{\partial^2\Lambda(x,y)}{\partial x^2} = \frac{\partial^2\Lambda_1(x,y)}{\partial x^2}\Lambda_2(x,y) + 2\frac{\partial\Lambda_1(x,y)}{\partial x}\frac{\partial\Lambda_2(x,y)}{\partial x} + \Lambda_1(x)\frac{\partial^2\Lambda_2(x,y)}{\partial x^2}, \tag{2.60}$$

and the second derivative with respect to y is,

$$\frac{\partial^2\Lambda(x,y)}{\partial y^2} = \frac{\partial^2\Lambda_1(x,y)}{\partial y^2}\Lambda_2(x,y) + 2\left(\frac{\partial\Lambda_1(x,y)}{\partial y}\right)\left(\frac{\partial\Lambda_2(x,y)}{\partial y}\right) + \Lambda_1(x,y)\frac{\partial^2\Lambda_2(x,y)}{\partial y^2}. \tag{2.61}$$

The piezoelectric operator for the distribution in Fig. 2.9 (zero skew angle of material axes) is

$$L[\Lambda(x,y)] = e_{31}^0\frac{\partial^2\Lambda(x,y)}{\partial^2 x} + e_{32}^0\frac{\partial^2\Lambda(x,y)}{\partial^2 y}, \tag{2.62}$$

where

$$\begin{aligned}\frac{\partial^2\Lambda(x,y)}{\partial x^2} = {} & \cos^2\theta\left(\langle x\cos\theta - y\sin\theta + a/2\rangle^{-2} - \langle x\cos\theta - y\sin\theta - a/2\rangle^{-2}\right) \\ & \times\left(\langle y\cos\theta + x\sin\theta + b/2\rangle^{0} - \langle y\cos\theta + x\sin\theta - b/2\rangle^{0}\right) \\ & + 2\cos\theta\sin\theta\left(\langle x\cos\theta - y\sin\theta + a/2\rangle^{-1} - \langle x\cos\theta - y\sin\theta - a/2\rangle^{-1}\right) \\ & \times\left(\langle y\cos\theta + x\sin\theta + b/2\rangle^{-1} - \langle y\cos\theta + x\sin\theta - b/2\rangle^{-1}\right) \\ & + \sin^2\theta\left(\langle x\cos\theta - y\sin\theta + a/2\rangle^{0} - \langle x\cos\theta - y\sin\theta - a/2\rangle^{0}\right) \\ & \times\left(\langle y\cos\theta + x\sin\theta + b/2\rangle^{-2} - \langle y\cos\theta + x\sin\theta - b/2\rangle^{-2}\right),\end{aligned} \tag{2.63}$$

and

$$\begin{aligned}\frac{\partial^2 \Lambda(x,y)}{\partial y^2} &= \sin^2\theta\left(\langle x\cos\theta - y\sin\theta + a/2\rangle^{-2} - \langle x\cos\theta - y\sin\theta - a/2\rangle^{-2}\right) \\ &\quad\times\left(\langle y\cos\theta + x\sin\theta + b/2\rangle^{0} - \langle y\cos\theta + x\sin\theta - b/2\rangle^{0}\right) \\ &\quad - 2\cos\theta\sin\theta\left(\langle x\cos\theta - y\sin\theta + a/2\rangle^{-1} - \langle x\cos\theta - y\sin\theta - a/2\rangle^{-1}\right) \\ &\quad\times\left(\langle y\cos\theta + x\sin\theta + b/2\rangle^{-1} - \langle y\cos\theta + x\sin\theta - b/2\rangle^{-1}\right) \\ &\quad + \cos^2\theta\left(\langle x\cos\theta - y\sin\theta + a/2\rangle^{0} - \langle x\cos\theta - y\sin\theta - a/2\rangle^{0}\right) \\ &\quad\times\left(\langle y\cos\theta + x\sin\theta + b/2\rangle^{-2} - \langle y\cos\theta + x\sin\theta - b/2\rangle^{-2}\right).\end{aligned} \tag{2.64}$$

The stress/charge constants are given by equation (2.41) with $\theta = 0$:

$$\begin{bmatrix} e_{31}^0 \\ e_{32}^0 \\ e_{36}^0 \end{bmatrix} = \begin{bmatrix} q d_{3'1'}^0 + \nu_p q d_{3'2'}^0 \\ \nu_p q d_{3'1'}^0 + q d_{3'2'}^0 \\ 0 \end{bmatrix}, \tag{2.65}$$

where

$$q = Y_p/(1-\nu_p^2). \tag{2.66}$$

The results of this operation on the distribution are shown in Fig. 2.11. The result of the piezoelectric operator acting on the distribution shown in Fig. 2.10 is given by

$$\begin{aligned}L[\Lambda(x,y)] &= q\left[\cos^2\theta\left(d_{3'1'}^0 + \nu_p d_{3'2'}^0\right) + \sin^2\theta\left(\nu_p d_{3'1'}^0 + d_{3'2'}^0\right)\right] \\ &\quad\times\left(\langle x + a/2\rangle^{-2} - \langle x - a/2\rangle^{-2}\right)\left(\langle y + b/2\rangle^{0} - \langle y - b/2\rangle^{0}\right) \\ &\quad - 2\cos\theta\sin\theta\, q\left(d_{3'1'}^0 + \nu_p d_{3'2'}^0 - \nu_p d_{3'1'}^0 - d_{3'2'}^0\right) \\ &\quad\times\left(\langle x + a/2\rangle^{-1} - \langle x - a/2\rangle^{-1}\right)\left(\langle y + b/2\rangle^{-1} - \langle y - b/2\rangle^{-1}\right) \\ &\quad + q\left[\sin^2\theta\left(d_{3'1'}^0 + \nu_p d_{3'2'}^0\right) + \cos^2\theta\left(\nu_p d_{3'1'}^0 + d_{3'2'}^0\right)\right] \\ &\quad\times\left(\langle x + a/2\rangle^{0} - \langle x - a/2\rangle^{0}\right)\left(\langle y + b/2\rangle^{-2} - \langle y - b/2\rangle^{-2}\right),\end{aligned} \tag{2.67}$$

and is shown in Fig. 2.12. The $\cos\theta$ and $\sin\theta$ terms multiplying the generalized functions in (2.67) were obtained from the nonzero skew angle assumption in equation (2.41). The $\cos\theta$ and $\sin\theta$ terms in equations (2.63) and (2.64) were obtained when taking distributional derivatives of generalized functions with composite arguments involving $\cos\theta$ and $\sin\theta$. Yet, the magnitudes and orientation of the doublet functions along the boundary and the delta functions at the corners match for *both* distributions. Thus, the modeling method developed herein agrees with results obtained by Lee and Moon.[8]

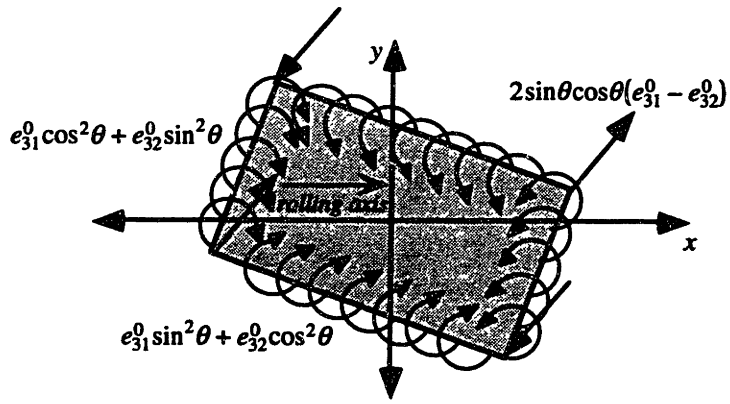

Fig. 2.11 Piezoelectric operator acting on rectangular distribution with skewed boundary.

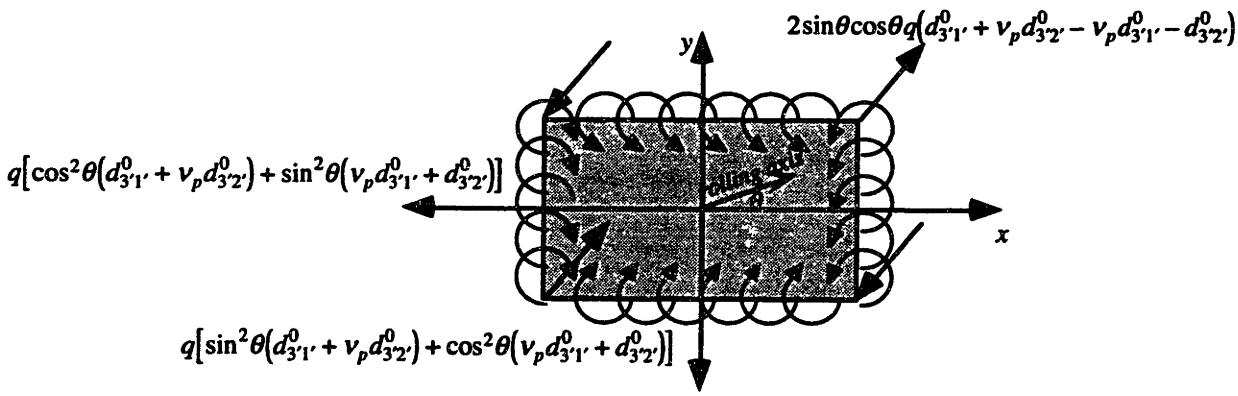

Fig. 2.12 Piezoelectric operator acting on rectangular distribution with skewed material axes.

2.4 Summary and application to structural control

A new modeling technique for two-dimensional distributed transducers was presented. This approach allows distributed transducer shape to be incorporated into the control design process for multi-dimensional structures as an additional design parameter. The method is applicable to many types of strain-inducing transducers, such as piezoelectric, electrostrictive, and magnetostrictive materials. The derivation was based upon the theory of multivariable distributions and was extended to distributions with composite functions as arguments. In this manner, arbitrary spatial weightings of transducers could be described. A differentiation theorem for such distributions was developed and used to calculate the spatial differential operator for a strain-inducing transducer. Several applications were presented to show the utility of this technique and compare the results to previous research in the field.

This modeling method was used to verify shaping techniques developed previously to approximate one-dimensional transducer shading. It was also shown that two-dimensional delta and doublet function distributions could be obtained even when using a uniaxial transducer if the boundaries of the transducer (or electrode) were shaped to be nonorthogonal to the material axes. The approach is in exact agreement with previous work by Lee and Moon where they demonstrated that when the material axes of a transducer are skewed with respect to the rectangular boundary axes of an PVDF electrode distribution, both delta and doublet function distributions are obtained. Guidelines for defining spatial transducer distributions using generalized functions with composite arguments were also established.

In the next chapter, this modeling technique will be used to help determine the effects of using shaped transducers to control and sense Bernoulli-Euler plates. Because this technique is analytical, it is quite useful in calculating the modal coefficients of various transducer distributions for plates with known boundary conditions. These modal coefficients can then be used to determine the controllability/observability characteristics of the transducer distribution.

2.5 References

1. S.E. Burke and J.E. Hubbard, Jr., "Active Vibration Control of a Simply Supported Beam Using a Spatially Distributed Actuator," *IEEE Control Systems Magazine*, pp. 25-30, August 1987.

2. S.E. Miller and J.E. Hubbard, Jr., "Observability of a Bernoulli-Euler Beam Using PVF_2 as a Distributed Sensor," *Proceedings of the 6th. VPI&SU/AIAA Symposium on Dynamics and Control of Large Structures*, Blacksburg, VA, edited by L. Meirovitch, June 1987.

3. S.E. Burke and J.E. Hubbard, Jr., "Distributed Actuator Control Design for Flexible Beams," *Automatica*, **24**(5), pp.619-627, 1988.

4. C.K. Lee and F.C. Moon, "Modal Sensors/Actuators," *ASME Journal of Applied Mechanics*, Vol. 57, pp. 434-441, June, 1990.

5. C.K. Lee, W.W. Chiang and T.C. O'Sullivan, "Piezoelectric Modal Sensors and Actuators Achieving Critical Active Damping on a Cantilever Plate," *AIAA Paper*, 89-1390-CP, pp. 2018-2026, April 1989.

6. C.K. Lee, W.W. Chiang and T.C. O'Sullivan, "Piezoelectric Modal Sensor/Actuator Pairs for Critical Active Damping Vibration Control," *Journal of the Acoustical Society of America*, 90(1), pp. 374-383, 1990.

7. D.W. Miller, S.A. Collins and S.P. Peltzman, "Development of Spatially Convolving Sensors for Structural Control Applications," *AIAA Paper*, 90-1127 -CP, pp. 2283-2297, 1990.

8. C.-K. Lee and F.C. Moon, "Laminated Piezopolymer Plates for Torsion and Bending Sensors and Actuators," *Journal of the Acoustical Society of America*, **85**(6), pp. 2432-2439, June 1989.

9. S.E. Burke and J.E. Hubbard, Jr., "Distributed Transducer Vibration Control of Thin Plates," *Journal of the Acoustical Society of America* , **90**(2), pp. 937-944, August 1991.

10. A.H. Zemanian, Distribution Theory and Transform Analysis: An Introduction to Generalized Functions, with Applications, chs. 1-2, McGraw-Hill, New York, 1965; reprint ed., Dover Publications Inc., Mineola, NY, 1987.

11. S.E. Burke and J.E. Hubbard, Jr., "Distributed Transducers for Structural Measurement and Control," *Advances in Control and Dynamic Systems*, C.T. Leondes (Ed.), Vol. 36, pp. 223-272, 1990.

12. J.E. Hubbard, Jr., "Distributed Transducers for Smart Structural Components," *Proceedings of the 6th. International Modal Analysis Conference*, Kissimee, FL, pp. 856-862, 1988.

13. S.H. Crandall, An Introduction to the Mechanics of Solids, McGraw-Hill, New York, 1972.

14. J.E. Hubbard, Jr. and S.E. Burke, "Pressure Distribution Characterization System," *United States Patent No.* 5,054,323, October 1991.

15. S.E. Burke and P.A. Rosenstrach, "High Resolution Monopulse Piezopolymer Sonar Sensor," *Proceedings of the 1992 Symposium on Autonomous Underwater Vehicle Technology*, S. Dunn (Ed.), Washington, D.C., pp. 209-214, June 1992.

16. S.E. Burke and J.E. Hubbard Jr., "Wideband, Derivative-Matched, Continuous Aperture Acoustic Transducer", United States Patent No. 5,237,542, August 1993.

17. E.K. Dimitriadis, C.R. Fuller, and C.A. Rogers, "Piezoelectric Actuators for Distributed Noise and Vibration Excitation of Thin Plates," *Proceedings of the Eigth Biennial Conference on Failure Prevention and Reliability*, Montreal, Canada, pp. 223-233 (September, 1989).

18. G. Strang, Introduction To Applied Mathematics, Wellesley-Cambridge Press, Cambridge, MA, 1986.

19. S. Burke, "Monopulse Sensor 3-D Beam Pattern Analysis", Draper Laboratory Technical Memorandum ETB-92-378, 29 July 1992.

20. M.J. Lighthill, An Introduction To Fourier Analysis and Generalized Functions, Cambridge University Press, Cambridge, 1958.

21. R.F. Hoskins, Generalised Functions, Ellis Horwood Limited, West Sussex, 1979.

22. Kynar Piezo Film Technical Manual, Pennwalt Corporation, 1985.

23. "Piezoelectric SOLEF PVDF Polyvinylidene Flouride Films," *Piezo News*, Solvay Technologies Inc., 1985.

Chapter 3:

Distributed Transducer Design for Plates: Spatial Shape and Shading as Design Parameters

3.1 Introduction

Several researchers have examined the use of distributed transducers for the active control of two-dimensional structures.[1-3] The possible applications include both vibration suppression and acoustic radiation attenuation. The primary advantage of distributed transducers is that they can be shaded by varying their gain over their spatial extent. Through the application of shaded transducers, the transducer-augmented forward-loop transfer function can be altered so as to achieve desired temporal and spatial performance goals.[4] This chapter describes methods for achieving two-dimensional transducer shading using *two-dimensionally* shaped transducers.

The previous chapter included the development of an analytical method for modelling two-dimensionally shaped transducers. The method will be used in this chapter to aid in the design of two-dimensional transducer distributions for the active control of plates. Because the method is analytical, much insight is obtained into the physics of the interaction between the shaped transducer and mode shapes in a plate.

Shaped sensors and actuators have previously been utilized for mode targeting, loop shaping, and for all-mode sensing and control for beams.[5-11] Because these transducers were applied to beams, no transverse modes of vibration were present, and the shapes were good approximations of continuous, one-dimensional shading. Burke and Hubbard[5] and Miller and Hubbard[6] developed a design methodology for shaded transducers to accomplish all-mode sensing and control for beams with arbitrary combinations of boundary conditions. They verified these techniques using shaped PVDF actuators and sensors[6,7]. Lee and Moon[8] and Lee *et al*[9,10] demonstrated modal damping in

beams using shaped PVDF transducers. Miller *et al*[11] reviewed the use of shaped PVDF sensors used to create desired spatial filtering properties for beams.

Clark & Fuller[12], Clark *et al*[13,14], and Clark & Burke[15] investigated shaped sensors for sensing acoustically significant modes in plates. However, these were also shapes which were designed to be good approximations to continuous one-dimensional shading. Even though these shaped transducers were applied to plates, their width was small in comparison with the smallest transverse wavelength present in the plate's dynamic response. However, errors in the placement of these sensors can lead to coupling with undesired modes in experimental implementations.[15]

The location and size of unshaded rectangular actuators have been studied by Dimitriadis *et al*[16] for structural acoustic control of plates. Shaping a distributed transducer into a nonrectangular shape is actually a form of two-dimensional shading: the gain is varied discontinuously over two-dimensions. Transducer shaping alone can provide useful modal coupling for plates. Burke and Hubbard[2] have extended the concept of continuous shading for beams to plates. Their work theoretically demonstrated that all-mode sensing and control could be achieved for plates through the use of continuous, two-dimensionally shaded transducers. While one-dimensional shading for beams and structural beam components can be easily approximated using shaped distributed transducers, the practical realization of two-dimensional shading in distributed transducers for plates is more difficult. A potential method outlined in this paper uses a superposition of gain-weighted, shaped transducers.

In this chapter, two-dimensional transducer shading and its implications for the active control of thin plates are discussed. Candidate methods of producing shaded transducers are also reviewed. Two-dimensional transducer shaping is presented as a useful design tool for the control problem. A method is described for approximating continuously shaded transducer distributions with a combination of transducer shaping and spatial gain-weighting. Wavenumber transforms are also used to evaluate controllability and observability. An optimization method used to fit the shaped transducer approximations to a continuous transducer distribution over a specified number of modal coefficients is then detailed. The analysis is applied to two specific examples. One utilizes two-dimensional transducer shaping and mode targeting alone to establish

controllability and observability over all but the even-even modes in a simply-supported plate. This transducer distribution is a very practical solution for the acoustic radiation attenuation problem. The second distribution is a superposition of gain-weighted, shaped transducer sections, which provide a good approximation to a continuous two-dimensionally shaded transducer distribution. This distribution provides "all-mode" controllability and observability over a large bandwidth and is therefore useful for global vibration suppression.

3.2 Analysis

3.2.1 Motivation for shading

To understand the utility of two-dimensional shaded transducers for plates, one must first examine the limits that uniformly-weighted distributed transducers place on controllability and observability for plates. The following discussion is a review of the plate control study by Burke and Hubbard.[2] Consider the transducer distribution, $\Lambda(x,y)$, laminated to a rectangular, simply-supported plate shown in Fig. 3.1. The transducer is assumed to be an induced-strain type such as piezopolymer film (PVDF) or a piezoceramic crystal (PZT). This distribution is even-symmetric about both centerlines, $x = a/2$ and $y = b/2$. If the material axes of this transducer are coincident with the axes of the plate, then the resultant control input/sensed output for the plate is shown in Fig. 3.2. Distributed doublet functions are obtained along the entire boundary. If the transducer were used as an actuator, these would correspond to uniform distributed bending moments. If the transducer were used as a sensor, it would be able to sense uniform angular displacement along the boundary.

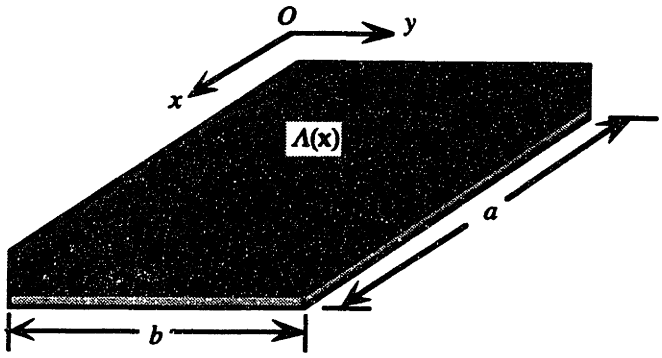

Fig. 3.1 Uniform transducer distribution.

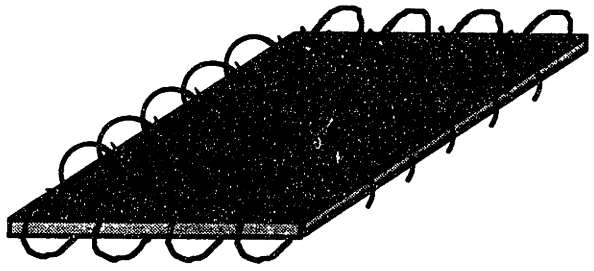

Fig. 3.2 Resultant control input/ sensed output for uniform transducer distribution.

The inherent even-even symmetry of the unshaded distribution limits the efficacy of this transducer when used as either a sensor or an actuator. Consider, the 2-1 mode and 2-2 modes of a simply-supported plate as shown in Fig. 3.3 and Fig. 3.4, respectively. Whenever the angular velocity distributions along opposing sides of the plate are equal, the unshaded transducer cannot do work or sense any motion in the direction normal to those sides. This occurs along sides $x = 0$ and $x = a$ in Fig. 3.3. Whenever the integrated angular velocity distributions along opposing sides of the plate are zero, the same result will hold. This is true for sides $y = 0$ and $y = b$ in Fig. 3.3 and for all sides in Fig. 3.4. Thus, this unshaded rectangular distribution will not be able to control or sense modes with odd-even, even-odd, or even-even symmetry. If this transducer were reduced in size but remained centered on the plate, it would still lack both controllability and observability for these modes.

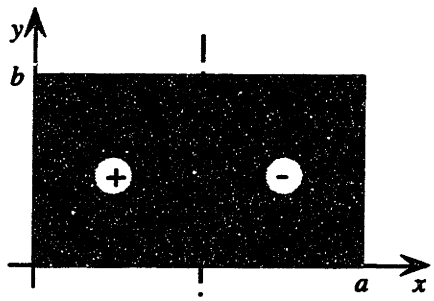

Fig. 3.3 2-1 mode of simply-supported plate.

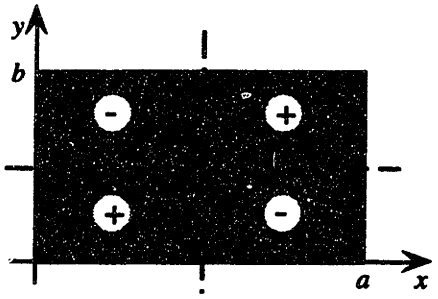

Fig. 3.4 2-2 mode of simply-supported plate.

By spatially varying the input/output characteristics of the transducer, i.e. by *shading* it, this symmetry problem can be resolved.[2] Shading the transducer in two dimensions gives it the different types of symmetry required to sense and control all modes of the simply supported plate. An example of a shaded transducer distribution is shown in Fig. 3.5. Note that the amplitude of the transducer distribution varies continuously over the surface of the plate. The transducer is shaded over two dimensions such that the gain is at a maximum, Λ_{max}, at one corner, $(x,y) = (0,0)$, but decreases linearly to zero in both the x and y directions. Thus, this transducer distribution has both even and odd symmetry about each of the center lines, $x = a/2$ and $y = b/2$.

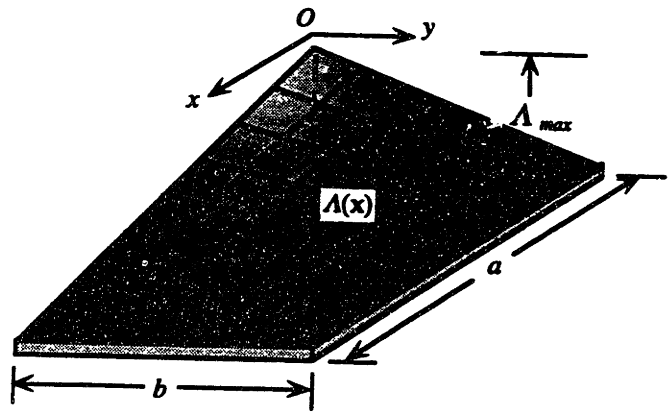

Fig. 3.5 Continuously shaded transducer distribution.

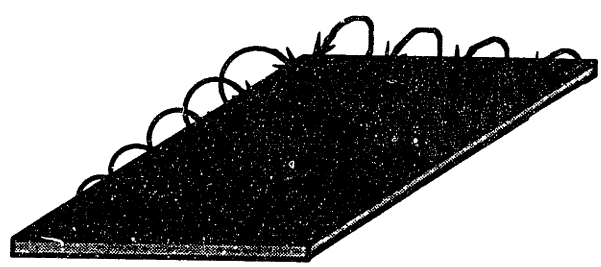

Fig. 3.6 Resultant control input/sensed output for continuously shaded transducer distribution.

The resultant control input/sensed output for the simply-supported plate is shown in Fig. 3.6. In contrast to the uniform transducer distribution, the induced moments/sensed angular velocity distributions are now only present on two adjacent sides of the plate, $x = 0$ and $y = 0$, and are weighted to decrease linearly from a maximum at the point (0,0) to zero at the points $(a,0)$ and $(0,b)$. This distribution can control and sense the modes that the uniform distribution could not. Because the moments occur only along $x = 0$ and $y = 0$, the cancellation due to equal angular velocity distributions along opposing sides of the plate is avoided. In addition, due to the weighting of the moments along each side, it is possible to sense modes where the integrated angular velocity along a side of the

plate is zero. Thus, all of the modes which could be present in a simply-supported plate can be controlled and sensed using the shaded distribution.

The above discussion used a simply-supported plate and a specific two-dimensional transducer shading as an example. However, two-dimensional shaded transducer distributions can be designed so as to exhibit all-mode sensing and control in plates with arbitrary boundary conditions.[2] When combined with a feedback controller such as velocity feedback, this is very beneficial for the problem of global vibration suppression in plates. To enhance stability robustness and increase performance, the shading can also be tailored so as to couple evenly into modes within a certain bandwidth and then roll-off for higher frequency modes. Thus, the system can be compensated spatially, through tailoring of the modal coefficients, to more effectively deal with temporal phase lag problems associated with real hardware such as analog filters and power supplies. That is the real benefit of shading: to be able to change the spatial filtering characteristics of an elastic system to improve both stability and performance.[4]

Another benefit of two-dimensional shading is in the design of transducers to control and sense only acoustically significant modes in panels. Sensing of acoustically significant modes in simply-supported plates has been studied previously using one-dimensionally shaded sensors,[12-15] but with two-dimensional shadings, the work can be expanded to develop both actuator and sensor distributions for plates with other boundary conditions. In these cases, the spatial filtering properties of plates can be changed so as to move energy from acoustically significant modes into those modes which are inefficient sound radiators.

3.2.2 Methods for shading two-dimensional piezoelectric transducers

The previous section reviewed the definition of two-dimensional shading and considered the benefits of shading from a physical standpoint. In the following discussion, the concepts will be formalized by examining the means for implementing shading using piezopolymer film (PVDF). This material is quite useful for producing two-dimensional shaded transducer distributions. It is tough and flexible, and can be laminated over large surface areas. The electrode

plating of the material can be manufactured with unique shapes, or the material can be cut to the desired shape.

The differential operator describing the spatial dynamics of piezopolymer film (PVDF), with the possibility of a skew angle, θ, between the transducer and structure axes, is given by Lee and Moon[1]

$$L[\Lambda(x,y)] = e_{31}^0 \frac{\partial^2 \Lambda(x,y)}{\partial^2 x} + e_{32}^0 \frac{\partial^2 \Lambda(x,y)}{\partial^2 y} + e_{36}^0 \frac{\partial^2 \Lambda(x,y)}{\partial x \, \partial y}, \tag{3.1}$$

$$\begin{bmatrix} e_{31}^0 \\ e_{32}^0 \\ e_{36}^0 \end{bmatrix} = \begin{bmatrix} \cos^2\theta & \sin^2\theta & -2\cos\theta\sin\theta \\ \sin^2\theta & \cos^2\theta & 2\cos\theta\sin\theta \\ \cos\theta\sin\theta & -\cos\theta\sin\theta & \cos^2\theta - \sin^2\theta \end{bmatrix} \times \begin{bmatrix} Y_p/(1-\nu_p^2) & \nu_p Y_p/(1-\nu_p^2) & 0 \\ \nu_p Y_p/(1-\nu_p^2) & Y_p/(1-\nu_p^2) & 0 \\ 0 & 0 & Y_p/2(1+\nu_p) \end{bmatrix} \begin{bmatrix} d_{3'1'}^0 \\ d_{3'2'}^0 \\ 0 \end{bmatrix}, \tag{3.2}$$

where $e_{31}^0, e_{32}^0, e_{36}^0$ represent the piezoelectric stress/charge constants with respect to the structure axes; $d_{3'1'}^0, d_{3'2'}^0$ are the piezoelectric strain/charge constants with respect to the PVDF material axes; and Y_p, ν_p are the Young's modulus and Poisson's ratio respectively of PVDF.

Both the actuator and sensor equations for PVDF laminated to a thin plate are based upon this differential operator. The skew angle, θ, can be varied to change the values of the stress/charge constants. These constants weight each partial differential term in the operator but cannot change the characteristics of the resultant terms of the operator. The characteristics of the resultant terms of the operator are affected only by the distribution function, $\Lambda(x,y)$, that is included under partial differentiation.

The spatial distribution of the transducer, $\Lambda(x,y)$, can be separated into two functions:

$$A(x,y) = F(x,y)\,P_0(x,y), \tag{3.3}$$

where $F(x,y)$ describes the shape of the PVDF and is defined as being equal to one within the transducer boundary and zero otherwise. $P_0(x,y)$ is the polarization profile of the PVDF and is assumed to be unity for film which has not been repolarized after manufacture.

One may vary the piezopolymer gain over two-dimensions by spatially varying either $A(x,y)$ or the electric field applied to the PVDF. It is possible to spatially weight the electric field used to pole the material during manufacture. This would affect the piezoelectric properties of the material, represented in the operator equation by the strain/charge constants. It is also possible to affect the polarization after manufacture by repoling (or depoling) the material with another strong electric field. Lee and Moon have accounted for this process with the $P_0(x,y)$ function which represents the polarization profile of the film. Hence, the material would arrive from the factory with certain values for the strain/charge constants which were constant over the extent of the film. The $P_0(x,y)$ would be equal to one for all (x,y). By applying a strong electric field to change the polarization profile, the overall effect in the operator would be to scale the piezoelectric properties of the film with respect to the factory values of the strain/charge constants.

Thickness variations in either the plate or the film can also cause shading. Thickness variation in film will change the applied electric field because the electric field is equal to the voltage applied to the film electrodes divided by the film thickness. Thickness variation in the bonding layer or in an added shim, will change the moment arm of the transducer relative to the center plane of the plate.

Another way to change the spatial distribution of the film, would be to change its electrode shape, $F(x,y)$. Nonrectangular shapes can be used to achieve desired shading effects in much the same way that shaped electrodes have been used for beam problems. However, shaping the film does not continuously change its gain over space. The film will have unit magnitude gain within the shape boundary and zero magnitude outside of the boundary.

During actual use, one can vary the electric field applied to the PVDF. One way to do this is to vary the voltage applied to the electrodes over space by gain-weighting transducer subsections. This technique combined with allowing transducer electrode shape to vary can be used to approximate a two-dimensional shading. Of the various techniques described in this section, transducer shaping and gain-weighting are the most practical for implementing two-dimensional shading. These techniques will be described in more detail in the next section and sample distributions will be presented which possess useful spatial filtering properties.

3.2.3 Mathematical modeling: calculation of modal coefficients for plates

To evaluate possible methods of shading the distribution of PVDF film, one can study the resultant effects of shading on modes of vibration in plates. Consider the free response of a Bernoulli-Euler plate. The response can be expressed as a sum of orthogonal modes separable in space and time:

$$w_n(t,\mathbf{x}) = \sum_{n=1}^{\infty} w_n(t)\, \varphi_n(\mathbf{x}), \tag{3.4}$$

where $w_n(t)$ is a harmonic function of time with natural frequency, w_n and φ_n is the modal shape.

The nth actuator modal expansion coefficient for the transducer, b_n, shows how the transducer, when used as an actuator, couples into individual modes of vibration. Conversely, the sensor modal coefficient, c_n, shows how well the transducer, when used as a sensor, senses individual modes. The modal coefficients characterize the impact of shading on plates and can serve as a measure for shading approximations. Burke and Hubbard[2] used Lyapunov functionals to assess the impact of shading on controllability and observability for plates, but similar results can be derived by examination of the modal coefficients. The use of modal coefficients is better suited for the study of complex two-dimensional transducer distributions because information about the plate modal symmetry is taken into account in their calculation. The nth modal coefficient for a two-dimensional transducer applied to a plate of domain, D, is given by[2,17]

$$b_n = c_n = \int_D \varphi_n(\mathbf{x})\, L[\Lambda(\mathbf{x})]\, d\mathbf{x}. \tag{3.5}$$

Note that the value of this modal coefficient depends upon the plate mode shape $\varphi_n(\mathbf{x})$, the transducer spatial distribution $\Lambda(x,y)$, and the differential operator describing the transducer's spatial dynamics, $L[.]$. For illustrative purposes, assume that the plate under consideration is simply-supported along all sides. This allows the mode shapes to be separated into one-dimensional sinusoids in x and y,

$$\varphi_n(\mathbf{x}) = \varphi_r(x)\,\varphi_q(y) = A_{rq}\sin(r\pi x/a)\sin(q\pi y/b). \tag{3.6}$$

These mode shapes will be used in the following analysis to calculate modal coefficients for a variety of transducer spatial distributions.

In the previous chapter, arbitrary two-dimensional transducer distributions were modeled using two-dimensional generalized functions with composite functions included in the arguments. The theory needed to calculate the PVDF differential operator acting on these distributions was also developed. The arbitrary transducer shape shown in Fig. 3.7 can be represented concisely by

$$\Lambda(x,y) = \left(\langle x - x_2\rangle^0 - \langle x - x_1\rangle^0\right)\left(\langle y - f_2(x)\rangle^0 - \langle y - f_1(x)\rangle^0\right). \tag{3.7}$$

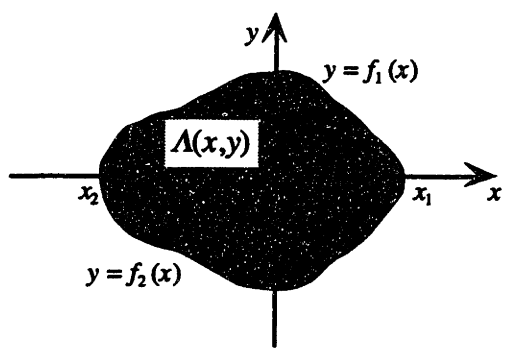

Fig. 3.7 Arbitrary transducer shape in rectangular coordinates.

The partial differentials needed to calculate the PVDF differential operator acting on the distribution are given by,

$$\frac{\partial \Lambda(x,y)}{\partial x} = \left(\langle x-x_2\rangle^{-1} - \langle x-x_1\rangle^{-1}\right)\left(\langle y-f_2(x)\rangle^{0} - \langle y-f_1(x)\rangle^{0}\right)$$
$$+\left(\langle x-x_2\rangle^{0} - \langle x-x_1\rangle^{0}\right)\left(-f_2'(x)\langle y-f_2(x)\rangle^{-1} + f_1'(x)\langle y-f_1(x)\rangle^{-1}\right), \quad (3.8)$$

$$\frac{\partial \Lambda(x,y)}{\partial y} = \left(\langle x-x_2\rangle^{0} - \langle x-x_1\rangle^{0}\right)\left(\langle y-f_2(x)\rangle^{-1} - \langle y-f_1(x)\rangle^{-1}\right). \quad (3.9)$$

Equations (3.7) - (3.9) allow for concise modeling of the transducer distribution and the piezoelectric differential operator. The second derivatives are given in Chapter 2, equations (2.35) - (2.37). The use of generalized functions for the mathematical representation of the distribution and the operator allows the modal coefficients to be calculated analytically. These tools will be used in the following section to examine the effects of transducer shading.

3.3 Two-Dimensional Transducer Design

3.3.1 Continuous, linearly-weighted distribution

Using the mathematics developed in the preceeding section, it is possible to analytically represent transducer distributions and to calculate their modal coefficients when applied to thin plates. Referring to the two-dimensional shaded distribution described in section 3.2.1 and pictured in Fig. 3.5, the spatial distribution for this continuous, linearly-weighted shading can be represented by

$$\Lambda(x,y) = \left(\langle x\rangle^{0} - \frac{1}{a}\langle x\rangle^{1} + \frac{1}{a}\langle x-a\rangle^{1}\right)\left(\langle y\rangle^{0} - \frac{1}{b}\langle y\rangle^{1} + \frac{1}{b}\langle y-b\rangle^{1}\right). \quad (3.10)$$

The linear weighting in two dimensions is described by the "ramp" generalized functions. The differential operator result for this distribution is given by,

$$L[\Lambda(x,y)] = e_{31}^{0}\left(\langle x\rangle^{-2} - \frac{1}{a}\langle x\rangle^{-1} + \frac{1}{a}\langle x-a\rangle^{-1}\right)\left(\langle y\rangle^{0} - \frac{1}{b}\langle y\rangle^{1} + \frac{1}{b}\langle y-b\rangle^{1}\right)$$
$$e_{32}^{0}\left(\langle x\rangle^{0} - \frac{1}{a}\langle x\rangle^{1} + \frac{1}{a}\langle x-a\rangle^{1}\right)\left(\langle y\rangle^{-2} - \frac{1}{b}\langle y\rangle^{-1} + \frac{1}{b}\langle y-b\rangle^{-1}\right). \quad (3.11)$$

This result includes weighted delta functions along the boundaries. For a simply-supported plate, these will vanish due to the pinned boundary conditions. Thus, the result given in equation (3.11) can be simplified by dropping these terms and pulling out the linear weighting from the generalized functions to yield,

$$L[\Lambda(x,y)] = e_{31}^{0}\left(1-\frac{y}{b}\right)\langle x\rangle^{-2}\left(\langle y\rangle^{0}-\langle y-b\rangle^{0}\right) + e_{32}^{0}\left(1-\frac{x}{a}\right)\langle y\rangle^{-2}\left(\langle x\rangle^{0}-\langle x-a\rangle^{0}\right). \quad (3.12)$$

This equation includes the linearly-weighted doublet functions along the sides $x = 0$ and $y = 0$, shown in Fig. 3.6. The nth modal coefficient is calculated by substituting equations (3.6) and (3.12) into (3.5) and integrating in x and y to give

$$b_n = e_{31}^{0}(r/q)(b/a) + e_{32}^{0}(q/r)(a/b). \quad (3.13)$$

The integration of the transducer distribution with the modal shape results in the weighted slope of the modal shape being sifted out along the two sides and then integrated over the length of the sides. As can be seen from equation (3.13), the modal coefficient derived for this shaded transducer will be nonzero for all r and q. Thus, both controllability and observability are guaranteed whether the transducer is used as an actuator or a sensor.

This shading would prove useful for controlling vibrations in simply-supported plates because of its all-mode actuation and sensing properties. Unfortunately, it is difficult to effect this shading directly. The methods described in section 3.2.2 are very difficult to manufacture. One method, however, that *can* be implemented is an approximation of the shading using a sum of gain-weighted transducer sections. Trying to approximate a two-dimensional shading such as that shown in Fig. 3.5 using a two-dimensional array of rectangular sections would be difficult because of the large number that would needed. The number of transducer sections needed to provide a good approximation could be reduced if the transducer shape was used to aid in the approximation.

3.3.2 Transducer shaping: triangular distribution

Triangular-shaped transducers can be used to capture part of the linear ramp function present in the continuous shading. As a first step at approximating the continuous, linearly-weighted transducer distribution shown in Fig. 3.5, consider the triangular distribution shown in Fig. 3.8.

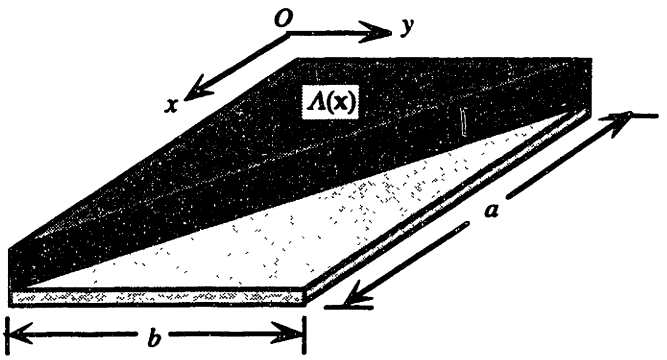

Fig. 3.8 Triangular transducer distribution.

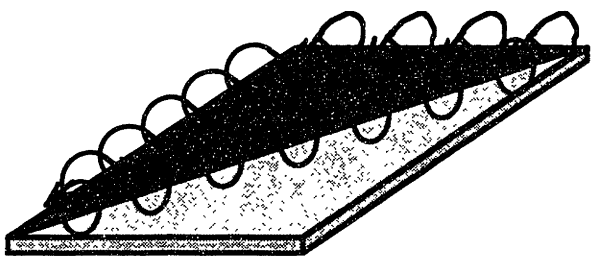

Fig. 3.9 Resultant control input/sensed output for triangular transducer distribution.

This distribution, like the linearly-weighted shading, is at a maximum at the origin and decreases to zero along both x and y through the decrease of surface area covered by the transducer. Using two-dimensional distributions with composite functions in the arguments, the transducer distribution is represented by

$$\Lambda(x,y) = \left(\langle x\rangle^0 - \langle x-a\rangle^0\right)\left(\langle y\rangle^0 - \left\langle y+\tfrac{b}{a}x-b\right\rangle^0\right). \tag{3.14}$$

The differential operator result is given by

$$L[\Lambda(x,y)] = e_{31}^0\left(\langle x\rangle^{-2} - \langle x-a\rangle^{-2}\right)\left(\langle y\rangle^0 - \left\langle y+\frac{b}{a}x-b\right\rangle^0\right)$$
$$+\left(\langle x\rangle^0 - \langle x-a\rangle^0\right)\left[e_{32}^0\langle y\rangle^{-2} - \left(\frac{b^2}{a^2}e_{31}^0 + e_{32}^0\right)\left\langle y+\frac{b}{a}x-b\right\rangle^{-2}\right]$$
$$-2\frac{b}{a}e_{31}^0\left(\langle x\rangle^{-1} - \langle x-a\rangle^{-1}\right)\left(\left\langle y+\frac{b}{a}x-b\right\rangle^{-1}\right), \tag{3.15}$$

and is shown in Fig. 3.9. Because the weighting is uniform within the shape boundary, the operator results in uniform doublet functions along the transducer boundary. Delta functions were also obtained at the vertices, but these were eliminated due to the simply-supported boundary conditions for the plate under consideration. The modal coefficients that arise from this distribution will be the sum of line integrals of the modal slope along boundaries $x = 0$, $y = 0$ and along the hypotenuse of the triangle. The modal coefficients that result from the application of this distribution to a simply-supported plate are given by,

$$b_n = e_{31}^0(r/q)(b/a)[(-1)^q - 1] + e_{32}^0(q/r)(a/b)[(-1)^r - 1]$$
$$+ \frac{q\pi}{b}\left(\frac{b^2}{a^2}e_{31}^0 + e_{32}^0\right)(-1)^q\int_0^a \sin(r\pi x/a)\cos(q\pi x/a)\,dx. \tag{3.16}$$

The first two terms show the result of the doublet functions acting along sides $x = 0$ and $y = 0$. Along $x = 0$, whenever q is even, the line integral along this side is zero. Along $y = 0$, whenever r is even, the line integral along this side is zero. The result of the doublet functions acting along the hypotenuse is shown in the last term of equation (16). The calculation of this integral depends upon whether $r = q$:

$$\int_0^a \sin(r\pi x/a)\cos(q\pi x/a)\,dx = 0, \quad (r = q); \tag{3.17}$$

$$\int_0^a \sin(r\pi x/a)\cos(q\pi x/a)\,dx =$$
$$-\frac{a}{2\pi}\left\{\frac{1}{r-q}[(-1)^{r-q} - 1] + \frac{1}{r+q}[(-1)^{r+q} - 1]\right\}, \quad (r \neq q). \tag{3.18}$$

Whenever $r = q$, the line integral along the hypotenuse will be zero. When $r = q$ = even, as in Fig. 3.10, the line integrals along $x = 0$ and $y = 0$ are also zero so the

modal coefficient sums to zero. However, when $r = q$ = odd, as shown in Fig. 3.11, the line integrals along x =0 and y =0 are both nonzero so the modal coefficient for this case is nonzero. The reason for the zero line integral along the hypotenuse, however, can be seen by examining both Figs. 3.10 and 3.11 and noting that each + or - rectangular section acts like a smaller plate in the 1-1 mode. Whenever the transducer hypotenuse extends from one corner of the + or - section to another, the line integral along this section will be zero. The distribution sifts out the slope of the mode shape along the hypotenuse and legs of the triangle. The contribution of the hypotenuse to the modal coefficient will be zero whenever the slope along the hypotenuse integrates to zero over the length of the plate.

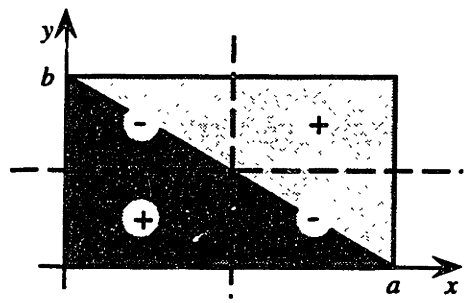

Fig. 3.10 Triangular distribution shown with 2-2 mode.

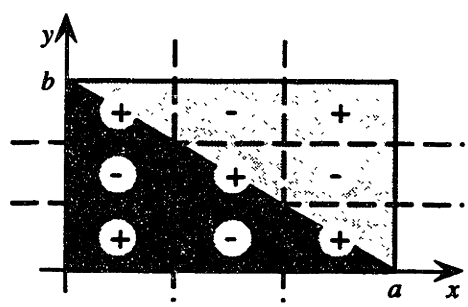

Fig. 3.11 Triangular distribution shown with 3-3 mode.

For r and q not equal and both odd, the line integrals along all sides wil be nonzero. For r and q not equal and either r or q is even, as shown in Fig. 3.12, the line integral along one of the sides of the plate will be zero but the integral along the hypotenuse will be nonzero. For r and q not equal, but both even, all of the line integrals, and hence the modal coefficient, will be zero. This can be seen in

Fig 3.13. The reason for the zero line integral along the hypotenuse in this case is due to the way the hypotenuse cuts through the sections between the nodal lines. The line integrals from the two - sections intersected by the hypotenuse sum to zero as do the line integrals from the two + sections that are intersected.

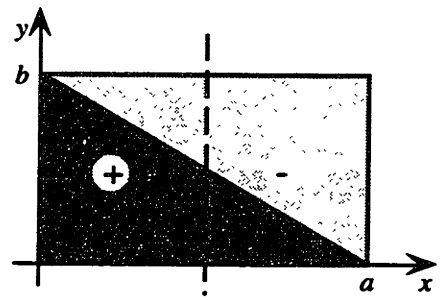

Fig. 3.12 Triangular distribution shown with 2-1 mode.

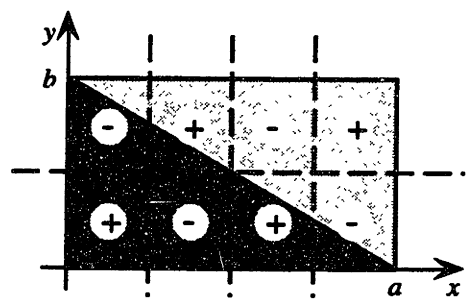

Fig. 3.13 Triangular distribution shown with 4-2 mode.

This shaped transducer distribution can control or sense the odd-odd, odd-even, and even-odd modes of a simply supported plate. It cannot, however, control or sense any of the even-even modes of a simply-supported plate. This makes the distribution very useful for the acoustic radiation attenuation problem because the odd-odd modes are the most efficient acoustic radiators while the odd-even and even-odd modes radiate sound to a lesser extent, and the even-even modes do not contribute significantly to the radiated sound field.[12] This transducer can be used to form a colocated sensor/actuator pair which will only sense and do work on those modes which have a significant contribution to the radiated sound field.

3.3.3 Gain-weighted approximation to linearly-weighted shading

If global vibration suppression of a simply supported plate is desired, the triangular distribution will not suffice. The above analysis shows that using shape to approximate shading in two-dimensions is more difficult than using it to approximate shading for beams. The two-dimensional linear shading is necessary to provide global controllability and observability. It is possible to approximate this shading for a large number of modes using an array of gain-weighted, shaped transducers as shown in Fig. 3.14. This distribution is a sum of smaller distributions which are each gain-weighted. The distribution linearly decreases in the x-direction due to the triangular shaping and decreases by steps in the y-direction because of the gain-weighting.

The differential operator result of this distribution is shown in Fig. 3.15. Doublet functions are obtained along the boundaries of the transducer sections but their magnitudes vary from section to section depending upon the gain that is given to each section. In the figure, for clarity, the doublet functions along the sides are represented by a resultant doublet function acting on the middle of the side.

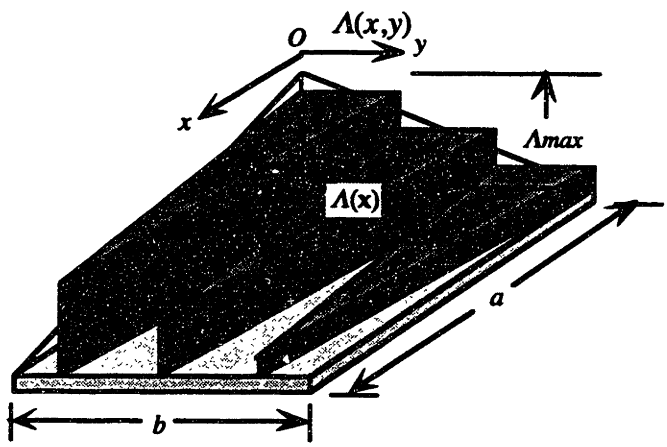

Fig. 3.14 Approximation to 2D linear shading.

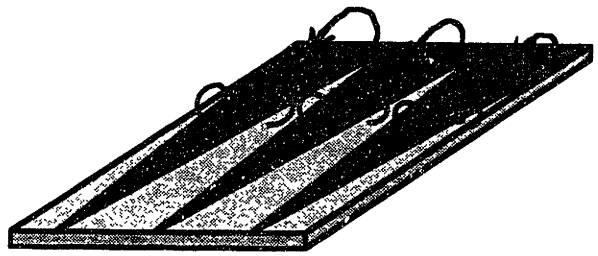

Fig. 3.15 Resultant control input/sensed output of linear 2D shading approximation.

The modal coefficients for the linearly-weighted shading are given by equation (3.13). To determine the best approximation, the modal coefficients of the gain-weighted array of transducer sections can be calculated and compared to those of the linearly-weighted shading.

The transducer distribution, $\Lambda(\mathbf{x})$, of a gain weighted array is a sum of the individual transducer distributions of the sections (with gains of the sections included in each distribution):

$$\Lambda(\mathbf{x}) = \sum_{s=1}^{S} \Lambda_s(\mathbf{x}), \tag{3.19}$$

where S is the total number of sections used in the approximation. The nth modal coefficient for the transducer distribution is given by the sum of the nth modal coefficients calculated for each section,

$$b_n = \sum_{s=1}^{S} \int_D \varphi_n(\mathbf{x})\, L\left[\Lambda_s(\mathbf{x})\right] d\mathbf{x} = \sum_{s=1}^{S} b_{n,s}. \tag{3.20}$$

The geometry of a triangular section to be used in the array is shown in Fig. 3.16.

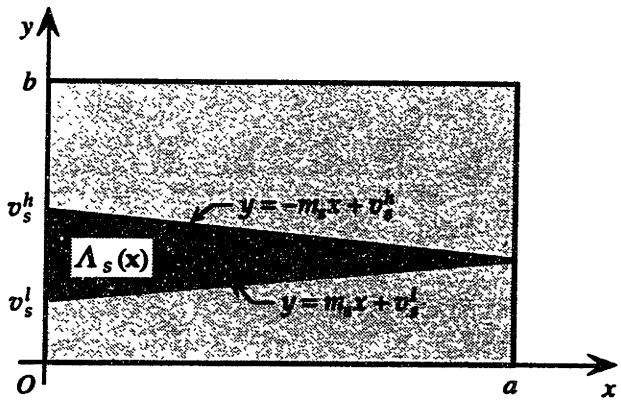

Fig. 3.16 Triangular transducer section geometry.

Each section is an isosceles triangle with a length equal to the total length of the plate, a. The section's spatial distribution is given by,

$$\Lambda_s(x,y) = g_s\left(\langle x\rangle^0 - \langle x-a\rangle^0\right)\left(\langle y - m_s x - v_s^l\rangle^0 - \langle y + m_s x - v_s^h\rangle^0\right), \tag{3.21}$$

where g(s) is the gain assigned to the section,

$$g_s = -\frac{(v_s^l + v_s^h)}{2}\left(\frac{\Lambda_{max}}{b}\right) + \Lambda_{max}. \tag{3.22}$$

This section gain is chosen such that the midpoint of the transducer section intersects a line defining the ideal gain over the plate width as shown in Fig. 3.17.

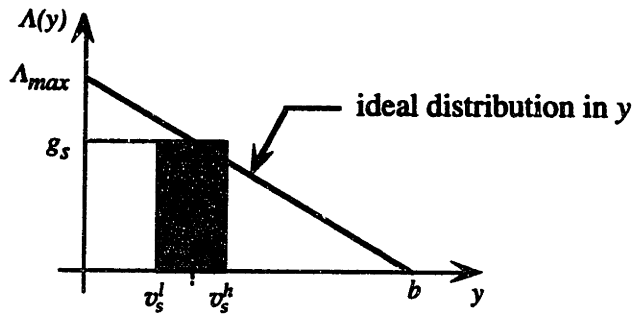

Fig. 3.17 Transducer section gain weighting.

Again, the differential operator acting on this distribution will produce doublet functions lining the boundary,

$$\begin{aligned} L[\Lambda(x,y)] = {} & e_{31}^0\left(\langle x\rangle^{-2} - \langle x-a\rangle^{-2}\right)\left(\langle y - m_s x - v_s^l\rangle^0 - \langle y + m_s x - v_s^h\rangle^0\right) \\ & + \left(m_s^2 e_{31}^0 + e_{32}^0\right)\left(\langle x\rangle^0 - \langle x-a\rangle^0\right)\left(\langle y - m_s x - v_s^l\rangle^{-2} - \langle y + m_s x - v_s^h\rangle^{-2}\right) \\ & - 2m_s e_{31}^0\left(\langle x\rangle^{-1} - \langle x-a\rangle^{-1}\right)\left(\langle y - m_s x - v_s^l\rangle^{-1} + \langle y + m_s x - v_s^h\rangle^{-1}\right). \end{aligned} \quad (3.23)$$

Their magnitude is uniform along each side because the gain of the section is constant over its spatial extent. Delta functions are also obtained at the vertices, but these disappear due to the pinned boundary conditions.

The modal coefficient for this section is

$$\begin{aligned} b_{n,s} = {} & g_s\left[\cos\left(\frac{q\pi v_s^h}{b}\right) - \cos\left(\frac{q\pi v_s^l}{b}\right)\right] \times \\ & \left\{e_{31}^0 (r/q)(b/a) + \tfrac{1}{2}\left(m_s^2 e_{31}^0 + e_{32}^0\right)\left(\frac{q\pi}{b}\right)\left[\left(\frac{r\pi}{a} + \frac{q\pi m_s}{b}\right)^{-1} + \left(\frac{r\pi}{a} - \frac{q\pi m_s}{b}\right)^{-1}\right]\right\}. \end{aligned} \quad (3.24)$$

As can be seen from the above expression and from Fig. 3.18, cancellation occurs when a nodal line in x bisects the triangle. So, when different transducer sections of equal widths are added together, even with different gains, as shown in Fig. 3.19, cancellation occurs when $q = 2S$ for all r. Because of this cancellation, one must employ unequal segment widths to change the inherent symmetry.

As an aside, the last term in equation (3.24) appears to go to infinity when $m_S = b/2Sa$ and $q = 2Sr$. The slope condition occurs whenever the sections have equal widths or whenever there is only one section. This can be seen from Fig 3.18. In this case, $m_S = b/2a$ and this term appears to go to infinity. However, using L'Hospital's Rule, it can be shown that, when $q = 2Sr$ and the slope aproaches $b/2Sa$, this term is well-behaved and goes to zero.

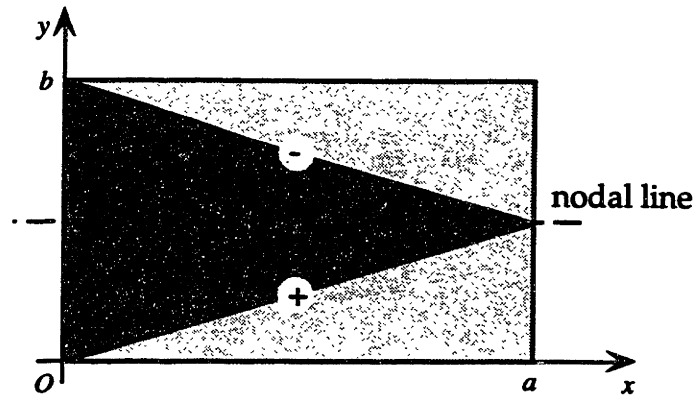

Fig. 3.18 Transducer section shown with 1-2 mode.

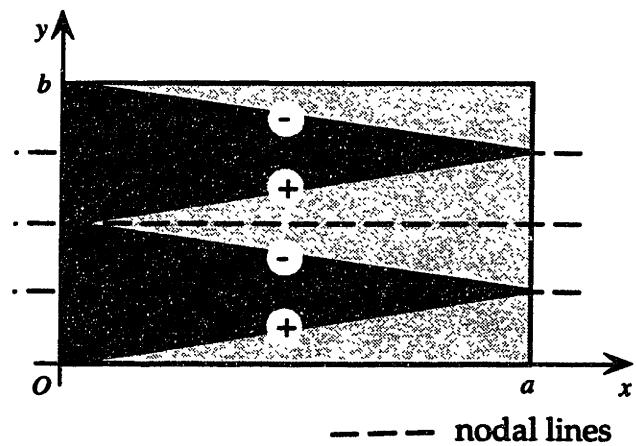

Fig. 3.19 Equal width transducer sections shown with 1-4 mode.

The benefit of using unequal widths in the approximation becomes apparent when the spatial Fourier transform is applied to the problem. It is possible to separate the problem into x and y components because of the plate's simply-supported boundary conditions. Examination of the y component will help determine the controllability/observability characteristics of the transducer distribution because the step approximation occurs along this direction. Imagine taking a slice of the transducer distribution along the line $x = 0$. The transducer distribution will look like a staircase function in this case. We will be comparing this function to that shown as the ideal function, the gain of the linear 2D distribution, shown in Fig. 3.17. Using this transform method involves less analysis than calculating the modal coefficients for each transducer distribution

as a whole. Thus, it provides a useful tool for evaluation of the controllability/observability properties of candidate distributions. The Fourier transform of the PVDF operator acting on the y component of a transducer distribution, $L[\Lambda(y)]$ is given by,

$$h(k) = \frac{1}{\sqrt{2\pi}} \int_0^b L[\Lambda(y)] e^{iky} dy \tag{3.25}$$

where the limits of integration are reduced from $(-\infty, +\infty)$ to $[0, b]$ because the transducer distribution is bounded by the width of the plate, b.. The spatial variable k is the wavenumber component in the y direction.

The magnitude of the imaginary part of the transform is given by,

$$h_{imag}(k) = \left| \int_0^b L[\Lambda(y)] \sin(ky) dy \right|. \tag{3.26}$$

This is equivalent to the expression for the y component of the nth modal coefficient when $k = q\pi/b$. Examination of this part of the transform is relevant to assessing the impact of the distribution on the plate mode shapes. Simply looking at the entire Fourier transform would not be useful because plate modal information would not be taken into account. Since the imaginary part of the transform is a continuous version over k of the y-component of the modal coefficient equation, the information obtained can be used to determine controllability and observability characteristics of the transducer acting on the simply-supported plate.

First, consider the ideal distribution in y shown in Fig. 3.17. This distribution can be represented by,

$$\Lambda(y) = \langle y \rangle^0 - \frac{1}{b}[\langle y \rangle^1 - \langle y - b \rangle^1]. \tag{3.27}$$

The PVDF operator acting on this distribution is given by,

$$L[\Lambda(y)] = \langle y \rangle^{-2}. \tag{3.28}$$

The point forces have been eliminated due to the boundary conditions leaving only a positive moment at $y = 0$. The Fourier transform for this case is,

$$h(k) = -ik. \tag{3.29}$$

Since the transform is purely imaginary, the magnitude of the imaginary component is simply k and is thus nonzero for all k. Thus, this ideal distribution has all-mode controllability and observability.

Now consider the case of an individual transducer section used in an approximation of the ideal distribution. The y component of the transducer distribution given in equation (3.21) along the line $x = 0$ is given by,

$$\Lambda_s(y) = g_s\left(\langle y - v_s^l\rangle^0 - \langle y - v_s^h\rangle^0\right). \tag{3.30}$$

The PVDF operator acting on this individual section distribution is,

$$L[\Lambda_s(y)] = g_s\left(\langle y - v_s^l\rangle^{-2} - \langle y - v_s^h\rangle^{-2}\right). \tag{3.31}$$

This result shows doublet functions (or moments) acting in opposition at the ends of the section. The Fourier transform of (3.31) is,

$$h(k) = -ikg_s\left(e^{ikv_s^l} - e^{ikv_s^h}\right). \tag{3.32}$$

The magnitude of the imaginary component is,

$$h_{imag}(k) = \left|kg_s\left[\cos\left(kv_s^l\right) - \cos\left(kv_s^h\right)\right]\right|. \tag{3.33}$$

From this equation, it is evident that whenever a nodal point occurs at the midpoint of the transducer section, no matter how large or small the section, a zero result will be obtained for the imaginary component of the Fourier transform. The opposing doublet moments produced by the transducer distribution will not be able to do any work or sense any angular displacement because of the symmetry involved. Thus, the particular mode for which this occurs will not be controllable or observable.

The following plots illustrate this point and also demonstrate the benefit of using sections with unequal widths. The first two plots, shown in Fig. 3.20, show an approximation to the ideal distribution using only two sections of equal width

and the imaginary part of the Fourier transform of such a distribution. The even modes, occuring at $k = 2\pi/b, 4\pi/b, 6\pi/b, \ldots$, are marked with an x on the wavenumber transform plot. The transform of the ideal distribution is shown with a dotted line while the transform of the approximation is shown with a a solid line. The zeros of the approximation occur at every other even mode beginning with $k = 4\pi/b$. Thus, this approximation to the ideal distribution can control/observe the first three modes of the plate, k = π/b, $2\pi/b$, and $3\pi/b$ before reaching a zero for the fourth mode. The mode shapes of the second and fourth mode are shown in the top plot. Since the transducer sections have different gains, the second mode is controllable. However, the fourth mode is not controllable because its has nodal points which occur in the middle of each transducer section.

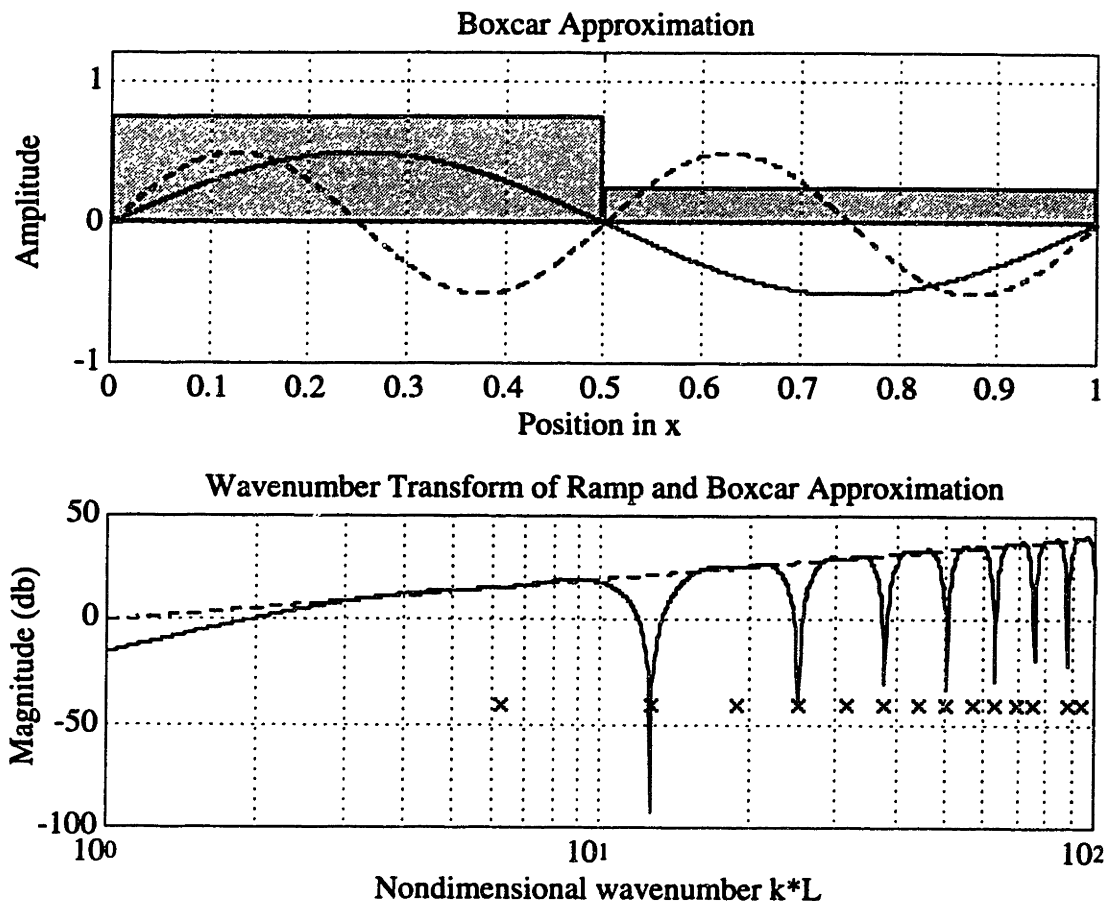

Fig. 3.20 Equal width section approximation and wavenumber sine transform.

The next two plots, pictured in Fig. 3.21, show that the same results are obtained when the width of the sections is reduced, but the midpoints are kept at the same location. In this case, the widths were reduced by the same amount, but the result would be the same even if they were of unequal width. Since the midpoints of each section are the same, they will still lack the asymmetry needed to control or observe the fourth mode.

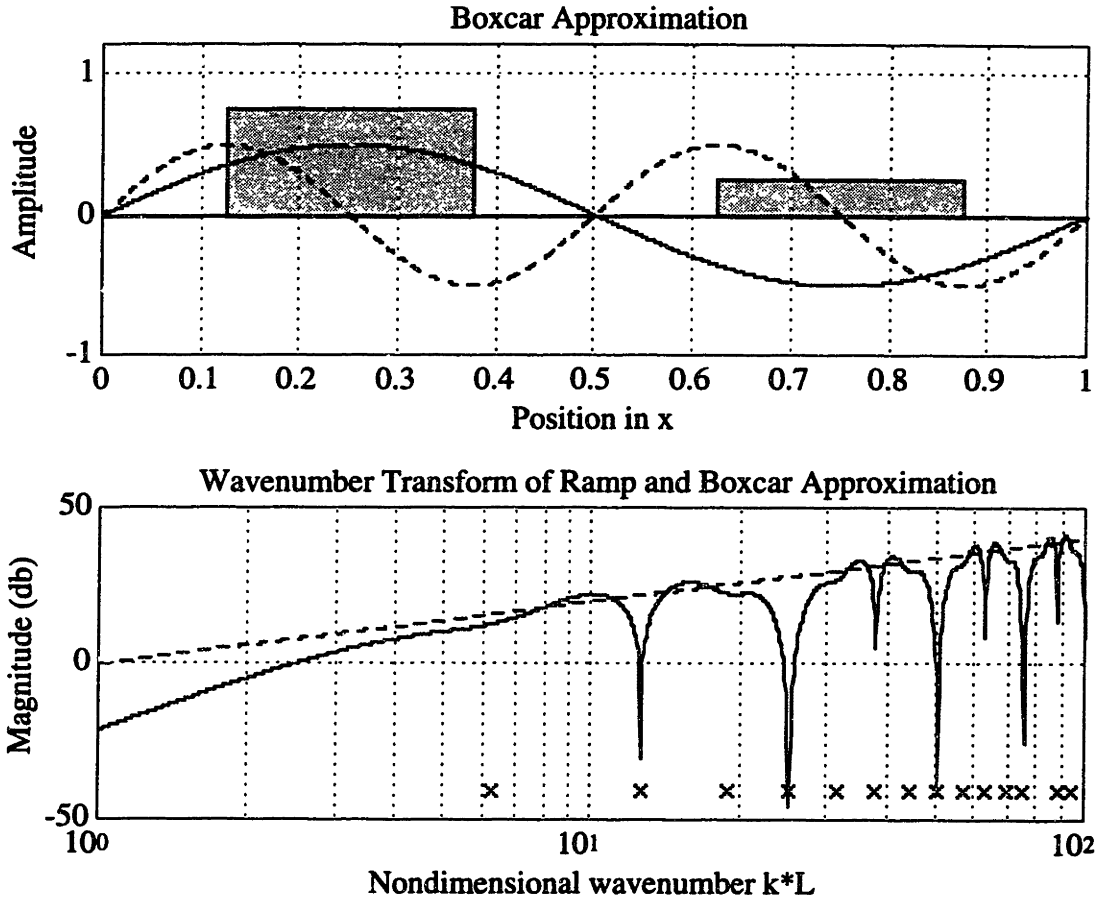

Fig. 3.21 Section approximation, with reduced widths, and wavenumber sine transform.

The final plots in Fig. 3.22 demonstrate improved controllability /observability characteristics using transducer sections with different widths and midpoints located in different points. The result is that the first five modes are now controllable/observable using only two transducer sections. On the transducer section plot, the solid line shows the mode shape of the fourth mode and the dashed line shows the mode shape of the sixth mode. It is not until the

sixth mode, k = $6\pi/b$, that nodal points will occur at the midpoints of the transducer sections.

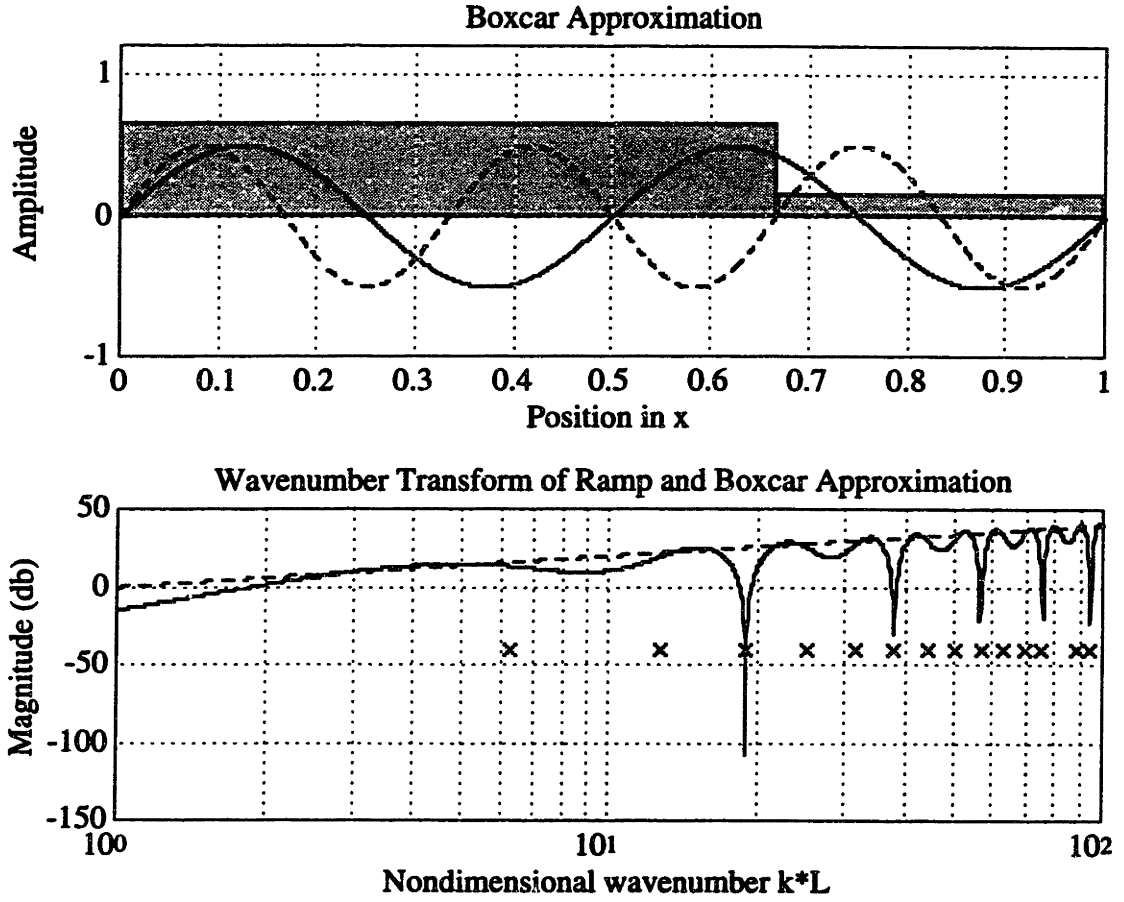

Fig. 3.22 Section approximation, with unequal widths, and wavenumber sine transform.

The wavenumber transform analysis demonstrates that one can allow the section widths to be degrees of freedom in an optimization problem that seeks to minimize the difference between the ideal distribution and the approximation. The analytical method is also a useful tool for understanding the physics of the transducer distribution's interaction with the plate mode shapes.

The design process can be reduced to a minimization problem with the following quadratic objective function:

$$J = \sum_{n=1}^{N} \left(b_{n,\,ideal} - b_{n,\,approx}(\alpha)\right)^2 = \left| b_{ideal} - b_{approx}(\alpha) \right|^2, \qquad (3.34)$$

where the $\mathbf{b}_{ideal}$ vector corresponds to the continuous, linearly-weighted shading and the $\mathbf{b}_{approx}$ vector corresponds to the gain-weighted approximation. The vector α is composed of the section widths α_S of the first S - 1 sections. These are the independent variables in the minimization problem. The width of the last section is a dependent variable because it is equivalent to the difference between the width of the plate, b, and the sum of the first S - 1 sections. The number of sections, S, and the number of modes, N, used in the optimization problem are both parameters to be determined prior to minimization.

The number of sections is dependent upon the width of the plate, b, because too large a number for a given plate width would yield section widths too small to be easily fabricated or positioned on the plate. The number of modes, N, used in the optimization problem should be large enough to include all modes within the control bandwidth. As N becomes very large, however, it will become more difficult to obtain a good approximation because more degrees of freedom are needed for the optimization. An important consideration becomes the values of the modal coefficients outside the desired bandwidth. This is because, in a real system, noise and phase lags can cause instability in high frequency modes with strong modal coupling. When a global controller such as velocity feedback is used, these modes can be destabilized. Thus, it is important to perform the optimization over a certain number of modes N and then check the values of the modal coefficients for the higher order modes.

All of the constraints for the problem relate to the geometry. The sections are chosen to be isosceles triangles with length equal to the length of the plate. Each width must be larger than a certain minimum width, α_{min} , and this width must be greater than zero. All sections must touch on the $x = 0$ side of the plate. Also, the total width of the sections cannot exceed the width of the plate.

The objective function was written as a MATLAB function to be minimized by the "fmins" function included in the MATLAB toolbox. This function uses an unconstrained nonlinear optimization scheme to find the minimum of a function of several variables. Most of the geometric constraints for this problem were written into the definition of the objective function. Two constraints could not be

included in this way: the minimum width constraint and the total width maximum. They were included by heavily penalizing the objective function when they were violated.

This research was concerned with matching an implementable distribution with an ideal distribution that had known controllability and observability properties. However, the analysis and optimization techniques can be applied to a more general case. One may define a modal coefficient profile that has a desired shape in the wavenumber domain. For example, if one is using a global controller such as velocity feedback, a desired profile would include roll-off after a defined bandwidth. In this manner, the transducer would not couple strongly into those modes for which the phase lags in the system summed to greater than 90 degrees, thus facilitating a higher velocity feedback gain. This would allow spatial compensation using distributed transducers to compensate for temporal phase lags in a hardware implementation.

The ideal distribution would then be defined by the desired modal coefficient profile, $\mathbf{b}_{ideal}$, and the optimization process would attempt to match some unknown transducer distribution to this profile. Since the geometry of the ideal distribution would be unknown, the geometry of the approximation could be changed to allow more degrees of freedom. For example, the plate could be divided up into a grid with a rectangular transducer section assumed to be covering each grid section. The gain of each transducer section would be allowed to vary between a minimum and maximum value. The gains of each section would then become the degrees of freedom used in the optimization problem. The optimization process would then be exercised and the results examined to see if an inherent geometry and symmetry exists. Then, suitable transducer shapes and gain-weighting could be applied to the problem so that the number of transducer sections could be reduced. The optimization process could take place again using a reduced number of degrees of freedom. In this manner, it would be possible to achieve a desired modal coefficient profile using a finite number of shaped, gain-weighted transducers.

3.4 Design example

The design process for the approximation outlined in section 3.3.3 was applied to a sample plate with length a = 0.671 m, b = 0.469 m. Uniaxial PVDF film was used, with $d^0_{3'1'} = 23\text{x}10^{-12}$ C/N and $d^0_{3'2'} = 3\text{x}10^{-12}$ C/N, $Y_p = 2\text{x}10^9$ N/m^2, and $v_p = 1/3$. The number of modes chosen to optimize over was 10 and the number of sections chosen was 5. The initial estimate for α was chosen such that all of the section widths were equal. The minimum width was 5cm.

The minimization routine converged and the result was checked by starting from several different initial estimates for the width vector. This was done to see if the minimum obtained was local or "global" for the allowable range of widths. The resulting widths are α = [8.2 6.4 11.0 10.4] cm. The resulting modal coefficients are compared to the linearly-weighted ideal shading in Fig. 3.23. The modal coefficients have been normalized such that the largest has unit amplitude. The modal coefficients obtained for N < 10 were in excellent agreement with those obtained for the linearly-weighted shading. The percentage error is less than 1% for those modes with n < 10. However, even for those modes just outside of the control bandwidth, the percentage error is less than 10%. It is interesting to note that the error was greatest for modes 13 and 15. For the given plate, these mode numbers correspond to the 1-4 and 2-4 modes. These are the only two modes shown for which q = 4. The errors associated with these modes are large because they are the most difficult to match due to the discrete gain-weighting approximation in the y direction.

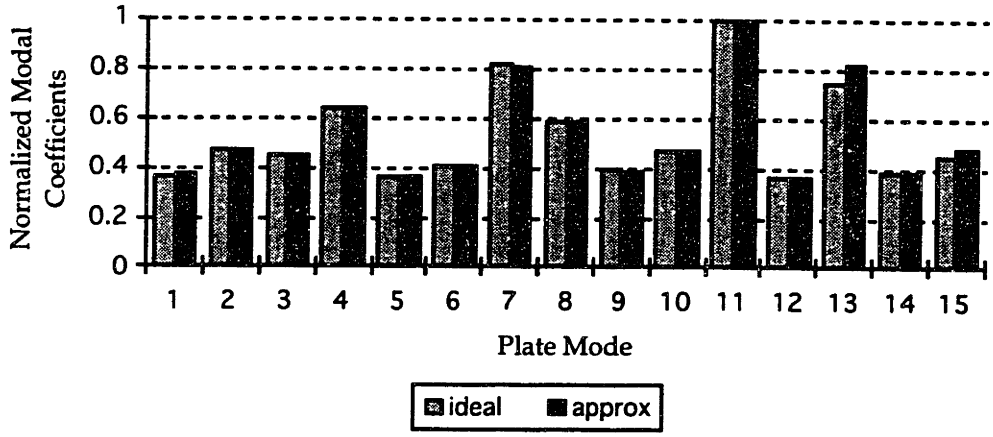

Fig. 3.23. Normalized modal coefficients of ideal (linear) shading and approximation.

The optimization results show that it is possible to obtain a close approximation to a desired continuous two-dimensional shading using gain-weighted, shaped transducers. This procedure can be extended to problems where it is desired to have the modal coefficients fit a pre-determined profile over mode number. One can envision such a profile as having relatively equal modal coefficients within a certain bandwidth with those coefficients outside of the bandwidth decreasing with increasing mode number. In this manner, the gain of a feedback controller could be increased to control modes within the bandwidth without destabilizing the modes outside of the bandwidth. This would allow spatial compensation using distributed transducers to compensate for temporal phase lags in a hardware implementation. Or, one might wish to target a small group of modes within a certain frequency range.

3.5 Summary

The motivation for two-dimensional transducer shading was presented and various methods for achieving shading were considered for the active control of thin plates. Two-dimensional transducer shaping was shown to be a useful design tool for the control problem. It was also shown that transducer shaping can be combined with gain-weighting to provide close approximation of continuously shaded transducer distributions. The analysis was applied to two

specific examples. One utilizes two-dimensional transducer shaping alone to establish controllability and observability over all but the even-even modes in a simply-supported plate. This transducer distribution is a very practical solution for the acoustic radiation attenuation problem. The second distribution is a superposition of gain-weighted, shaped transducer sections providing a good approximation to a continuous two-dimensional shaded transducer distribution. This distribution provides "all-mode" controllability and observability over a large bandwidth and is therefore useful for global vibration suppression in plates. An optimization method used to fit the approximation to the continuous transducer distribution over a specified number of modal coefficients was described. The following chapter will discuss an active control system for a plate based upon the design example given in this chapter.

3.6 References

1. C.-K. Lee and F.C. Moon, "Laminated Piezopolymer Plates for Torsion and Bending Sensors and Actuators," *Journal of the Acoustical Society of America*, **85**(6), pp. 2432-2439, June 1989.

2. S.E. Burke and J.E. Hubbard, Jr., "Distributed Transducer Vibration Control of Thin Plates," *Journal of the Acoustical Society of America* , **90**(2), pp. 937-944, August 1991.

3. R.L. Clark and C.R. Fuller, "Control of Sound Radiation With Adaptive Structures," *Journal of Intelligent Material Systems and Structures*, **2**(3), pp. 431-452, July 1991.

4. S.E. Burke and J.E. Hubbard, Jr., "Spatial Filtering Concepts in Distributed Parameter Control," *Journal of Dynamic Systems, Measurement, and Control*, 112, pp. 565-573, December 1990.

5. S.E. Burke and J.E. Hubbard, Jr., "Distributed Actuator Control Design for Flexible Beams," *Automatica*, **24**(5), pp.619-627, 1988.

6. S.E. Miller and J.E. Hubbard, Jr., "Observability of a Bernoulli-Euler Beam Using PVF_2 as a Distributed Sensor," *Proceedings of the 6th. VPI&SU/AIAA*

Symposium on Dynamics and Control of Large Structures, Blacksburg, VA, edited by L. Meirovitch, June 1987.

7. S.E. Burke and J.E. Hubbard, Jr., "Active Vibration Control of a Simply Supported Beam Using a Spatially Distributed Actuator," *IEEE Control Systems Magazine*, pp. 25-30, August 1987.

8. C.K. Lee and F.C. Moon, "Modal Sensors/Actuators," *ASME Journal of Applied Mechanics*, **57**, pp. 434-441, June, 1990.

9. C.K. Lee, W.W. Chiang and T.C. O'Sullivan, "Piezoelectric Modal Sensors and Actuators Achieving Critical Active Damping on a Cantilever Plate," *AIAA Paper*, 89-1390-CP, pp. 2018-2026, April 1989.

10. C.K. Lee, W.W. Chiang and T.C. O'Sullivan, "Piezoelectric Modal Sensor/Actuator Pairs for Critical Active Damping Vibration Control," *Journal of the Acoustical Society of America*, 90(1), pp. 374-383, 1990.

11. D.W. Miller, S.A. Collins and S.P. Peltzman, "Development of Spatially Convolving Sensors for Structural Control Applications," *AIAA Paper*, 90-1127 -CP, pp. 2283-2297, 1990.

12. R.L. Clark and C.R. Fuller, 1992, "Control of Sound Radiation With Adaptive Structures," *Journal of Intelligent Material Systems and Structures*, **2**(3), pp. 431-452, July 1991.

13. R.L. Clark and C.R. Fuller, "Modal Sensing of Efficient Acoustic Radiators With PVDF Distributed Sensors in Active Structural Acoustic Approaches," *Journal of the Acoustical Society of America*, **91**(6), pp. 3321-3329, 1992.

14. R.L. Clark, R.A. Burdisso and C.R. Fuller, "Design Approaches for Shaping Polyvinylidene Fluoride Sensors in Active Structural Acoustic Control," *Journal of Intelligent Material Systems and Structures*, **4**, pp. 354-365, 1993.

15. R.L. Clark and Burke, S.E., "Practical Considerations for Designing Shaped Modal Sensors From Polyvinylidene Fluoride," submitted to *ASME Journal of Vibration and Acoustics*, 1993.

16. E.K. Dimitriadis, C.R. Fuller and Rogers, C.A., "Piezoelectric Actuators for Distributed Noise and Vibration Excitation of Thin Plates," *Proceedings of the Eigth Biennial Conference on Failure Prevention and Reliability*, Montreal, Canada, pp. 223-233, September 1989.

17. S.E. Burke, J.E. Hubbard, Jr., and J.E. Meyer, "Colocation: Design Constraints for Distributed and Discrete Transducers," presented at the Symposium on Intelligent Structural Systems, 1991 ASME Thirteenth Biennial Conference on Mechanical Vibration and Noise, Miami, FL, September 1991.

Chapter 4:

Control System Analysis

4.1 Introduction

For a given structural control problem, one may construct an objective function based upon modal states which defines the performance metric. The modal states of the structure can be weighted such that penalties are assigned only to those modes which degrade performance. In the acoustic radiation problem, this function would penalize only those modes which had a significant contribution to the radiated sound field. In a global vibration problem, this function would attempt to damp all modes within an achievable control bandwidth.

Since structures are distributed parameter systems, choosing the control action which meets this objective function involves both temporal and spatial design.[1] Many researchers have studied the temporal aspects of the design problem in depth,[2] but have only considered the spatial part when determining observability and controllability for configurations of discrete transducers. As a result, the temporal solution becomes quite complex and, in order to achieve high-authority control, involves multi-input/multi-output compensators which depend upon detailed knowledge of the structure's temporal dynamics. In addition, unless model and/or controller order reduction techniques are used, the dimension of the controller may be equal to or even greater than the number of modes present in the structural response.

As discussed in the previous chapters, the use of distributed transducer design allows for more flexibility in the spatial part of the design problem. In fact, distributed transducer design may be used to directly satisfy the performance metric for the system. For example, it was shown in the last chapter that one transducer distribution could control or sense all of the odd-odd, even-odd, and odd-even modes in a simply-supported plate. The distribution *spatially* filtered out the even-even modes in the same plate. In this manner, the penalties

for the objective function for the acoustic radiation control problem were defined through the spatial design of the transducer distribution. The transducer could only actuate or sense those modes which had a significant contribution to the sound field. It was also shown in the last chapter that another transducer distribution, a superposition of gain-weighted, shaped transducer segments, provided modal coefficients of the same magnitude for a group of modes within a specified bandwidth. Thus, penalties are assigned evenly to these modes through the use of this transducer distribution.

If the transducer distribution can directly effect the desired penalties for the objective function, then the temporal part of the control design problem can be simplified considerably. A globally dissipative control law, such as velocity feedback,[3,4] can be combined with a colocated sensor and actuator distribution to provide a single-input/single-output compensator which is not dependent upon knowledge of the natural frequencies of the structure. Even though velocity feedback cannot discriminate between modes, the transducer distribution can be designed to spatially weight modes in a certain fashion to help accomplish mode-specific performance requirements.

In this chapter, a control system design is discussed which makes use of the gain-weighted, multi-section shaded transducer distribution discussed in the previous chapter. The governing equation of motion for a rectangular, simply-supported plate is presented with the input due to the controller included as the forcing term.[5] The sensor and actuator distributions are colocated on opposite sides of the plate.[6] Given transducer colocation, marginal stability is proven for any dissipative temporal control law. A proof of asymptotic stability is predicated upon an "assumed modes" closed-loop response and is therefore proven only for the linear viscous damping provided by velocity feedback. System matrices are then presented which allow for a simulation of the closed-loop system response.[6] Units are provided with each expression to allow for a dimensional check by the reader.

4.2 Plant and Transducer Characteristics

The plant to be controlled is a rectangular, simply-supported Bernoulli-Euler metal plate. This type of plate is frequently used as a basis for the study of

structural sound and vibration problems.[7] The plate, shown in Fig. 4.1, is augmented with a PVDF actuator distribution, Λ_a, on one side and a colocated PVDF sensor distribution, Λ_s, on the other. The result is a three-layer laminate, assumed to be mechanically transverse isotropic. Even if the PVDF distribution is anisotropic, the assumption of isotropy can still be made because the stiffness of the film is assumed to be small in comparison to that of the plate.

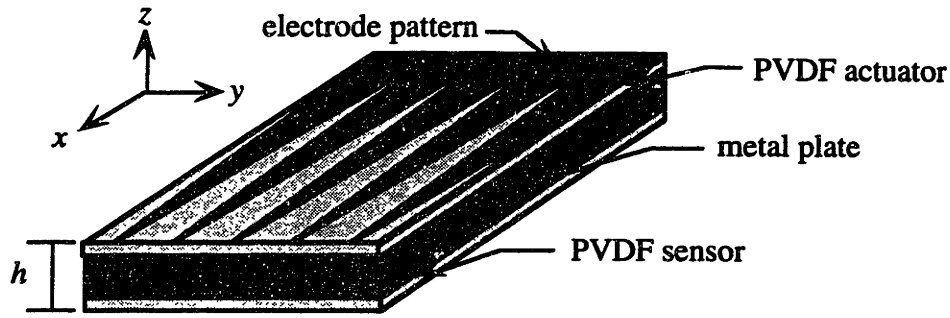

Fig. 4.1 Plate augmented with PVDF actuator and sensor.

Lee and Moon[5] derived the equation of motion for such a laminate with both PVDF layers used as actuators in a bimorph configuration. Mechanically, the system is the same. The difference occurs in the control input, which is halved in magnitude when only one layer is used as an actuator. The equation of motion for the system is given by

$$D_{11}\nabla^4 w + \rho h \frac{\partial^2 w}{\partial t^2} - T\nabla^2 w = u(\mathbf{x},t), \qquad (\mathrm{N/m^2}) \qquad (4.1)$$

where $w = w(\mathbf{x},t)$ is the transverse displacement of the plate and $u(\mathbf{x},t)$ is the control input due to the PVDF actuator. Lee and Moon did not include the effect of in-plane tension, T, but it has been included here for generality.

The left-hand side of equation (4.1) is the same as the conventional Bernoulli-Euler plate equation except that the constant terms include the laminate characteristics. The flexural rigidity D_{11}, is given by

$$D_{11} = \frac{h_m^3}{12}\left[\frac{Y_m}{(1-\nu_m^2)}\right] + h_p\left(\frac{h_m^2}{2} + h_m h_p \frac{2h_p^2}{3}\right)\left[\frac{Y_p}{(1-\nu_p^2)}\right], \qquad (\mathrm{Nm}) \quad (4.2)$$

where h_m is the thickness of the plate, h_p is the thickness of each PVDF layer, Y_m is the Young's modulus of the plate, Y_p is the Young's modulus of the PVDF, ν_m is Poisson's ratio for the plate, and ν_p is Poisson's ratio for PVDF. The equivalent density of the laminate, ρ, is

$$\rho = \frac{2\rho_p h_p + \rho_m h_m}{h_m + 2h_p}, \qquad (\text{kg/m}^3) \tag{4.3}$$

and the thickness of the laminate, h, is

$$h = h_m + 2h_p. \qquad (\text{m}) \tag{4.4}$$

The control input to the right-hand side of equation (4.1) is provided by the PVDF actuator and is separable in space and time:

$$u(\mathbf{x},t) = u(t)\, \varepsilon_a Z_p L[\Lambda_a(\mathbf{x})]. \qquad (\text{N/m}^2) \tag{4.5}$$

The temporal portion of the control input, $u(t)$, is given by

$$u(t) = G(t)\, h_p, \qquad (\text{V}) \tag{4.6}$$

where $G(t)$ is the applied electric field to the PVDF actuator. The product of the electric field and the thickness, h_p, yields an applied voltage across the faces of the PVDF.

The spatial portion of the control input is determined from the product of the piezoelectric differential operator acting on the actuator distribution, $L[\Lambda_a(\mathbf{x})]$ (N/Vm^3), the bonding efficiency of the actuator to the plate, ε_a, and the moment arm of the PVDF relative to the center of the plate, Z_p:

$$Z_p = \frac{h_m + h_p}{2}. \qquad (\text{m}) \tag{4.7}$$

The bonding efficiency is defined to be a positive number and less than or equal to 1. The moment arm extends from the center of the PVDF actuator layer to the center of the plate. A cross-section of the laminate is shown in Fig. 4.2. This figure shows the geometry in the transverse direction of the laminate.

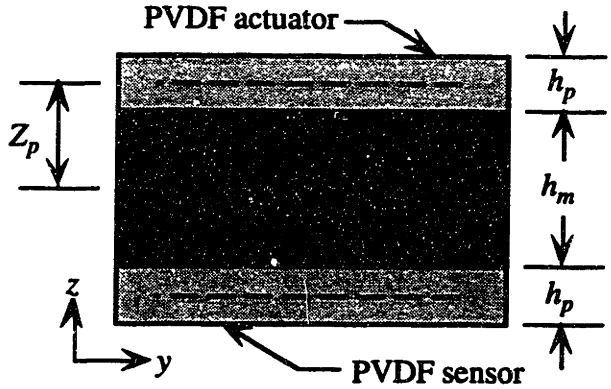

Fig. 4.2 Cross section of laminate.

The spatial extent of the laminate , Ω , extends over $0 < x < a$ and $0 < y < b$. The laminate is assumed to have simply-supported boundary conditions along all four edges such that the transverse displacement and moments at the boundary are zero:

$$w = 0, \frac{\partial^2 w}{\partial x^2} = 0 \quad \text{at} \quad x = 0, a; \tag{4.8}$$

$$w = 0, \frac{\partial^2 w}{\partial y^2} = 0 \quad \text{at} \quad y = 0, b. \tag{4.9}$$

4.3 Colocated Velocity Feedback: Marginal and Asymptotic Stability

This section will describe the stability achieved using a dissipative controller to provide the temporal part of the control input, $u(t)$, for the equation of motion of the laminate given in equation (4.1). The challenge in proving stability occurs because, while the system is linear and time-invariant, it is a distributed parameter system. In addition, because the linear Bournoulli-Euler plate model is only valid for small displacements from equilibrium, the stability proofs will hold for local stability only.

It is first important to demonstrate that a dissipative control law used for $u(t)$ will, at the very least, leave the system described in (4.1) marginally stable. This can be demonstrated using the direct method of Lyapunov. This method

involves defining an "energy-like" scalar quantity that is positive definite and proving that its time history is always at least negative semi-definite. This will correspond to zero growth in energy when the system is displaced from the equilibrium state. The following proof has been adapted from a proof for marginal stability for velocity feedback for distributed transducers by Burke and Hubbard.[6] It is presented here to provide a suitable review for the asymptotic stability proof developed later in this section.

The equilibrium state for the plate described in equation (4.1) is defined by,

$$\mathbf{w}(\mathbf{x},t) = [w(\mathbf{x},t)\ \dot{w}(\mathbf{x},t)]^T = \mathbf{0} \tag{4.10}$$

The theorem which formally describes the Lyapunov direct method for the determination of stability was described by Kalman and Bertram[8] and is quoted from Slotine and Li[9] here as:

Lyapunov Theorem for Local Stability:

If, in a ball $\mathbf{B}_{R_0}$, there exists a scalar function $V(\mathbf{w})$ with continuous first partial derivatives such that

- $V(\mathbf{w})$ is positive definite (locally in $\mathbf{B}_{R_0}$)
- $\dot{V}(\mathbf{w})$ is negative semi-definite (locally in $\mathbf{B}_{R_0}$)

then the equilibrium point $\mathbf{w} = \mathbf{0}$ is stable. If, actually, the derivative $\dot{V}(\mathbf{w})$ is locally negative definite in $\mathbf{B}_{R_0}$, then the stability is asymptotic.

Burke and Hubbard[6] used the total energy of the controlled laminate to define the scalar function, $V(\mathbf{w})$. The first three terms within the integral represent the strain energy due to the plate's stiffness. The fourth term represents the kinetic energy. The last three terms represent the strain energy due to the in-plane tension term.

$$V(\mathbf{w}) = \frac{1}{2}\int_{\Omega} D_{11}\left[(\nabla^2 w)^2 + \left(\frac{\partial^2 w}{\partial x\,\partial y}\right)^2 + \frac{\partial^2 w}{\partial x^2}\frac{\partial^2 w}{\partial y^2}\right] + \rho h\left(\frac{\partial w}{\partial t}\right)^2 + T\left[\left(\frac{\partial w}{\partial x}\right)^2 + \left(\frac{\partial w}{\partial x}\right)\left(\frac{\partial w}{\partial y}\right) + \left(\frac{\partial w}{\partial y}\right)^2\right] d\mathbf{x}. \tag{4.11}$$

This function is positive definite because it is zero when $\mathbf{w} = \mathbf{0}$ and it is positive whenever $\mathbf{w} \neq \mathbf{0}$. The next step in the proof for marginal stability involves the time derivative of this function.

The time derivative of the system energy can be represented as[6]

$$\dot{V}(\mathbf{w}) = \int_{\Omega} u(\mathbf{x},t)\left(\frac{\partial w}{\partial t}\right) d\mathbf{x}. \tag{4.12}$$

This expression has the familiar form of power since it is the product of stress and velocity integrated over the surface of the plate.

Taking into account the separability of the control input, equation (4.12) can be rewritten such that the temporal part of the control input moves out from under the spatial integration:

$$\dot{V}(\mathbf{w}) = u(t)\,\varepsilon_a Z_p \int_{\Omega} L[\Lambda_a(\mathbf{x})]\frac{\partial w}{\partial t}\, d\mathbf{x}. \tag{4.13}$$

Now, suppose that a dissipative control law is chosen for $u(t)$. This would have the opposite sign as the laminate velocity, $\frac{\partial w}{\partial t}$. Any control law which did not have the opposite sign of the plate velocity would add energy to the system and the energy functional would have to be modified accordingly. For example, a control law which has any position feedback has the effect of stiffening the structure and this adds strain energy to the structure. The controller based upon velocity feedback of the PVDF sensor signal is given by,

$$u(t) = -k\, f(t)\, sgn(\dot{v}_s); \qquad f(t) > 0, \tag{4.14}$$

where k is a positive scalar gain, $f(t)$ is any strictly positive scalar function and v_s is the voltage signal sensed by the PVDF sensor,

$$v_s(t) = \frac{\varepsilon_s Z_p}{c_s} \int_{\Omega} L[\Lambda_s(\mathbf{x})]\, w(\mathbf{x},t)\, d\mathbf{x}. \tag{4.15}$$

In the above expression ε_s is the bonding efficiency of the sensor and c_s is the capacitance of the sensor.

Substitution of the dissipative temporal control into the expression for the power flow yields,

$$\dot{V}(\mathbf{w}) = -k\, f(t)\, \varepsilon_a Z_p \operatorname{sgn}\left[\int_\Omega L[\Lambda_s(\mathbf{x})]\left(\frac{\partial w}{\partial t}\right) d\mathbf{x}\right]\left[\int_\Omega L[\Lambda_a(\mathbf{x})]\left(\frac{\partial w}{\partial t}\right) d\mathbf{x}\right]. \quad (4.16)$$

If the actuator and sensor, both of which are assumed to be made of PVDF, have the same spatial distribution such that $\Lambda_a(\mathbf{x}) = \Lambda_s(\mathbf{x}) = \Lambda(\mathbf{x})$, then they are colocated. The expression for power flow then simplifies to,

$$\dot{V}(\mathbf{w}) = -k\, f(t)\, \varepsilon_a Z_p \left|\int_\Omega L[\Lambda(\mathbf{x})]\left(\frac{\partial w}{\partial t}\right) d\mathbf{x}\right|. \quad (4.17)$$

Since all of the terms outside of the absolute value are defined to be positive, the power flow will always be negative semi-definite. The power flow is zero when the velocity, $\frac{\partial w}{\partial t}$, is zero, but is negative otherwise. Thus, marginal stability is guaranteed, but asymptotic stability cannot yet be determined because the power flow is not negative definite.

When the Lyapunov function, in this case defined by the system energy, is only negative semi-definite, asymptotic stability can still be determined through the use of the invariant set theorem.[10] The following definition for an invariant set is quoted from Slotine and Li:[9]

Definition of an Invariant Set

A set G is an invariant set for a dynamic system if every system trajectory which starts from a point in G remains in G for all future time.

This definition of an invariant set is used in the following local invariant set theorem, also quoted from Slotine and Li:

Local Invariant Set Theorem

Consider an autonomous system (where the system dynamics do not explicity depend upon time) of the form $\dot{\mathbf{w}} = \mathbf{f}(\mathbf{w})$ with f continuous, and let $V(\mathbf{w})$ be a scalar function with continuous first partial derivatives. Assume that

- for some $l > 0$, the region Ω_l defined by $V(\mathbf{w}) < l$ is bounded
- $\dot{V}(\mathbf{w}) \leq 0$ for all w in Ω_l

Let **R** be the set of all points within Ω_l where $\dot{V}(\mathbf{w}) = 0$, and **M** be the largest invariant set in **R**. Then, every solution $\mathbf{w}(t)$ originating in Ω_l tends to **M** as $t \rightarrow \infty$.

This theorem can be used to prove asymptotic stability provided that the only point contained within the set **M** is the equilibrium point $\mathbf{w} = \mathbf{0}$. In this manner, every state trajectory originating within Ω_l will asymptotically approach the equilibrium point.

In order to use the invariant set theorem, it is important to ascertain what the acceleration of the vibrating system will be at any nonzero value of displacement. To do this, it is assumed that the closed-loop displacement may be represented by the product of separable functions in space and time:

$$w(\mathbf{x},t) = \Phi(\mathbf{x})\eta(t). \tag{4.18}$$

This assumption has been studied for small values of linear proportional damping and was shown not to couple the modes of vibration.[11,12] Because the damping is assumed to be proportional, the asymptotic stability proof will only be carried out for the case of velocity feedback, known as "electronic damping."

Substituting equations (4.5) and (4.18) into equation (4.1) yields

$$\eta(t)\, D_{11}\nabla^4\Phi(\mathbf{x}) + \rho h\frac{d^2\eta(t)}{dt^2}\Phi(\mathbf{x}) - \eta(t)T\,\nabla^2\Phi(\mathbf{x}) = u(t)\,\varepsilon_a Z_p L[\Lambda(\mathbf{x})] \tag{4.19}$$

With velocity feedback used as the temporal control law,

$$u(t) = -k\,\dot{v}_s(t); \qquad k > 0, \tag{4.20}$$

and equation (4.18) used to describe the displacement, the control input may be represented as,

$$u(t) = -k\frac{d\eta(t)}{dt}\frac{\varepsilon_s Z_p}{c_s}\int_{\Omega}\Phi(\mathbf{x})\,L[\Lambda(\mathbf{x})]d\mathbf{x}. \tag{4.21}$$

Substituting equation (4.21) into equation (4.19) gives

$$\rho h \frac{d^2\eta(t)}{dt^2}\Phi(\mathbf{x}) + \eta(t)\left[D_{11}\nabla^4\Phi(\mathbf{x}) - T\,\nabla^2\Phi(\mathbf{x})\right] = -k\,\frac{d\eta(t)}{dt}\frac{\varepsilon_a\varepsilon_s Z_p^2}{c_s}\left\{\int_\Omega \Phi(\mathbf{x})\,L[\Lambda(\mathbf{x})]\,d\mathbf{x}\right\} L[\Lambda(\mathbf{x})]. \tag{4.22}$$

By multiplying both sides by the spatial portion of the response, $\Phi(\mathbf{x})$, and integrating over the domain of the laminate, the partial differential equation (4.22) can be put into the following form:

$$\rho h \frac{d^2\eta(t)}{dt^2}\left[\int_\Omega \Phi^2(\mathbf{x})d\mathbf{x}\right] + k\,\frac{d\eta(t)}{dt}\frac{\varepsilon_a\varepsilon_s Z_p^2}{c_s}\left\{\int_\Omega \Phi(\mathbf{x})\,L[\Lambda(\mathbf{x})]\,d\mathbf{x}\right\}^2 + \eta(t)\left\{\int_\Omega [D_{11}\Phi(\mathbf{x})\,\nabla^4\Phi(\mathbf{x}) - T\,\Phi(\mathbf{x})\,\nabla^2\Phi(\mathbf{x})]d\mathbf{x}\right\} = 0. \tag{4.23}$$

The result is an ordinary differential equation for a simple oscillator with positive coefficients. The coefficients multiplying the acceleration and velocity terms are positive, but the sign of the coefficient multiplying the displacement term is less easily determined. However, the sign of this coefficient can be checked by expanding the response into modes,

$$w(\mathbf{x},t) = \sum_{n=1}^{\infty} A_n\,\gamma_n\,\varphi_n(\mathbf{x})\,\eta_n(t). \tag{4.24}$$

Due to the simply-supported boundary conditions of the laminate, the mode shapes are sinusoidal in x and y,

$$\varphi_n(\mathbf{x}) = A_{rq}\,\gamma_{rq}\,\varphi_r(x)\,\varphi_q(y) = A_{rq}\,\gamma_{rq}\sin(r\pi x/a)\sin(q\pi y/b). \tag{4.25}$$

A positive number is obtained when the biharmonic operator, $\nabla^4[.]$, acting on an eigenfunction defined by (4.25) is multiplied by the same eigenfunction and a negative number is obtained when the Laplacian operator, $\nabla^2[.]$ acting on an eigenfunction is multiplied by the same function. Therefore, because both D_{11} and T are positive, the expression in the integrand in the last term of (4.23) will always be positive.

The acceleration of the laminate when its velocity is zero may now be written as

$$\frac{d^2\eta(t)}{dt^2} = -\eta(t)\frac{\left\{\int_\Omega [D_{11}\Phi(\mathbf{x})\nabla^4\Phi(\mathbf{x}) - T\,\Phi(\mathbf{x})\nabla^2\Phi(\mathbf{x})]d\mathbf{x}\right\}}{\rho h\left[\int_\Omega \Phi^2(\mathbf{x})d\mathbf{x}\right]}. \tag{4.26}$$

The result shows that the acceleration is always nonzero for nonzero values of displacement and the acceleration always has the opposite sign of displacement.

The invariant set theorem may now be applied to the problem to demonstrate asymptotic stability. The set **R** is the set of all points where $\dot{V}(\mathbf{w}) = 0$. This occurs whenever the velocity $\frac{d\eta(t)}{dt} = 0$. The largest invariant set, **M**, within **R** must only include the equilibrium point $\mathbf{w}(\mathbf{x},t) = \mathbf{0}$. This is because the acceleration will be nonzero for any nonzero displacement and so the only instance when the laminate will remain at a given state where $\dot{V}(\mathbf{w}) = 0$ for all time is when the laminate reaches the equilibrium state.

4.4 Simulation

To simulate the system, a state space representation is needed. Burke and Hubbard[13] defined the system matrices for a general transducer augmented distributed parameter system using an integral equation formulation such that the following input/output relationship could be defined

$$v_s(s) = \mathbf{G}(s)u(s) = [\mathbf{C}\Phi(s)\mathbf{B}]u(s), \tag{4.27}$$

where $v_s(t)$ is the sensor signal presented in equation (4.15), **C** is a vector of sensor modal coefficients, **B** is a vector of actuator modal coefficients, Φ is the state transition matrix and $u(s)$ is the Laplace-transform of the temporal control input to the system.

The actuator modal coefficient matrix has alternating zeros because the modal state vector consists of both modal displacements and velocities,

$$\mathbf{B} = [0\ b_1\ 0\ b_2\ \ldots\ 0\ b_N]^T. \tag{4.28}$$

The modal coefficients for the plate have the same definition as in the previous chapter except that they are now scaled by the bonding efficiency and moment arm,

$$b_n = \varepsilon_a Z_p \int_D \varphi_n(\mathbf{x})\, L[\Lambda(\mathbf{x})]\, d\mathbf{x}. \qquad \left(\frac{\sqrt{kg}\,m}{s^2 V}\right) \tag{4.29}$$

The mode shapes are now also mass-normalized such that,

$$\int_\Omega \rho h \left[\gamma_n \varphi_n(\mathbf{x})\right]^2 d\mathbf{x} = 1. \tag{4.30}$$

The normalization constant, γ_n, is

$$\gamma_n = \frac{2}{\sqrt{ab\rho h}}. \qquad (1/\sqrt{kg}) \tag{4.31}$$

Due to colocation, the sensor modal coefficient matrix, assuming a direct rate measurement, is equal to the transpose of the actuator modal coefficient matrix,

$$\mathbf{C} = [0\ c_1\ 0\ c_2\ \ldots\ 0\ c_N]\,. \tag{4.32}$$

The sensor modal coefficient matrix for the plate, however, differs from the actuator matrix by a constant which is the capacitance of the sensor:

$$c_n = \frac{k_d \varepsilon_a Z_p}{C_p} \int_D \varphi_n(\mathbf{x})\, L[\Lambda(\mathbf{x})]\, d\mathbf{x}\,, \qquad \left(\frac{Vs}{\sqrt{kg}\,m}\right) \tag{4.33}$$

$$C_p = \left(\frac{1}{2} a\, b\right) c_p\,. \qquad (F) \tag{4.34}$$

The state transition matrix has a block diagonal form ordered by mode number,

$$\Phi = diag\,(\Phi_1, \Phi_2, \ldots \Phi_N)\,. \tag{4.35}$$

Each block is related to the plant matrix for each mode.

$$\Phi_n = (s\mathbf{I} - \mathbf{A}_n)^{-1}\,. \tag{4.36}$$

The plant matrix for each mode consists of the natural frequency and the modal damping term,

$$\mathbf{A}_n = \begin{bmatrix} 0 & 1 \\ -\omega_n^2 & -2\zeta_n\omega_n \end{bmatrix}. \tag{4.37}$$

These individual plant matrices can be assembled into one plant matrix describing the system dynamics.

$$\mathbf{A} = diag\,(\mathbf{A}_1, \mathbf{A}_2, \ \ldots\ \mathbf{A}_N)\,. \tag{4.38}$$

The system can then be defined by the modal state equations, where the vector η contains the modal displacements and velocities:

$$\dot{\vec{\eta}} = \mathbf{A}\vec{\eta} + \mathbf{B}u\ . \tag{4.39}$$

and the scalar y_s represents the sensor output:

$$y_s = \mathbf{C}\,\eta. \tag{4.30}$$

Fig. 4.3 shows a simulation of an uncontrolled simply-supported plate after an impact. The sensor output is shown as a function of time. Fifteen modes were included in the simulation with 0.5% damping assumed for each mode. Fig. 4.4 shows a simulation of the same plate with velocity feedback applied. The gain used in this case is large enough such that the maximum voltage applied to the actuator array is 400 Volts. It was assumed in this simulation that a perfect rate measurement of the sensor array was available, that there were no limiting actuator dynamics, and that the actuator and sensor arrays were perfectly bonded to the plate. It can be seen from the simulations that the velocity feedback controller adds to the linear damping already present in the system. The decay envelope shape does not change, but the settling time is reduced significantly. It is also seen that the modes are evenly penalized in that there is no mode which dominates the closed-loop response.

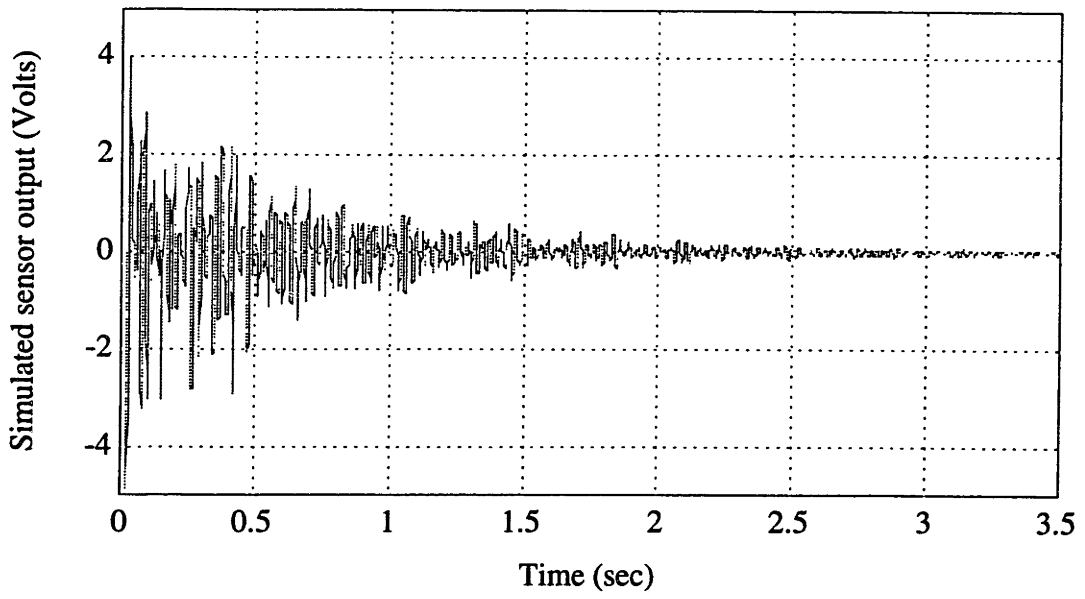

Fig. 4.3 Simulated impact response of plate: no control input.

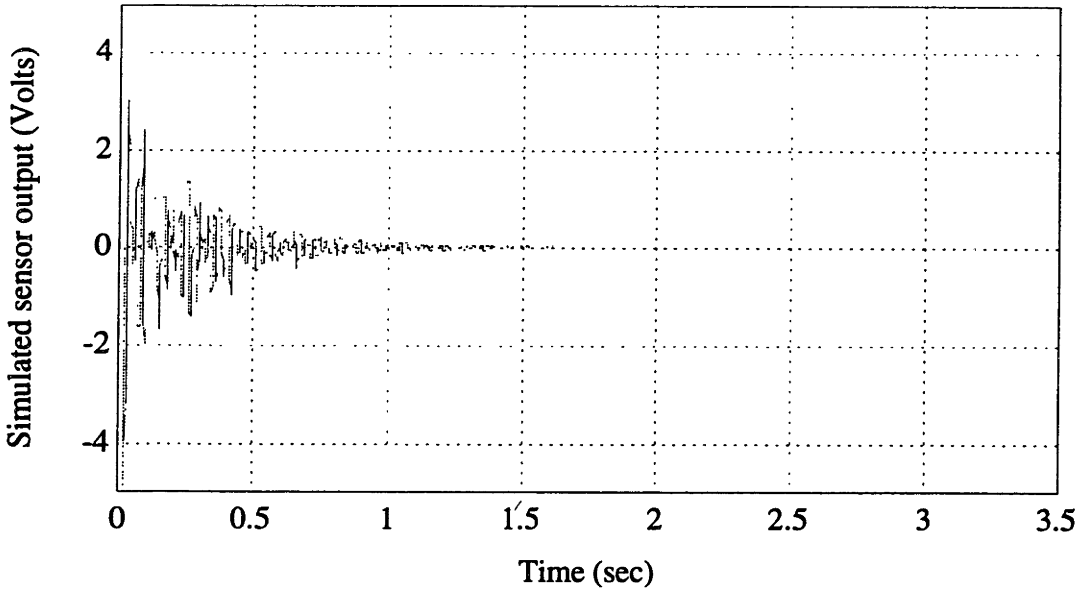

Fig. 4.4 Simulated impact response of plate: velocity feedback.

The balanced modal coupling in the system is evident when looking at the calculated open-loop frequency response function between the actuator array and the sensor array shown in Fig. 4.5. This shows that the transducer distribution couples evenly into the modes of the system. The alternating pole/zero pattern is due to the colocation of the actuator array with the sensor array.

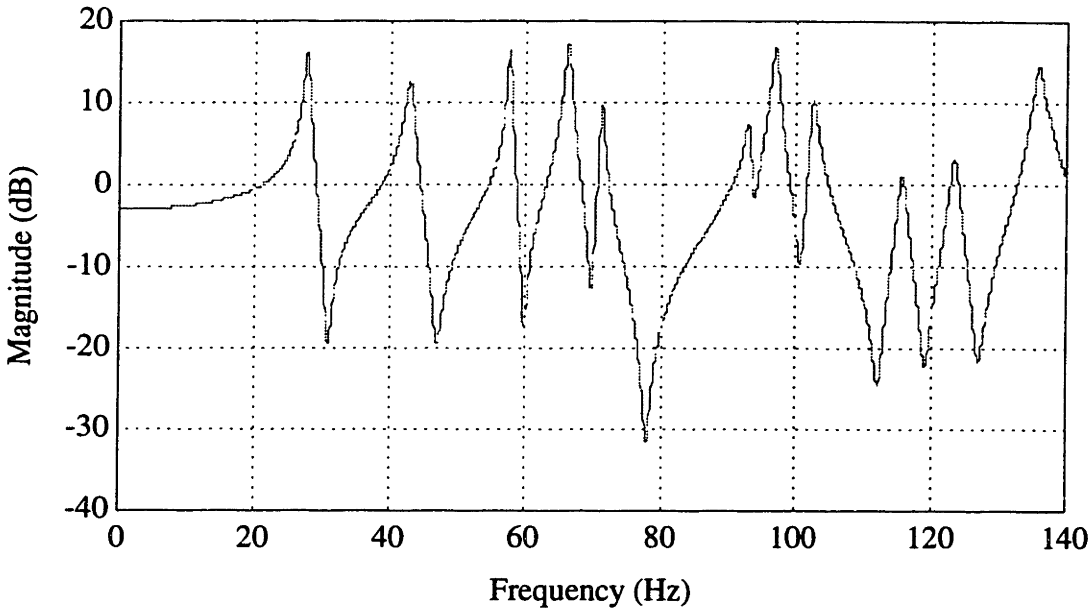

Fig. 4.5 Calculated open-loop frequency response function.

4.5 Summary

This chapter described the plant and transducer setup and dynamics. A rectangular, three-layer laminate plate which was simply-supported at the edges was used as a sample problem. Marginal stability was proven for any dissipative controller. Asymptotic stability was proven for the case of velocity feedback. The state matrices were then presented for the distributed parameter system so that the system was able to be simulated easily using MATLAB. The results of the simulations show the behavior of the simply-supported plate when velocity feedback is used as the control input.

The experimental work in the following chapter utilizes both of the sensor and actuator distributions along with velocity feedback to perform a validation of the concepts described above. Although the experimental plate has boundary conditions lying between simply-supported and clamped, the behavior of the experimental system under closed-loop control should be similar to that shown by the simulations in this chapter. The control should add damping to all of the modes within the disturbance bandwidth.

4.6 References

1. S.E. Burke and J.E. Hubbard, Jr., "Spatial Filtering Concepts in Distributed Parameter Control," *Journal of Dynamic Systems, Measurement, and Control*, Vol. 112, pp. 565-573, December, 1990.

2. D.C. Hyland, J.L. Junkins, and R.W. Longman, "Active Control Technology for Large Space Structures," *Journal of Guidance Control and Dynamics*, **16**(5), pp. 801-821, September-October 1993.

3. J. Canavin, "The Control of Spacecraft Vibration Using Multivariable Output Feedback," Paper 78-1419, *AIAA/AAS Conference on Large Space Platforms*, Los Angeles, CA, August 1978.

4. M. Balas, "Direct Velocity Feedback Control of Large Space Structures," *Journal of Guidance and Control*, **2**(3), pp. 252-253, May-June 1979.

5. C.-K. Lee and F.C. Moon, "Laminated piezopolymer plates for torsion and bending sensors and actuators," *Journal of the Acoustical Society of America*, **85**(6), pp. 2432-2439, June 1989.

6. S.E. Burke and J.E. Hubbard, Jr., "Distributed transducer vibration control of thin plates," *Journal of the Acoustical Society of America* , **90**(2), pp. 937-944, August 1991.

7. P.W. Smith, Jr. and R.H. Lyon, *Sound and Structural Vibration*, NASA CR-160.

8. R. Kalman and J. Bertram, "Control Systems Analysis and Design via the 'Second' Method of Lyapunov," *Transactions of ASME, Journal of Basic Engineering*, pp. 371-400, 1962.

9. J.J. Slotine and W. Li, **Applied Nonlinear Control**, Prentice Hall, Englewood Cliffs, 1991.

10. J. La Salle and S. Lefschetz, **Stability by Liapunov's Direct Method**, Academic Press, 1961.

11. T.K. Hasselman, "Modal Coupling in Lightly Damped Structures," AIAA Journal, **14**(11), pp. 1627-1628, November 1976.

12. A.H. Flax, "Comment on 'Modal Coupling in Lightly Damped Structures'", AIAA Journal **15**(11), p. 1662, November 1977.

13. S.E. Burke and J.E. Hubbard, Jr., "Distributed Transducers, Collocation, and Smart Structural Control," *SPIE 1990 Technical Symposium on Optical Engineering and Photonics in Aerospace Sensing*, Orlando, FL, April 1990.

Chapter 5:

Experimental Demonstration: Active Vibration Damping of a Bernoulli-Euler Plate

5.1 Introduction

This chapter describes an experiment which embodies and validates the modeling and design concepts developed in Chapters 2 and 3. In these chapters, it was shown that two-dimensional distributed transducers can be designed to have controllability and observability over a large modal group, and that the modal coefficients would have the same magnitude, e.g. balanced coupling.

The transducer distribution used for the active control of the plate described in this chapter was the "all-mode" distribution composed of gain-weighted, shaped transducer segments developed in Chapter 3. This transducer distribution facilitates global sensing and control over a wide bandwidth. It was decided to demonstrate global vibration suppression using this transducer distribution. The control bandwidth chosen for this experiment included the first 15 modes of the plate. These modes include all of the types of modal symmetry present in a simply-supported plate.

The test article was a rectangular Bernoulli-Euler aluminum plate. To approximate simply-supported boundary conditions, a 90 deg V-notch was milled around the perimeter of the plate and the excess material was clamped in a rigid test fixture.[1] In this manner, the plate has zero deflection at the notch, but is allowed to have angular displacement there. This approximates a simply-supported, or hinged, boundary condition with a rotational constraint. Figure 5.1 shows a cutaway view of the plate alongside the theoretical boundary condition model. As the ratio of the notch depth to plate thickness increases, the effective spring constant of the rotational spring will decrease.[1] When this ratio decreases to zero, the spring constant approaches infinity and the plate will have a clamped boundary condition.

This plate configuration was chosen because the mode shapes will have the same symmetries as those for a simply-supported plate and so the theoretical work in the previous chapters can be applied.

The rest of this chapter is organized as follows. Section 5.2 describes the plate and clamping fixture. The results of a modal test of the plate are given in section 5.3. Section 5.4 describes the application of distributed piezopolymer film transducer to the plate. Section 5.5 presents the results of an open-loop test of the structure, a transfer function between the actuator and the sensor distribution. Section 5.6 shows the results of closed-loop tests of the structure using velocity feedback in the presence of both transient and stochastic disturbance inputs. In addition, a test characterizing the interaction of the PVDF sensor array with the acoustic environment is described. Finally, conclusions and recommendations for future work are given in section 5.7.

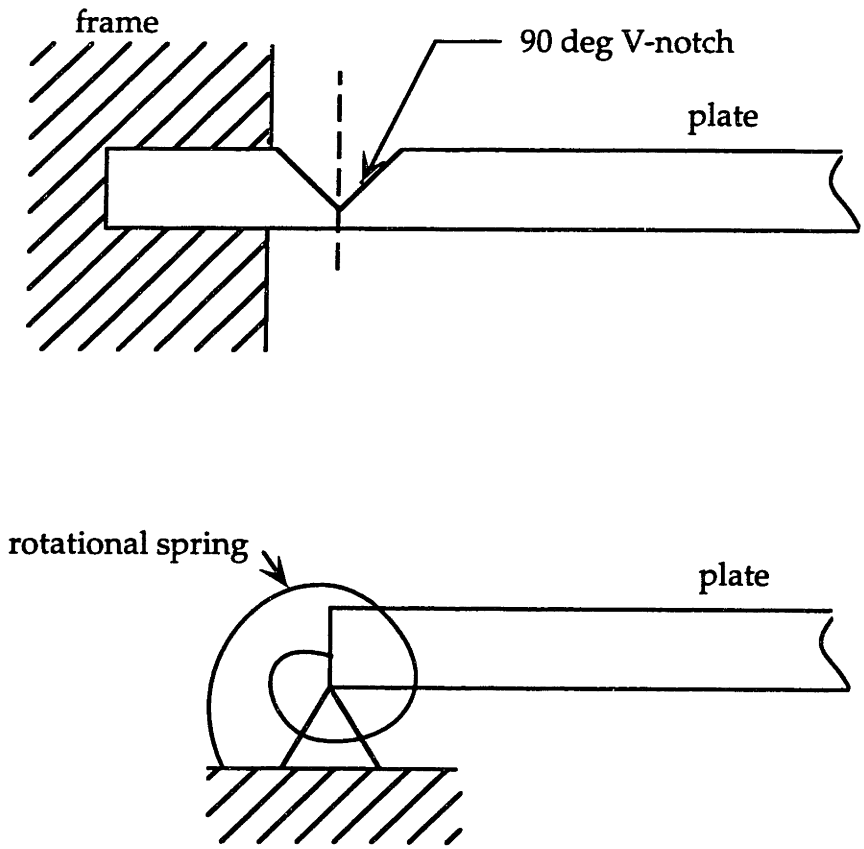

Fig. 5.1 Side view of plate with V-notch compared to simply-supported plate with rotational edge constraint.

5.2 Experimental Plate and Test Fixture

The aluminum plate (ρ = 2710 kg/m^3, E = 69.6 x 10^9 Pa) and steel mounting frames (ρ = 7840 kg/m^3, E = 202.0 x 10^9 Pa) are shown in Fig. 5.2. A vertical support configuration was chosen to permit access for a shaker input disturbance and to eliminate much of the in-plane tension due to gravity (e.g. sag). The plate is sandwiched between the two steel mounting frames. The notch of the plate is milled at the boundary where the plate meets the clamping frames. The plate is made from 6061-T6 flat sheet aluminum. The plate is 1/32 (0.031) inch thick and the dimensions of the plate between the centerlines of the notch are 26.4 inches by 18.5 inches. The notch was milled using a numerically controlled milling machine to a depth of 0.024 inches.

The clamping frames were designed to have significant mass in comparison to the plate. The frames were made from cold-rolled steel bars welded together and milled to the desired flatness of 0.001 inches. The frames were clamped to each other and the plate using 3/8 inch cap screws. The plate and frames were supported vertically by an alumimum support made from I beams and L beams. The entire structure was mounted to a floating Newport optics table. This was done to prevent building structural vibrations from contaminating the experiment.

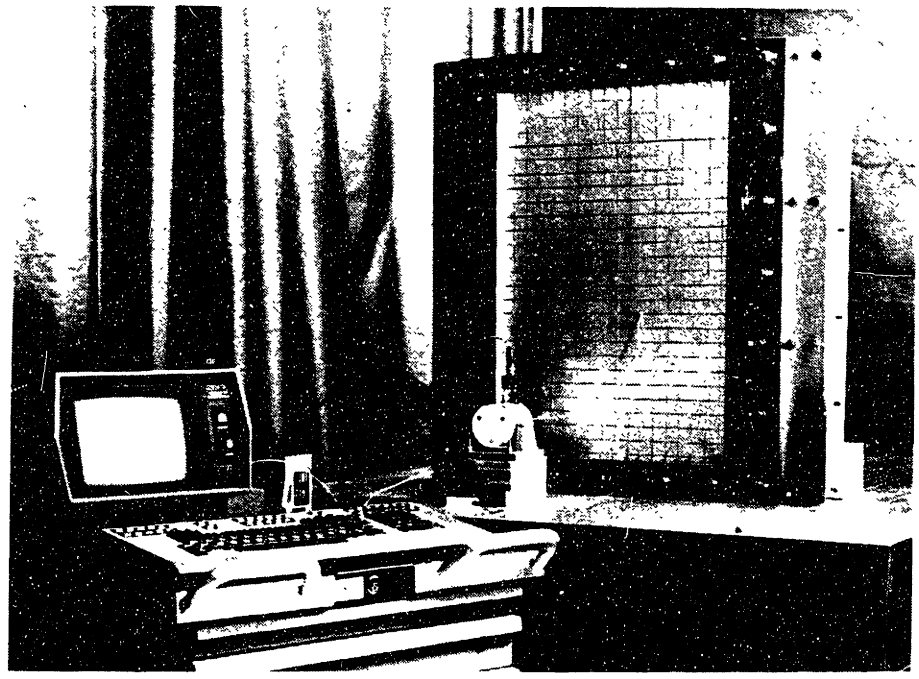

Fig. 5.2. Experimental plate and clamping frames.

5.3 Modal Test

A modal test was conducted to verify that the experimental plate had mode shapes which were similar to the simply-supported plate discussed in Chapter 3. The same symmetries and mode order were expected due to the symmetric boundary condition and the plate's aspect ratio. Due to the rotational edge constraint, it was expected that the slope of the mode shapes near the boundary of the plate would be smaller than for a simply-supported plate which has no rotational constraint.

The modal test was conducted using a Zonic 6088 spectrum analyzer. The analyzer has a signal source output which drove a Ling V203 shaker with a low-passed random noise signal. The cutoff frequency chosen for the tests was 125 Hz. The shaker was connected to a steel stinger, which was in turn connected to a PCB force head model 209. The force head was attached to the plate with cyanoacrylate adhesive. An Entran EGA-125-5D 0.5 gram accelerometer was used as the roving sensor for the modal test. The accelerometer was attached to the plate using a thin layer of beeswax. The modal test setup, with the shaker and accelerometer, is shown in Fig. 5.1.

Ninety-nine test points were used- eleven across the length of the plate and nine across the width. The Zonic was set up for continuous processing with Kaiser-Bessel windowing and 50% overlap. Thirty averages were used to calculate the frequency response function at each location.

The Zonic's built-in modal analysis software was used to fit the frequency response functions to a multiple degree of freedom model. The frequency and damping results are shown in Table 5.1. Two modes were overlapping in frequency. The ordering of the modes is the same as expected for a simply-supported plate with the same aspect ratio.

Table 5.1 Frequency and damping values for experimental plate.

Mode	Frequency (Hz)	Damping (%)
(1,1)	43.82	0.44
(2,1)	54.53	0.44
(3,1) & (1,2)	65.49	0.36
(2,2)	67.19	0.34
(3,2)	84.30	0.32
(4,1)	87.42	0.35
(1,3)	90.14	0.35
(2,3)	103.14	0.34
(4,2)	108.17	0.37
(5,1)	118.41	0.25

The mode shapes obtained from the test were similar to the simply-supported mode shapes, with the exception of a decreased slope near the boundary. This was expected due to the rotational edge constraint. However, the modes had the same symmetry and ordering as for a simply-supported plate. Several example shapes are shown in Figures 5.3, 5.5, and 5.7. The corresponding simply-supported mode shapes are shown in Figures 5.4, 5.6, and 5.8 for comparison.

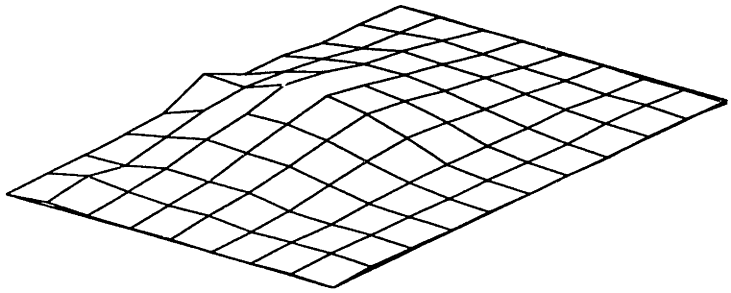

Fig. 5.3 Experimental (1,1) mode shape.

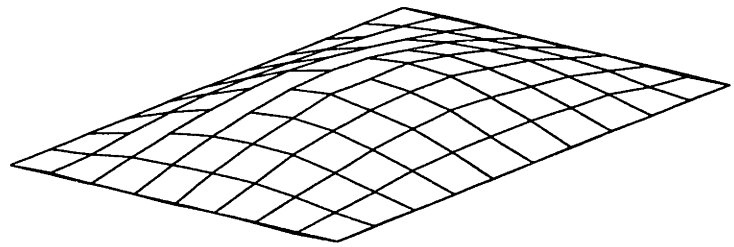

Fig. 5.4 Theoretical simply-supported (1,1) mode shape.

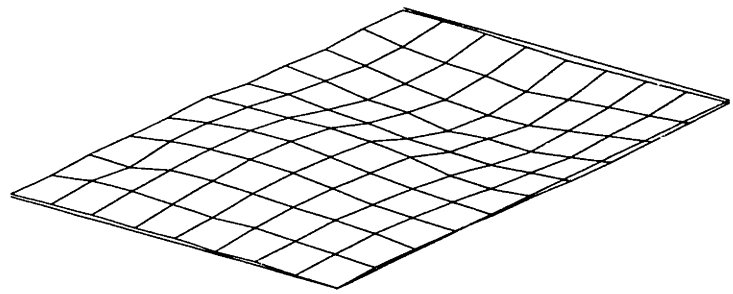

Fig. 5.5 Experimental (2,1) mode shape.

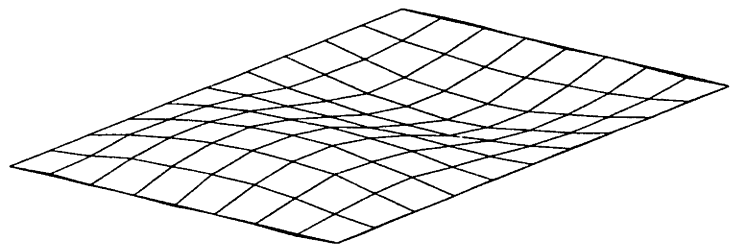

Fig. 5.6 Theoretical simply-supported (2,1) mode shape.

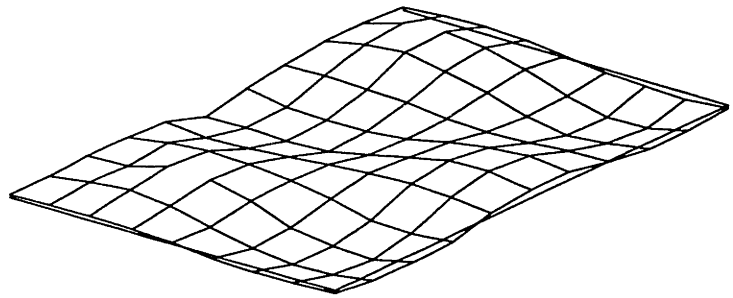

Fig. 5.7 Experimental (3,2) mode shape.

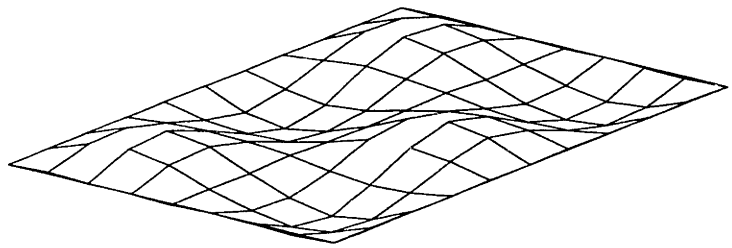

Fig. 5.8 Theoretical simply-supported (3,2) mode shape.

5.4 Transducer Application

The transducer material used for this experiment is Atochem uniaxial, 52μm, piezopolymer film (PVDF) with a nickel-aluminum electrode coating. It is flexible, available in large areas, and can be cut to any shape. Both the sensor distribution and actuator distribution were constructed from this material. These distributions were identical, and placed on opposite sides of the plate. The sensor distribution is shown in Fig. 5.9 and the actuator distribution, on the back side of the plate, is shown in Fig. 5.10. Their construction and application is discussed in this section.

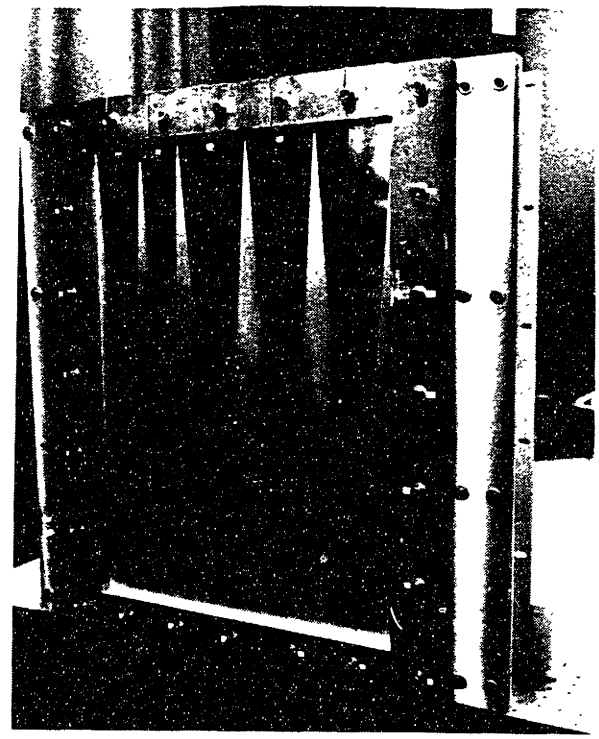

Fig. 5.9 Sensor distribution on experimental plate.

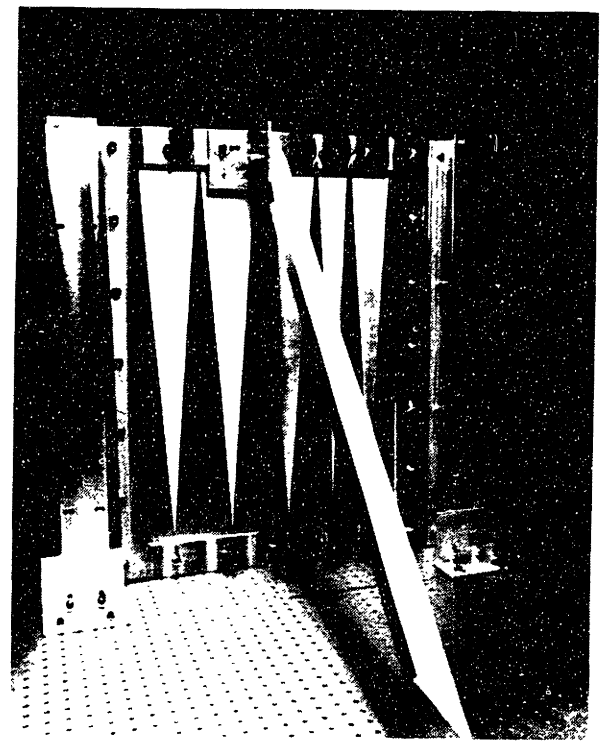

5.10 Actuator distribution on experimental plate.

The method for cutting the film and attaching it to the plate was adapted from Burke.[2] The techniques are briefly reviewed here along with the additional experience gleaned from cutting the large area transducers needed for this experiment.

The PVDF film was measured, marked, and laid out to be cut on a flat surface. A large straight edge was placed along the film where a cut was to be made and taped down to the cutting surface using masking tape. Care was taken not to allow the tape to touch the film. With the straight edge pressed against the film this way, one does not have to hold it down while making a long cut. This helped to prevent cutting mistakes. The film was cut using single-edged razor blades. The film is tough enough to dull the razor blade, so only one cut was made with each blade.

A kitchen "scrunge" pad was used to prepare the aluminum plate for application of the PVDF. After the surface of the plate was polished, the locations of the film were marked using an etching tool. The entire plate was wiped clean with acetone to remove any remaining particles.

The transducers were laminated to the plate using a mixture of four parts RBC 3215 epoxy resin with one part RBC AB-532 resin hardener. The mixture was applied to the plate using a 1 inch foam brush. The layer was partially evened out using a straight-edge razor blade. The transducer section was then wrapped around an acrylic cylinder. It was then slowly rolled onto the epoxy layer on the plate while pressing down to eliminate air bubbles trapped beneath the film. Air bubbles and excess epoxy were then worked out from underneath the film by hand. Various brayers, rubber then acrylic, were then rolled over the area of the film. This serves to ensure a thin, uniform bond between the film and the plate. The film, with electrode coating, should have a mirror-like finish when the procedure is complete. This result can be seen by the light reflected from the sensor distribution shown in Fig. 5.9.

After the piezo film had been laminated to the plate, small brass contact pads were attached to the "roots" of the transducer film sections using Tra-Con Tra-Duct BA-2902 conductive epoxy. Stranded wire, 26 guage, was soldered to the pads to provide the needed electrical connections to the film.

This was done before attaching the pads to the film so that no heat would be applied to the film that might locally depolarize it.

The actuator distribution in Fig. 5.10 looks different than the sensor distribution shown in Fig. 5.9 because the nickel-aluminum electrode coating was fortified with Chomerics Cho-Shield conductive acrylic spray. This was done because the film's electrode layer was too thin to handle the high voltage that can be applied to the actuators. One six-ounce spray can was used to cover the actuator array. Drafting tape, which will not harm the PVDF, was used to mask the plate around the PVDF actuator before applying the conductive acrylic spray. This spray coating causes the pale, non-reflective finish of the actuators seen in Fig. 5.10.

A Faraday cage made from aluminum window screen was placed over the mounting frame, covering the actuator side of the plate so as to prevent electromagnetic cross-talk between the actuator and sensor distributions.

5.5 Open-Loop Test

An open-loop measurement of the frequency response function between the actuator and the sensor distribution was conducted to verify that the actuator and sensor arrays were colocated and to verify that the distributions coupled evenly into the modes of the structure as predicted in Chapter 3. A schematic of the signal flow for the open-loop test is shown in Fig. 5.11.

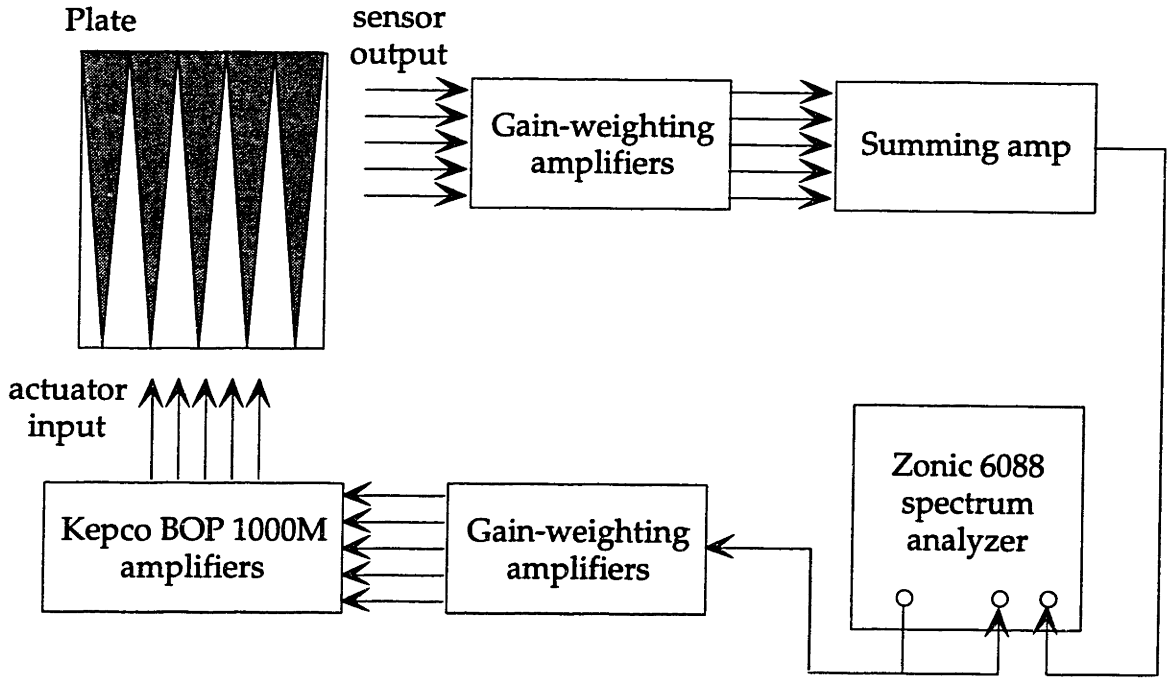

Fig. 5.11 Signal flow for open-loop test of actuator and sensor.

In this configuration, the system is single-input/single-output. The output from each PVDF sensor segment is individually gain-weighted. Then, all of the gain-weighted sensor outputs are added together in a summing amplifier. The resulting single output signal is then fed to the Zonic spectrum analyzer. The signal source of the Zonic is used to provide one signal which drives a similar array of gain-weighting amplifiers for the actuator distribution. This signal is also given to the Zonic for use in the frequency response function calculation. The output from each of the actuator gain-weighting amplifiers is then passed to a Kepco BOP-1000M bipolar operational power supply/amplifier which amplifies the voltage by 100 so as to drive the PVDF actuators. Since the plate itself served as a common ground, the Kepco amplifiers were run with fully differential outputs in the voltage mode. Originally, the signal from the Zonic was to be passed through one Kepco amplifier which would then drive a voltage divider which would have provided the gain-weighted signal to each actuator segment. This proved to be difficult to accomplish because the PVDF had a large capacitance, and the voltage divider formed a low-pass network with the actuator segments, thus rolling off the signal for each segment over frequencies below the desired controller bandwidth.

The sensing electronics are shown in Fig. 5.12. The input voltage, sourced from each sensor segment, is passed through a non-inverting, gain-weighting amplifier. The values of R_1 and R_2 are varied to obtain the correct gain for the sensor voltage. R_2 included a potentiometer so that this gain could be precisely adjusted. The dotted lines on the figure indicate leads to the other gain-weighting amplifiers. Each of the resulting voltages is added together through the summing amplifier. Also shown on the schematic is the differentiator used to provide the velocity signal used for feedback. This differentiator was tested individually and was not included in the open-loop test results that follow.

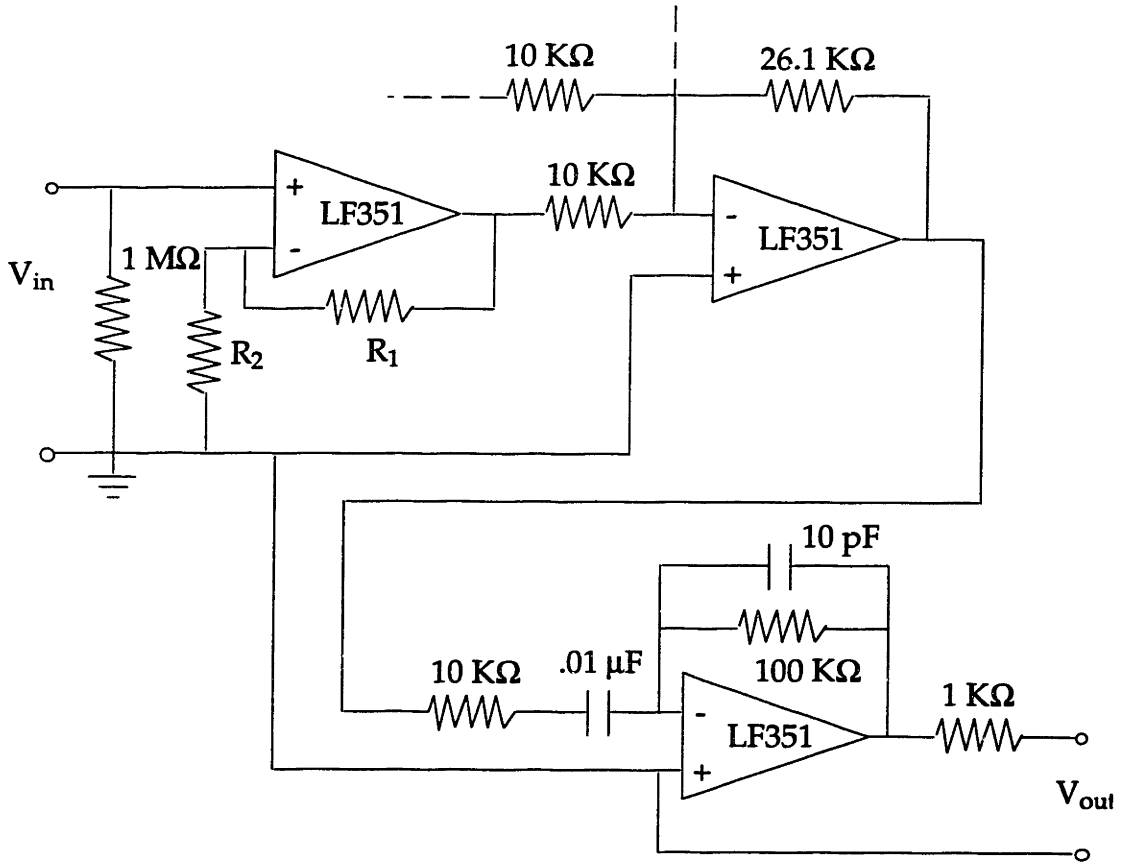

Fig. 5.12 Sensor electronics including gain-weighting amplifier, summing amplifier, and differentiator

Table 5.2 Amplifier gains and resistor ratios for amplifying electronics.

Pennant	Amplifier Gain	R_1/R_2
1	9.131	8.131
2	7.578	6.578
3	5.724	4.724
4	3.452	2.452
5	1.175	0.175

The open-loop test was conducted using low-passed random noise from the Zonic signal source with a cutoff frequency of 125 Hz. The resulting frequency response function is given in Fig. 5.13. For the most part, the response function has the expected alternating pole/zero pattern shown in Fig. 4.5 in Chapter 4. This verifies colocation of the gain-weighted actuator array with the gain-weighted sensor array. The only anomalies were a 60 Hz noise spike, the region around 25 Hz, and the region between 40 and 50 Hz. The coherence around all of these frequencies was poor. The 60 Hz noise was expected due to the line voltage, but the poor coherence in the 25 Hz region and the 40-50 Hz region were not. The phenomena associated with the 25 Hz and 40-50 Hz regions are identified in the next section.

One notes that the modal peaks in the frequency response function are all of the same order of magnitude. This demonstrates that the transducer distribution couples evenly into the modes of the structure within the disturbance bandwidth as predicted in Fig. 4.5 in Chapter 4. Thus, all of the modes excited by the disturbance are penalized evenly by the control action so that global vibration performance can be achieved.

The frequency locations for the peaks are all lower than they were for the modal tests. There are several reasons for this. In order to attach the transducers, the plate and text fixture had to be disassembled. The disassembly and then reassembly could have had a part in changing the natural frequencies because the boundary conditions could have changed. In addition, the epoxy used to attach the transducers to the plate adds damping

to the plate. The combination of the transducers, epoxy, brass pads, and conductive acrylic spray added mass to the plate. The effect of added mass and added damping is to lower the natural frequencies of the plate.

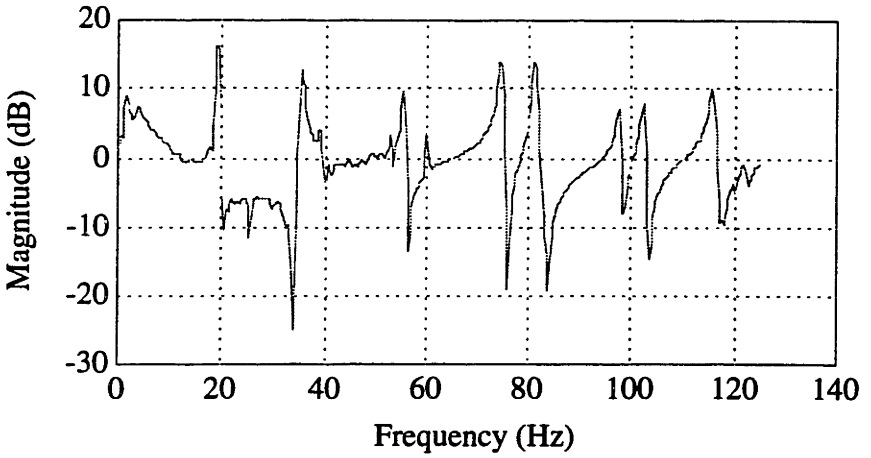

Fig. 5.13 Open-loop transfer function between actuator and sensor.

5.6 Closed-Loop Testing

Closed-loop tests were conducted to show that using velocity feedback with the transducer distributions would result in a stable system with added damping. A schematic of the signal flow for the closed-loop tests is shown in Fig. 5.14.

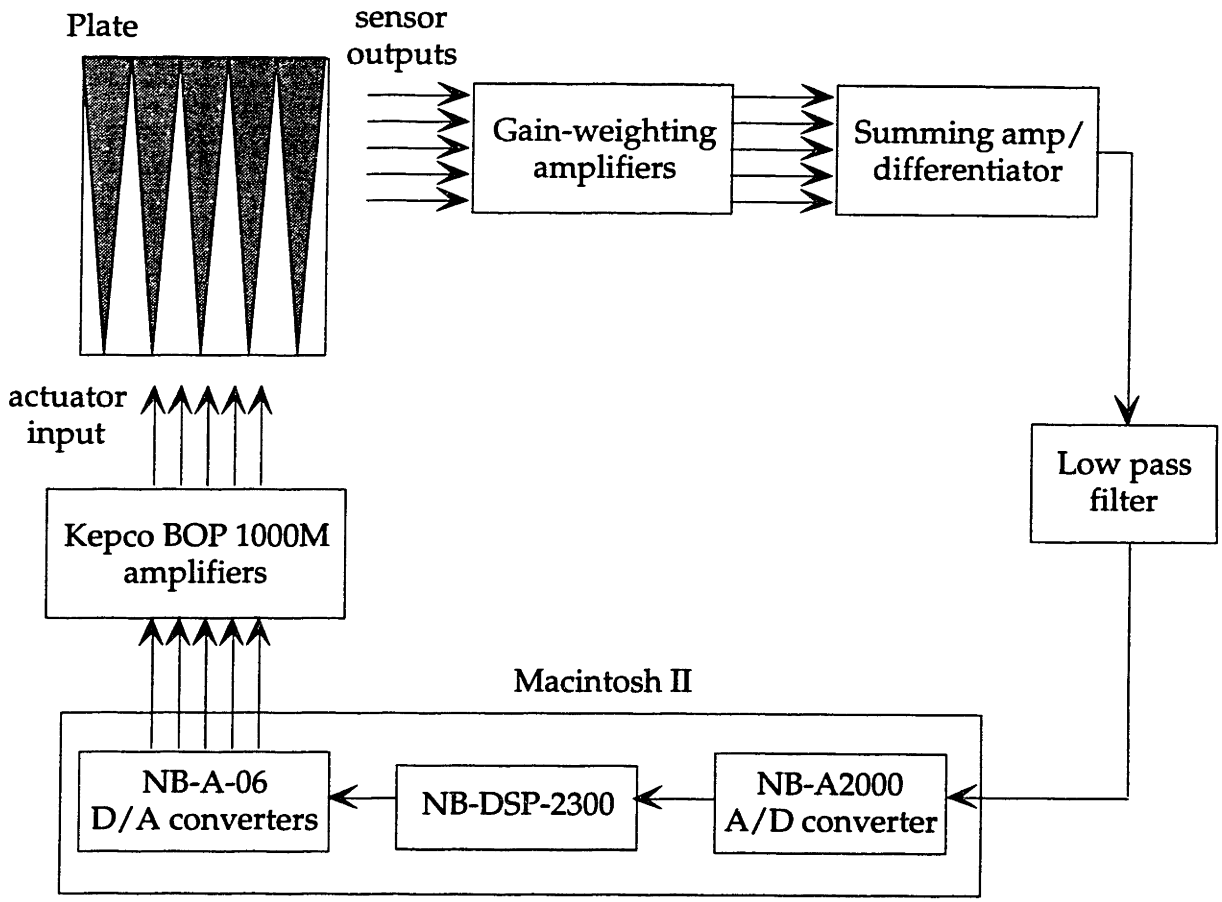

Fig. 5.14 Signal flow for closed-loop tests.

The signal flow for the closed-loop tests is similar to that for the open-loop test except that the sensor array output from the summing amplifier is now passed through an analog differentiator to provide a velocity signal and this is, in turn, passed through an Ithaco 4302, 24 dB/octave, low pass filter, set to a 1000 Hz bandwidth, to eliminate high-frequency noise signals. The PVDF electrodes are large enough to allow the sensor distribution to behave as an antenna and pick up high-frequency electromagnetic interference. The output of the low pass filter is then passed to the Macintosh II control computer. The Macintosh II contains three boards made by National Instruments (NI). The NI NB-A2000 A/D converter samples the signal from the low pass filter at a rate of 10,000 Hz. This digitized data is in turn passed to the NI NB-DSP-2300 digital signal processor board in the control computer. The DSP computes the control action and sets saturation limits on the allowable control voltage. The computed control signal is then gain-weighted

for each actuator segment before passing the values to 5 channels of the NI NB-A0-6 D/A converter. Both the sensor and control signal are saved by the DSP board to a daughter memory board for analysis after the control experiment. The D/A converter drives the inputs of the Kepco amplifiers which provide the necessary control voltages for the PVDF actuator segments. The entire control loop is run synchronously at the sampling rate of 10 KHz. This is accomplished by using the sample clock signal of the A/D converter to update the D/A converter. During the contro

A band-limited impulse disturbance was employed to quantify the settling time of the actively-controlled plate in comparison to its open-loop response. A foam-covered ball was used to provide the input. The ball was suspended in a pendular fashion so as to provide reasonably repeatable impacts to the plate. The power spectral density of the sensor signal with the disturbance showed that the disturbance had a bandwidth of approximately 150 Hz. This excited the first 15 modes of the plate.

The time response of the plate using velocity feedback as the closed-loop control law is plotted along with the open-loop (uncontrolled) response in Fig. 5.15. For the closed-loop control experiment, the controller was turned on before the impact. The gain chosen for the velocity feedback was the maximum that could be used before high-frequency modes of the plate were driven unstable. As expected, the highest gain demonstrated the best damping performance. The settling time was reduced by more than fifty percent. This is excellent performance considering that the first fifteen modes of the plate were excited by the disturbance and that the control law used was not dependent upon knowledge of these modal frequencies. The reduction in settling time is comparable with that of the simulated simply-supported plate shown in Fig. 4.3 (uncontrolled) and Fig. 4.4 (controlled).

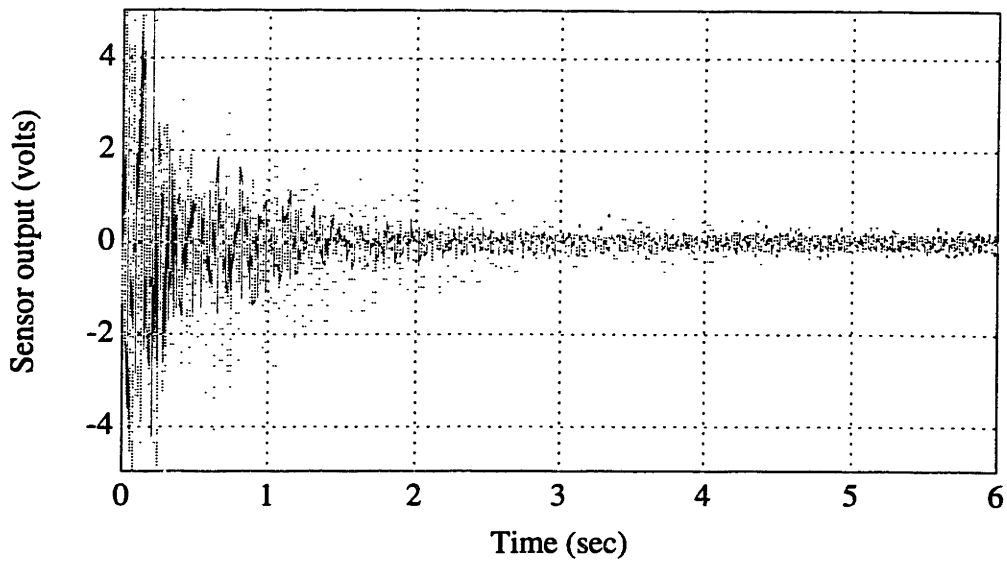

Fig. 5.15 Closed-loop time response (-) plotted with open-loop time response (...).

All of the modes within the disturbance bandwidth were actively damped. However, at the end of all of the closed-loop tests, there was a residual vibration signal, apparent even after 2.5 seconds. This signal is shown in a close-up view in Fig. 5.16. It is dominated by one signal at 25 Hz. This is not a mode of the plate, but it is close to a mode at 22 Hz. It was suspected that this was an external acoustic noise source that the controller could not control. As was noted in the previous section, the open-loop actuator/sensor transfer function shown in Fig. 5.13 shows poor coherence at this frequency.

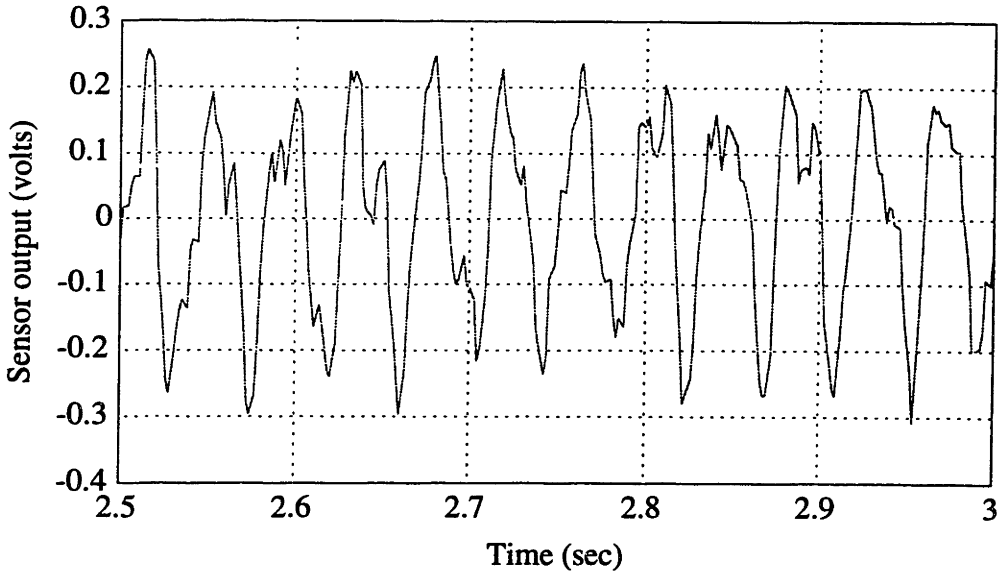

Fig. 5.16 Close-up view of controller residual response after 2.5 sec.

A closed-loop frequency response function between a stochastic disturbance input and the sensor output was measured using the shaker as the disturbance. The shaker was configured as for the open-loop test in section 5.5. The shaker was driven with low-passed random noise with a cutoff frequency of 125 Hz. The result is shown along with the same test done open-loop in Fig. 5.17. This result shows a damping improvement in some modes, but shows an increased response for the first mode.

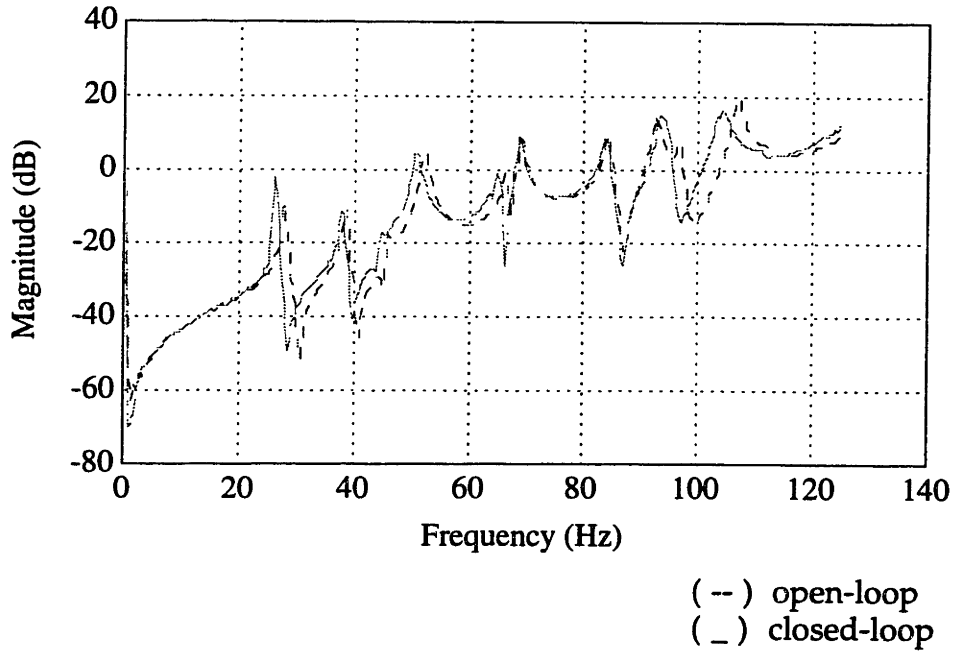

Fig. 5.17 Closed-loop and open-loop response for plate with stochastic disturbance.

It was suspected that this problem was due to an acoustic noise source at this frequency. This would have caused the odd structure in the 25 Hz and the 40-50 Hz regions on the open-loop test. To determine the cause, a microphone was placed near the plate and the power spectral density (PSD) of the sound field was measured. This test was conducted with the plate control deactivated. The sound field's PSD is shown in Fig. 5.18. As can be seen from the plot, the highest point occurs at 25 Hz in a very narrow spike. This is no doubt driven by fans in the air handling system. The balance of the sound PSD is more broad-band, reflecting sound radiation from the air circulation in the lab and other ambient sound.

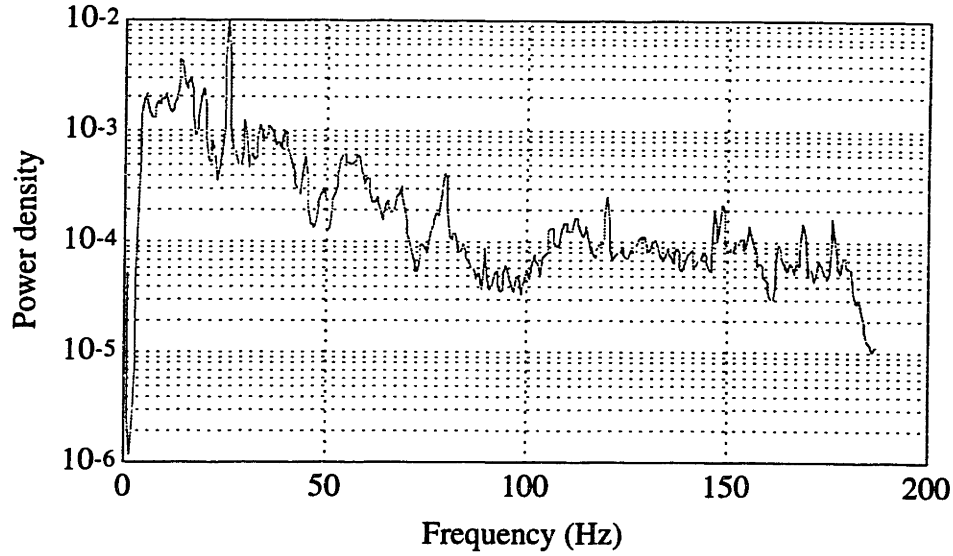

Fig. 5.18 Power spectral density measurement made of microphone placed near plate.

The effect of this acoustic noise on the plate/transducer structure was then determined from measuring the PSD of the sensor output when no disturbance, except for laboratory acoustic noise, was input to the plate. This PSD is shown in Fig. 5.19. Again, the controller was turned off for this test. As can be seen from the plot, the modes of the plate are seen along with the 25 Hz signal. This signal is very close to the first mode at 22 Hz.

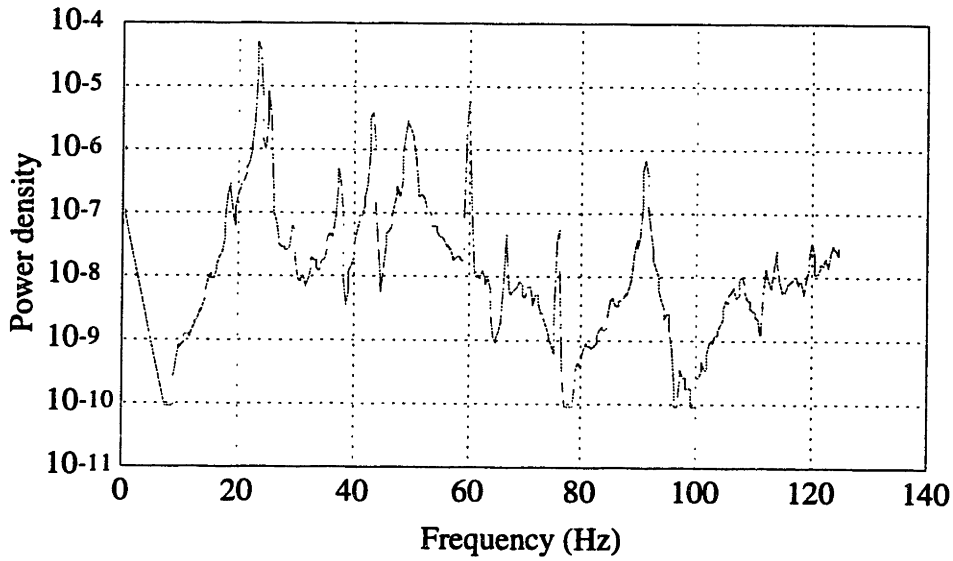

Fig. 5.19 Power spectral density measurement made of baseline sensor signal.

The controller was assumed to have control over those acoustic disturbances which excite modes in the plate. However, if an acoustic disturbance also affected the PVDF sensor through its thickness, by compression, then the controller would not have control over this disturbance. PVDF can sense acoustic sources through its thickness because it has a d_{33} or "hydrostatic" response in addition to a d_{31} and d_{32} in-plane strain response. This is because the PVDF actuators are applied to the plate as induced-strain devices. They can only affect bending in the plate. To see if an acoustic noise source was causing a signal on the PVDF sensor through compression of the PVDF, the plate was blocked with stiff foam over the entire actuator side to prevent bending vibrations. In this way, the only signal on the PVDF sensor would come from a hydrostatic response.

The resulting PSD of the sensor array signal with the plate blocked is shown in Fig. 5.20. The modal structure (e.g. resonant bending) of the plate has now disappeared. As can be seen from the plot, there is a significant peak at 25 Hz. This would explain why the controller cannot control this disturbance, because it affects the PVDF through its hydrostatic response. The controller sees a sensor array output signal at 25 Hz and thinks that bending is occuring in the plate at this frequency. It tries to counteract this bending and therefore actually causes 25 Hz bending in the plate. This does not destabilize the plate because the actuator array does not itself create a 3-3 sensor output. The actuator array cannot cause force in the 3-3 direction.

In addition to the peak at 25 Hz, the PSD has high amplitude in the 40-50 Hz region. This explains the poor coherence in the same region shown in the open-loop plot in Fig. 5.13. There is also a spike at 67 Hz but, as can be seen in Fig. 5.13, this frequency is not near a mode of the plate. Finally, there are the expected spikes at 60 and 120 Hz due to the line voltage.

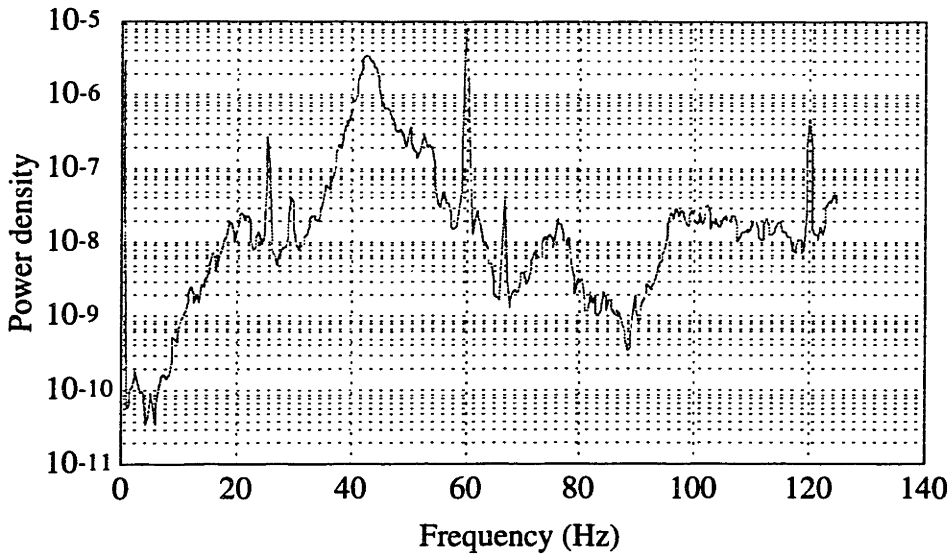

Fig. 5.20 Power spectral density measurement made of baseline sensor signal with the plate backed (bending motion prevented).

This effect does not diminish the results of the active control experiment, but it does highlight a concern when using PVDF as a sensor for structural acoustic control applications. The PVDF is not as sensitive in its thickness mode as in its bending mode, but the effect showed itself in this experiment because the PVDF sensor had a large surface area covering half of the plate (244 in^2). The compression response is integrated over the entire surface of the sensor. Therefore, a larger sensor area will result in this effect becoming more significant.

5.7 Summary and Recommendations

The experiment described in this chapter demonstrated that it is possible to design, fabricate and apply two-dimensional transducer distributions which will evenly couple into large groups of modes in plates. In addition, it was shown that colocation was achieved for gain-weighted actuator and sensor arrays. This facilitates the use of velocity feedback for global vibration suppression. Knowledge of the spatial response of the structure is used, especially modal symmetry, but no detailed knowedge is needed of the

temporal dynamics of the plate structure. Phase lags in the control system, however, must be understood in order to choose a maximum feedback gain.

In addition, an unexpected effect of using PVDF sensors in an acoustically noisy environment was discovered. This could provide a practical limitation for applying PVDF as a large-area sensor for structural acoustic control. This can occur with any other distributed transducer which can sense in the compression mode. Ways of alleviating or eliminating this effect should be studied in the future.

5.8 References

1. W.H. Hoppmann, Jr. and J. Greenspon, "An Experimental Device for Obtaining Elastic Rotational Constraint on Boundary of a Plate," Proceedings of the 2nd. National Congress on Applied Mechanics, pp. 187-191, 1954.

2. S.E. Burke, "Shape and Vibration Control of Distributed Parameter Systems - Extension of Multivariable Concepts Using Spatial Transforms," Mechanical Engineering PhD. Thesis, Department of Mechanical Engineering, Massachusetts Institute of Technology, May 1989.

Chapter 6:

Conclusions and Recommendations

6.1 Conclusions

This work focused on the modeling and design of two-dimensional distributed transducers for the active control of vibrations in plates. Chapter 1 reviewed the previous research conducted in the field of active control of plates and showed the necessity of research into the spatial part of the control design problem for plates.

A new modeling technique for two-dimensional distributed transducers was presented in Chapter 2. This approach allows distributed transducer shape to be incorporated into the control design process for multi-dimensional structures as an additional design parameter. The method is applicable to many types of strain-inducing transducers, such as piezoelectric, electrostrictive, and magnetostrictive materials. The derivation was based upon the theory of multivariable distributions and was extended to distributions with composite functions as arguments. In this manner, arbitrary spatial weightings of transducers could be described. A differentiation theorem for such distributions was developed and used to calculate the spatial differential operator for a strain-inducing transducer. Several applications were presented to show the utility of this technique and compare the results to previous research in the field.

This modeling method was used to verify shaping techniques developed previously to approximate one-dimensional transducer shading. It was also shown that two-dimensional delta and doublet function distributions could be obtained even when using a uniaxial transducer if the boundaries of the transducer (or electrode) were shaped to be nonorthogonal to the material axes. The approach is in exact agreement with previous work by Lee and Moon where they demonstrated that when the material axes of a transducer are skewed with respect to the rectangular boundary axes of an PVDF

electrode distribution, both delta and doublet function distributions along the boundary are obtained. Guidelines for defining spatial transducer distributions using generalized functions with composite arguments were also established.

In Chapter 3, the motivation for two-dimensional transducer shading was presented and various methods for achieving shading were considered for the active control of thin plates. Two-dimensional transducer shaping was shown to be a useful design tool for the control problem. It was also shown that transducer shaping can be combined with gain-weighting to provide close approximation of continuously shaded transducer distributions. The analysis was applied to two specific examples. One utilizes two-dimensional transducer shaping alone to establish controllability and observability over all but the even-even modes in a simply-supported plate. This transducer distribution is a very practical solution for the acoustic radiation attenuation problem. The second distribution is a superposition of gain-weighted, shaped transducer sections providing a good approximation to a continuous two-dimensional shaded transducer distribution. This distribution provides "all-mode" controllability and observability over a large bandwidth and is therefore useful for global vibration suppression in plates. An optimization method used to fit the approximation to the continuous transducer distribution over a specified number of modal coefficients was described.

Chapter 4 described the plate and transducer setup and dynamics. A rectangular, three-layer laminate which was simply-supported at the edges was used as a sample problem. Marginal stability was proven for any dissipative controller. Asymptotic stability was proven for the case of velocity feedback. The state matrices were then presented for the distributed parameter system so that the system was able to be simulated using MATLAB.

The experiment described in Chapter 5 demonstrated that it is possible to design two-dimensional colocated transducer arrays which will evenly couple into large groups of modes in plates. This facilitates the use of velocity feedback for global vibration suppression. Knowledge of the spatial response of the structure is used, especially modal symmety, but no knowedge is needed of the temporal dynamics of the structure. In addition, an unexpected effect of using PVDF sensors in an acoustically noisy environment was

discovered. This could pose problems when trying to use PVDF as a large-area sensor for structural acoustic control. This could occur with any other distributed transducer which can sense in the hydrostatic mode. Ways of alleviating or eliminating this effect should be studied in the future.

This thesis focused upon the modeling and design of two-dimensional transducers for the active control of multidimensional elastic structures. It was shown that two-dimensional distributed transducers can produce effects that are simply not possible using discrete transducers. Two-dimensional transducers can actuate or sense doublet functions distributed along transducer boundaries which vary across the surface of the structure. This effect allows one to achieve modal coupling that was impossible to achieve using any combination or number of discrete transducers.

6.2 Future Directions

The modeling work for distributed transducers should be extended to curved shapes. A circular transducer which is perfectly biaxial should exhibit uniform moments along the boundaries. This could be used as a test case for the modeling method. The result for an elliptical transducer could be derived and checked in the limit as the ellipse approaches a circle. In addition, the modeling work should be extended to cover two-dimensional distributed transducers applied to shells. Design guidelines for the control of shells could then be derived based upon this result.

The design work in Chapter 3 covered specific transducer distributions and shading. The work in this chapter should be extended to allow the design of a transducer distribution to directly meet desired performance goals specified through a modal coefficient profile.

In addition, the analytical transducer design work should be merged with multidimensional structures which are described by finite element models. In this way, the coupling of two-dimensional transducer distributions into these structures could be evaluated and experimentally checked.

Finally, a way of eliminating the hydrostatic sensitivity of PVDF, described by the d_{33} constant, should be determined if it is desired to use PVDF as a large-area structural sensor in an acoustically noisy environment.

Appendix:

Theory of Distributions Review

This appendix reviews the theory of distributions. The material in this appendix was gathered from Zemanian[1] and Lighthill.[2] In section A.1 and the first part of A.2, the definition of a distribution and various properties of distributions are summarized from the development presented by Zemanian.[2] Next, in section A.3, derivatives of distributions are defined and explained, again in a manner similar to Zemanian.

A.1 Definition of a Distribution (Generalized Function)

A functional assigns a number to every function which belongs to a specific set of functions, called test functions:

$$\langle f, \phi \rangle = \langle f(t), \phi(t) \rangle \equiv \int_{-\infty}^{\infty} f(t)\, \phi(t)\, dt, \tag{A.1}$$

where f is the functional and f is a test function. The definition of a suitable test function will follow. The $\langle\ \rangle$ notation used is the same as the inner product notation. Functionals are always defined as inner products with test functions. A distribution (or generalized function) is a functional which is also *linear* and *continuous*. Linearity of a distribution is defined by

$$\langle f, \phi_1 + \phi_2 \rangle = \langle f, \phi_1 \rangle + \langle f, \phi_2 \rangle, \tag{A.2}$$

$$\langle f, \alpha \phi \rangle = \alpha \langle f, \phi \rangle, \tag{A.3}$$

where α is a complex number (allowed to be real).

Continuity of a distribution is defined in the following manner. If a sequence of a functions converges to the test function $\phi(t)$,

$$\left\{\phi_\nu(t)\right\}_{\nu=1}^{\infty} \to \phi(t), \tag{A.4}$$

then, the sequence of a distribution acting on the function sequence converges to the value of the distribution acting on the test function $\phi(t)$,

$$\left\{\langle f, \phi_\nu \rangle\right\}_{\nu=1}^{\infty} \to \langle f, \phi \rangle. \tag{A.5}$$

The test function $\phi(t)$ upon which the distribution acts has the following properties:

a. Operates on the independent, real variable, t;

b. Complex-valued (can take either real or complex values);

c. Infinitely smooth on some finite interval (the function has continuous derivatives of all orders - these derivatives can be zero though);

d. Zero outside of a finite interval (bounded support).

An example of a test function is the following:

$$\zeta(t) = \begin{cases} 0 & |t| \geq 1 \\ x & |t| < 1 \end{cases}. \tag{A.6}$$

This function satisfies the criteria for a test function because it is infinitely smooth over the open interval (-1,1) and zero outside of this interval. This testing function does have discontinuities at 1 and -1. However, since test functions are only used in conjunction with distributions under integration, these discontinuities simply become bounds on the integral.

Also note that the bounded support requirement on the testing function can be relaxed if the distribution itself has bounded support. For example, the delta function, $\delta(t)$, has bounded support in that it only has a nonzero value at $t = 0$.

Two distributions, f and g, are defined as *equal* if they yield the same result when applied to a test function, i.e.

$$\langle f, \phi \rangle = \langle g, \phi \rangle \tag{A.7}$$

for all testing functions ϕ.

A.2 Operations on Distributions

Addition The sum of two distributions, f and g, is also a distribution and is defined as

$$\langle f+g, \phi \rangle \equiv \langle f, \phi \rangle + \langle g, \phi \rangle. \tag{A.8}$$

Multiplication of a distribution by a constant If α is any complex number (allowed to be real), then the product of α with a distribution, f, is defined as

$$\langle \alpha f, \phi \rangle \equiv \langle f, \alpha\phi \rangle = \alpha \langle f, \phi \rangle. \tag{A.9}$$

The last step in equation (A.9) follows directly from the linearity property of distributions.

Translation of a distribution If t is a real number, then a distribution translated by t acting on a test function is equivalent to the distribution without translation acting on a test function translated by $-\tau$.

$$\langle f(t-\tau), \phi(t) \rangle \equiv \langle f(t), \phi(t+\tau) \rangle. \tag{A.10}$$

This definition was established using a linear change of variable under integration

Example: Sifting property of delta functions

The "delta function", $\delta(t)$, is a well-known distribution with the following definition:

$$\langle \delta(t), \phi(t) \rangle = \phi(0). \tag{A.11}$$

Note that the delta function, $\delta(t)$, "sifts out"[1] the value of the test function at $t = 0$. The scalar value assigned to $\langle \delta(t-\tau), \phi(t) \rangle$ is defined using the translation property of a distribution:

$$\langle \delta(t-\tau), \phi(t) \rangle = \langle \delta(t), \phi(t+\tau) \rangle = \phi(\tau).. \tag{A.12}$$

The delta function, $\delta(t-\tau)$, "sifts out"[1] the value of the test function at $t = \tau$.

A.3 Distributional Derivatives

Ordinary differentiation does not make much sense on distributions. Take, for example, the case of the Heaviside function shown in Figure A.1:

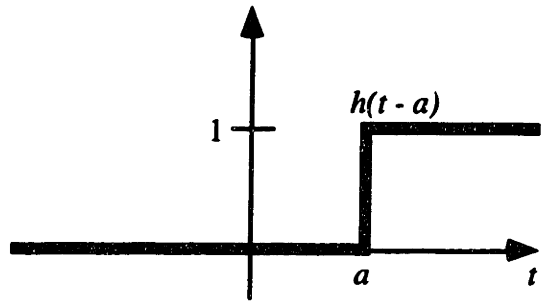

Figure A.1: Heaviside Function

The ordinary derivative of this distribution would be zero for $t < a$ and $t > a$ but would be infinite at $t = a$.

Distributional derivatives will be defined in this section. All distributions have derivatives of all orders and each distributional derivative is a distribution itself. The first distributional derivative is defined as

$$\langle f'(t), \phi(t) \rangle = \langle f(t), -\phi'(t) \rangle. \tag{A.13}$$

To understand this definition, use integration by parts:

$$\begin{aligned} \langle f'(t), \phi(t) \rangle &= \int_{-\infty}^{\infty} f'(t)\, \phi(t)\, dt \\ &= \int_{-\infty}^{\infty} u\, dv \\ &= u\, v]_{-\infty}^{\infty} - \int_{-\infty}^{\infty} v\, du \end{aligned} \tag{A.14}$$

where

$$\begin{aligned} u &= \phi(t) \\ du &= \phi'(t)\, dt \\ dv &= f'(t)\, dt \\ v &= f(t) \quad . \end{aligned} \tag{A.15}$$

Substituting in:

$$u\,v]_{-\infty}^{\infty} - \int_{-\infty}^{\infty} v\,du = f(t)\,\phi(t)]_{-\infty}^{\infty} - \int_{-\infty}^{\infty} f(t)\,\phi'(t)\,dt. \tag{A.16}$$

The first term in the right-hand side of the equation is zero if either $\phi(t)$ or $f(t)$ has bounded support, i.e. either $\phi(t)$ or $f(t)$ is zero at $t = \pm\infty$. Therefore,

$$\langle f'(t), \phi(t) \rangle = \langle f(t), -\phi'(t) \rangle. \tag{A.17}$$

Using relation (A.17) helps when trying to determine distributional derivatives. For example, one might ask what the distributional derivative of the Heaviside function is:

$$\begin{aligned} \langle h'(t), \phi(t) \rangle &= \langle h(t), -\phi'(t) \rangle \\ &= -\int_0^{\infty} \phi'(t)dt \ . \end{aligned} \tag{A.18}$$

Now integrate to obtain

$$\begin{aligned} -\int_0^{\infty} \phi'(t)dt &= -\{\phi(t)]_{\infty} - \phi(t)]_0\} \\ &= \phi(0) \\ &= \int_{-\infty}^{\infty} \delta(t)\phi(t)dt \quad . \end{aligned} \tag{A.19}$$

Therefore,

$$\langle h'(t), \phi(t) \rangle = \langle \delta(t), \phi(t) \rangle. \tag{A.20}$$

The derivative of the heaviside function is equivalent to the delta function in the distributional sense.

Substituting the delta function into equation (A.13) yields the following relation:

$$\langle \delta'(t), \phi(t) \rangle = \langle \delta(t), -\phi'(t) \rangle = -\phi'(0). \tag{A.21}$$

The derivative of the delta function is known as the doublet function. Instead of sifting out the value of the test function at $t = 0$, the doublet function sifts out the slope of the test function at $t = 0$.

A.4 References

1. A. Zemanian, **Distribution Theory and Transform Analysis: An Introduction to Generalized Functions, with Applications**, Dover Publications Inc., Mineola, NY (1987).

2. M. Lighthill, **An Introduction To Fourier Analysis and Generalized Functions**, Cambridge University Press, Cambridge, England (1958).